Calibration and validation of a damage model for 6005-T6 aluminium

Stanić, Matej

UNIVERSITY OF ZAGREB

FACULTY OF MECHANICAL ENGINEERING AND NAVAL ARCHITECTURE

MASTER'S THESIS

Matej Stanić

Zagreb, 2021

UNIVERSITY OF ZAGREB

FACULTY OF MECHANICAL ENGINEERING AND NAVAL ARCHITECTURE

MASTER'S THESIS

CALIBRATION AND VALIDATION OF A DAMAGE MODEL FOR 6005-T6 ALUMINIUM

Mentor:

Full Prof. Zdenko Tonković, PhD

Student:

Matej Stanić

Zagreb, 2021

IZJAVA

Pod punom moralnom odgovornošću izjavljujem da sam ovaj rad izradio samostalno, koristeći se znanjem stečenim tijekom studija te navedenom literaturom.

STATEMENT

I hereby declare that this thesis is entirely the result of my own work. The research has been conducted employing the knowledge obtained during my undergraduate and graduate studies, except where otherwise indicated. All used sources are given in the list of referenced literature.

ACKNOWLEDGMENT

First, I would like to express my gratitude to my mentor, Professor Zdenko Tonković, for his suggestions, time and support he provided during the writing of this thesis. Also, a very special thanks to him for all transferred knowledge and very friendly attitude to me during my studies.

Secondly, big thanks goes to Mr. Nikola Naranča for giving me the opportunity to write this paper in collaboration with companies AVL-AST d.o.o. and AVL List GmbH.

I have to express the greatest gratitude to Mr. Roman Baranja, who besides me, invested the largest amount of time and effort into this thesis. His guidance and daily advice allowed me a successful completion of this thesis. Thank you for your patience and good humor for which it was a pleasure to work with you.

My enormous thanks goes to my parents, Dubravka and Marinko. Thank you for always believing in me and for the opportunity to study. I would not be here without your support!

My very special thanks goes to my fiancée Doris, for her love, unconditional support, encouragement and patience. Thank you for always being by my side and for motivating me to work even harder.

Also, big thanks goes to my sister Andrea, to my brothers Ivan and Luka, to Maja and Romana for all the great moments we spent together in the dormitory. With you, studying was a lot more fun.

I would like to thank my best friend Marin, who helped me the most during my studies, along with my brothers. Furthermore, big thanks to all my friends from the choir of altar servers, for the great support and the opportunity for my personal development.

Thanks to my aunt Ana, for all the support and lunches she prepared in the last six years. Also, thanks to my uncle Ivica for big financial support.

Finally, enormous thanks to God Almighty for all the gifts and knowledge given to me, and for all the people I met during my studies.

Matej Stanić

SVEUČILIŠTE U ZAGREBU
FAKULTET STROJARSTVA I BRODOGRADNJE
Središnje povjerenstvo za završne i diplomske ispite
Povjerenstvo za diplomske ispite studija strojarstva za smjerove:
procesno-energetski, konstrukcijski, brodostrojarski i inženjersko modeliranje i računalne simulacije

Sveučilište u Zagrebu Fakultet strojarstva i brodogradnje	
Datum:	Prilog:
Klasa: **602 - 04 / 21 - 6 / 1**	
Ur. broj: **15 - 1703 - 20 -**	

DIPLOMSKI ZADATAK

Student: **Matej Stanić** Mat. br.: 0035204179

Naslov rada na hrvatskom jeziku: **Kalibracija i validacija modela oštećenja za 6005-T6 aluminij**

Naslov rada na engleskom jeziku: **Calibration and validation of a damage model for 6005-T6 aluminium**

Opis zadatka:

Simulation tasks and techniques today have the goal and challenge of accurate prediction of complex physical and mechanical behaviour of systems or single components. Therefore, a valid prediction of material properties of analysed components plays a vital role in the numerical modelling and computer simulation process.

Accordingly, the task and purpose of this Master Thesis is the finite element calibration of the material model for extruded 6005-T6 aluminium, with the emphasis on the damage behaviour of the material, subjected to the quasi-static loading. The calibration is based on experimental measurement results for various types of specimens, covering tensional (uniaxial and biaxial) and shear stress states of the material. The test specimens are cut only in the extrusion direction of the analysed aluminium profile.

Based on everything said above in this study it is necessary to:

1. Study available literature on the damage modelling of ductile metals.
2. Calibrate hardening curve parameters of the material for 2mm and 3mm thick specimens.
3. Calibrate damage model parameters for 2mm and 3mm thick specimens.
4. Validate finite element simulations against experimental measurements.

During thesis preparation one must comply with the standard rules for preparation of master thesis. It is necessary to list all literature used and received assistance.

Zadatak zadan: 12. studenoga 2020.

Datum predaje rada: 14. siječnja 2021.

Predviđeni datum obrane: 18. – 22. siječnja 2021.

Zadatak zadao:

Prof. dr. sc. Zdenko Tonković

Predsjednica Povjerenstva:

Prof. dr. sc. Tanja Jurčević Lulić

Contents

List of Figures

List of Tables

List of Symbols and Units

Latin symbols

Symbol	Unit	Description
A	N/mm^2	Strength coefficient
c_d	m/s	Dilatation wave speed
D	-	Overall damage variable
E	N/mm^2	Young's modulus
E	J	Energy
f	-	Yield function
f	Hz	Frequency
h	mm	Shear notch width
$\mathbf{I}$	N	Vector of internal forces
I_1	N/mm^2	First invariant of stress tensor
J_2	N/mm^2	Second invariant of deviatoric stress tensor
k	-	Shear geometry parameter
k_0	N/mm^2	Initial yield strength
L	mm	Characteristic element length
L_{min}	mm	The smallest element length
$\mathbf{M}$	kg	Nodal mass matrix
n	-	Strain hardening exponent
p	N/mm^2	Hidrostatic pressure
$\mathbf{P}$	N	Vector of external forces
q	N/mm^2	Von Mises equivalent stress
Q	N/mm^2	Stress difference between saturated and yield stress
$\mathbf{s}$	N/mm^2	Deviatoric stress tensor
$\mathbf{u}$	mm	Displacement vector
$\dot{\mathbf{u}}$	mm/s	Vector of nodal velocities
$\ddot{\mathbf{u}}$	mm/s^2	Vector of nodal accelerations
$\dot{\overline{u}}^{pl}$	mm	Equivalent plastic displacement
t	s	Time

Greek symbols

Symbol	Unit	Description
α	-	Weighting factor
β	-	Strain coefficient
Δx	mm	Shear notch offset
$\dot{\overline{\varepsilon}}^{pl}_{\mathrm{D}}$	-	Equivalent plastic strain rate
$\overline{\varepsilon}^{pl}_{\mathrm{D}}$	-	Equivalent plastic strain at the onset of damage
ε_{eng}	-	Engineering strain
ε^{p}_{eq}	-	Equivalent plastic strain
$\varepsilon^{p}_{eq,f}$	-	Equivalent plastic strain to failure
ε^{p}_{ij}	-	Plastic strain tensor
ε_{true}	-	True strain
η	-	Stress triaxiality
ρ	$\mathrm{kg/m^3}$	Density
σ_{eng}	$\mathrm{N/mm^2}$	Engineering stress
σ_{ij}	$\mathrm{N/mm^2}$	Stress tensor
σ_{true}	$\mathrm{N/mm^2}$	True stress
σ_{Y}	$\mathrm{N/mm^2}$	Yield strength
ω_d	-	Damage variable

List of Abbreviations

Abreviations	Description
BEV	Battery electric vehicle
CDM	Continuum damage mechanics method
CH	Center hole specimen
DIC	Digital image correlation
DOF	Degree of freedom
HEV	Hybrid electric vehicle
ICE	Internal combustion engine
NT6	Tensile specimen with 6.67 mm notch radius
NT20	Tensile specimen with 20 mm notch radius
PHEV	Plug-in hybrid electric vehicle
SH-HD	Shear high ductility specimen
SH-LD	Shear low ductility specimen
SH-MD	Shear moderate ductility specimen
UT	Uniaxial tension specimen
UTS	Ultimate tensile strength

Sažetak (Abstract in Croatian)

Automobilska industrija jedna je od najvećih svjetskih industrija te je predvodnik u inovativnim inženjerskim rješenjima. Ipak, uslijed potrebe za smanjenjem emisije štetnih ispušnih plinova, klasična automobilska industrija doživljava veliku transformaciju. Upotreba konvencionalnih motora s unutarnjim izgaranjem sve se više zamjenjuje električnim pogonom. Elektromotori dobivaju električnu energiju iz baterijskih blokova koji su smješteni u podvozju vozila. Budući da većina baterija sadrži zapaljive kemikalije, u slučaju sudara one predstavljaju veliku opasnost za korisnike. Stoga, baterijski se blokovi postavljaju u kučišta izrađena od aluminijskih legura koje ih štite u slučaju udara. Osim relativno niske gustoće, aluminijske legure imaju dovoljnu duktilnost koja osigurava apsorpciju energije prilikom udara. Za optimalno konstruiranje kučišta baterija, potrebno je poznavati točna svojstva korištene legure te njezino ponašanje prilikom razvoja duktilnog oštećenja uslijed opterećivanja.

U ovome radu analizirana je 6005-T6 aluminijska legura koja se često koristi u automobilskoj industriji. Na početku je prikazana teorijska pozadina elastoplastičnog ponašanja materijala i ponašanja materijala uslijed rasta duktilnog oštećenja. Kako bi se materijal točno implementirao u numeričke simulacije, provedena su eksperimentalna ispitivanja na različitim vrstama uzoraka kako bi se opisalo što više stanja naprezanja. Za opis elastoplastičnog ponašanja materijala korišten je kombinirani Swift-Voce zakon tečenja, čiji su parametri određeni inverznom eksperimentalno-numeričkom procedurom. Provedena je analiza iniciranja i razvoja duktilnog oštećenja primjenom programskog paketa *Abaqus*, koja je validirana s rezultatima eksperimentalnih mjerenja. Određeni su parametri nastanka i propagacije oštećenja za različita stanja naprezanja.

Ključne riječi: elastoplastično ponašanje, kombinirani Swift-Voce zakon tečenja, triaksijalnost, duktilno oštećenje, metoda konačnih elemenata

Abstract

The automotive industry is one of the world's largest industries. Also it is a leader in innovative engineering solutions. However, due to the need to reduce pollutant exhaust emissions, the classic automotive industry is undergoing a major transformation. The use of conventional internal combustion engines is increasingly being replaced by electric powertrain. Electric motors use power from energy stored in battery packs located in the chassis of the vehicle. Since the most batteries contain flammable chemicals, they pose a great danger to users in the event of a collision. Therefore, the battery packs are placed in housings made of aluminium alloys that protect them in the event of an impact. In addition to relatively low density, aluminium alloys have sufficient ductility to ensure energy absorption on impact. For optimal construction of the battery housing, it is necessary to know the exact properties of the alloy used and its behavior during the development of ductile damage due to loading.

In this paper, a 6005-T6 aluminium alloy that is often used in the automotive industry is analyzed. At the beginning, the theoretical background of elastoplastic material behavior and material behavior due to the evolution of ductile damage is presented. In order to accurately implement the material into numerical simulations, experimental tests were performed on different specimen types to describe as many stress states as possible. To describe the elastoplastic behavior of the material, a combined Swift-Voce flow law was used, the parameters of which were determined by an inverse experimental-numerical procedure. An analysis of the initiation and evolution of ductile damage was performed using the *Abaqus* software package. Afterwards, the analysis results were validated with the results of experimental measurements. The parameters of damage initiation and propagation for different stress states are determined.

Keywords: elastoplastic behavior, combined Swift-Voce flow law, ductile damage, triaxiality, finite element method

Prošireni sažetak

Ovaj rad izrađen je u suradnji s hrvatskom tvrtkom AVL-AST d.o.o. te austrijskom tvrtkom AVL List GmbH. Navedene tvrtke bave se razvojem pogona vozila pokretanih motorima s unutarnjim izgaranjem i električnih pogonskih sklopova. Osim toga, razvijaju različitu mjernu opremu za automobilsku industriju.

Električni pogon vozila sastoji se od baterijskih sklopova u kojima je pohranjena električna energija i elektromotora. Baterijski blokovi smješteni su u kučištima i nalaze se u podvozju vozila. Lako zapaljive kemikalije, koje se nalaze u baterijama, predstavljaju veliku opasnost ukoliko prilikom sudara dođe do njihovog istjecanja iz baterija. Zato kučišta moraju biti konstruirana tako da spriječe oštećenje samih baterija. Za njihovu izradu često se koriste aluminijske legure. Aluminijske legure odlikuje niska gustoća, pa komponente izrađene od njih ne pridonose znatnom povećanju mase vozila. Osim toga, relativno visoka čvrstoća i duktilnost omogućuju dovoljnu deformabilnost i apsorpciju energije. Tijekom procesa konstruiranja baterijskog sklopa provode se brojni eksperimenti kako bi se povjerio dolazi li do gubitka mehaničkog integriteta baterijskog sklopa. Ipak, provedba velikog broja eksperimenata može dovesti do velikog povećanja cijene uz veliko vremensko produljenje procesa konstruiranja i izrade. Zato se u zadnje vrijeme sve više pribjegava korištenju numeričkih simulacija u procesu konstruiranja baterijskih sklopova. Na taj način pojednostavljuje se i skraćuje proces izrade konačne komponente. Za točnu dinamičku ili kvazistatičku numeričku analizu sudara baterijskog sklopa, potrebno je poznavati točna svojstva korištenih materijala, te implementirati materijal u program za numeričke simulacije. Za određivanje svojstava materijala tijekom procesa deformiranja i razvoja duktilnog oštećenja, potrebno je provesti eksperimentalna mjerenja na uzorcima. Na osnovu eksperimentalnih rezultata, provodi se kalibracija numeričkog modela elastoplastičnog ponašanja materijala kao i kalibracija inicijacije i razvoja duktilnog oštećenja. Područje istraživanja ovoga rada može se podijeliti u tri cjeline:

1. Provođenje eksperimentalnih ispitivanja na uzorcima izrađenim od aluminijeve legure 6005-T6 koja se koristi u izradi baterijskih kučišta,

2. Korištenjem numeričkih simulacija opisati elastoplastično ponašanje materijala pomoću kombiniranog Swift-Voce zakona tečenja,

3. Kalibrirati parametre modela duktilnog oštećenja ugrađenog u programski paket *Abaqus*, te validirati rezultate numeričkih simulacija s eksperimentalnim mjerenjima.

U prvom poglavlju rada prikazan je kratak opis automobila na električni pogon, kao i baterijskih sklopova koji se u njima koriste.

U drugom poglavlju opisana su svojstva 6005-T6 aluminijske legure. Nadalje, prikazane su teorijske osnove numeričkog opisivanja elastoplastičnog ponašanja materijala pomoću Swift-Voce zakona tečenja. Prikazan je i algoritam implementacije korištenog zakona tečenja u programski paket *Abaqus*. Također, detaljno je opisan proces nastajanja i razvoja duktilnog oštećenja, te su navedeni razni modeli njegovog numeričkog opisa. Budući da je u ovom radu korišten programski paket *Abaqus*, prikazan je ugrađeni model duktilnog oštećenja.

U trećem je poglavlju opisan eksperimentalni postav korišten za određivanje svojstava materijala. Prikazani su tipovi uzoraka i rezultati eksperimentalnih mjerenja. Osim toga, prikazane su i postavke numeričkih simulacija kao i korišteni numerički modeli. Na osnovu eksperimentalnih mjerenja provedena je kalibracija numeričkog modela elastoplastičnog ponašanja materijala i na kraju je prikazana usporedba reultata provedenih analiza s eksperimentalnim mjerenjima.

Četvrto se poglavlje bavi inicijacijom i razvojem duktilnog oštećenja. Opisan je način kalibracije parametara duktilnog oštećenja pomoću eksperimenata i numeričkih simulacija. Prikazani su rezultati numeričkih simulacija u usporedbi s eksperimentalnim odzivom materijala.

Na kraju, u završnom su poglavlju istaknuti svi zaključci istraživanja te su navedene preporuke za daljnji rad.

1 Introduction

Due to increasing limitation of pollution, performance, energy consumption reduction, safety and phase-out of fossil fuel cars, the goal of the modern automotive industry is to produced lightweight and reliable vehicles powered by electricity. Currently, the most of the electric vehicles are run by combination of internal combustion engine (ICE) and electric motor with battery, like hybrid vehicles. The main advantage of these vehicles is that the different motors work better at different speeds, the electric motor is more efficient at producing turning power and the combustion engine is better for maintaining high speed. Switching from one to the other at the right time provides higher energy efficiency and lower fuel consumption. There are two main types of hybrids: hybrid electric vehicles (HEVs) and plug-in hybrid electric vehicles (PHEVs). HEVs have smaller battery pack, therefore the most of the energy is still produced by ICE. Charge of the batteries from the regeneration of energy from braking in city driving is the biggest advantage of these type of hybrids. In PHEV models, the battery pack is significantly larger and produce much more energy for electric motor. Furthermore, PHEVs have the ability to charge the battery from electric source outside the vehicle (i.e. home and public charging points). Schematic models of HEVs and PHEVs are shown in Figure 1.1.

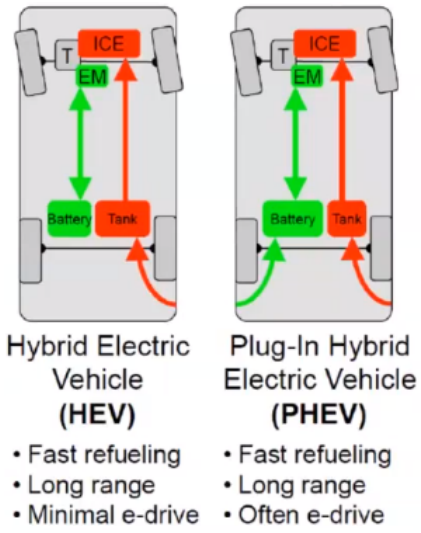

Figure 1.1: Schematic representation of HEVs and PHEVs [1]

On the other hand, battery electric vehicles (BEVs) have no combustion engine, but are made with a large battery pack and electric motor. The main advantage of these vehicles is that air pollution is from the upstream generation and emissions of the vehicles are reduced to zero. Moreover, BEVs also have possibility to charge batteries from regenerative braking. Model of BEV is shown in Figure 1.2.

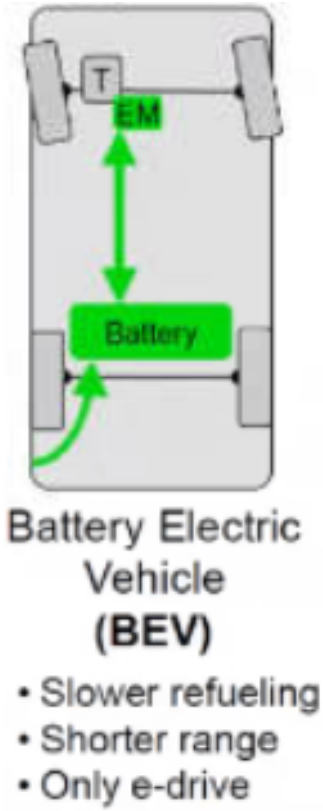

Figure 1.2: Schematic representation of BEVs [1]

Still, there are also a lot of problems in the BEVs practical usage. Limited range and lack of the re-fuelling infrastructure is preventing its wider application. Also, the costs of the powertrain production, which are a result of the incorporation of the big Lithium-ion battery packs, further increase the total price of the vehicles. Additionally, the charge duration can take up to 12 hours [2]. On top of that, the battery packs contain highly flammable liquids that are very dangerous in case of a short circuit or a crash, therefore, a special attention must be paid to the construction and integration of the battery packs into the powertrain. Lithium-based traction batteries are usually completely enclosed in the battery housing and integrated in the vehicle to protect the battery from all conceivable stresses and external influences. Numerous crash test and numerical simulation procedures are designed to prevent liquid leakage and sudden fires in case of accidents. Battery packs and housing are shown in Figure 1.3.

Figure 1.3: Battery powertrain [3]

1.1 Motivation

With the improvement of electric vehicles safety standards, there is a growing need for use of lightweight materials with satisfying strength and crashworthiness. Battery housing protects the most important and vulnerable part of the electric vehicle from mechanical shocks and fire. Aluminium is the most used material in the battery housing designs. Its strength and ductility allow it to absorb a large amount of damage before failure. During a battery pack design many experiments on real models are conducted to see whether they comply with security standards. Still, experiments are expensive and in recent times, numerical simulations are increasingly used to evaluate structural integrity. Therefore, valid prediction and modelling of the material properties of the analyzed components plays a vital role in the simulation process. It is necessary to calibrate and validate a material behaviour before and during the damage process in order to correctly predict the material response.

1.2 Thesis structure overview

The aim of this thesis is to correctly predict hardening and damage response of 6005-T6 aluminium under quasi-static loading. In the first chapter a brief description of battery usage in automotive industry is given, as well as importance of correct battery housing material calibration.

Chapter 2 discusses 6005-T6 aluminium properties and hardening model used for its

calibration. Also, the theoretical background of combined Swift-Voce flow law is studied in this chapter. It also covers basic principles and theory of the ductile damage, as well as its implementation in *Abaqus*.

Chapter 3 presents the experimental and numerical setup of the calibration. Swift-Voce parameters determination procedure is shown and results obtained by using Swift-Voce hardening model are discussed.

Furthermore, ductile damage calibration is presented in chapter 4. The results of the performed analysis and validation of ductile damage are shown.

The conclusions of this work and recommendations for future works are presented in the final chapter of this thesis.

2 Material model

2.1 6005-T6 aluminium alloy

Aluminium and its alloys are of the most versatile, economical and attractive metallic materials in the world, due to the unique combination of properties provided by the possibility of alloying with various metals. Aluminium alloys are second to steels in use as structural metals. With a destiny of only 2700 kg/m^3 and coupled with the high strength (some alloys even bigger than structural steel) and ductility, aluminium is ideal for design and construction of strong, lightweight structures, especially those that move like space vehicles and aircraft as well as land-borne vehicles. Also, aluminium is extremely resistant to the atmospheric corrosion, due to its tendency to form a compact oxide layer over the surface. It can also resist corrosion by water, salt and other environment if it is appropriately alloyed and treated. What is most important, aluminium can be fabricated in any desired form. It can be cast in any form, rolled to thickness down to foil thinner than paper, forged, hammered, it can be stamp, drawn, spun formed. Moreover, there is almost no limit to the different profiles (shapes) in which the metal can be extruded [5]. Additionally, various types of aluminium extruded profiles are shown in Figure 2.1.

Figure 2.1: Aluminium extruded profiles [4]

Aluminium alloys are usually divided into two categories: wrought and cast compositions. A further differentiation for each category is based on the primary mechanism of property development. A nomenclature for different types of wrought and cast alloys has been developed by the Aluminum Association and its designation system is widely accepted in the world. Their alloy identification system employs different nomenclatures for wrought and cast alloys, but divides alloys into families for simplification. For wrought alloys a four-digit system is used to produce a list of wrought composition families. For instance, the primary alloying element is labeled by the first number of alloy designation and this element produces a group of alloys with similar properties. The second number denotes whether it is a modification of an existing alloy and the last two digits are assigned sequentially by the association [6]. Examples of aluminium wrought alloy families are listed in Table 2.1.

Table 2.1: Wrought Alloy Designation System and Characteristics [6]

Series Number	Primary Alloying Element	Relative Corrosion Resistance	Relative Strength	Heat Treatment
1xxx	None	Excellent	Fair	Non-heat-treatable
2xxx	Copper	Fair	Excellent	Heat-treatable
3xxx	Manganese	Good	Fair	Non-heat-treatable
4xxx	Silicon	-	-	Non-heat-treatable
5xxx	Magnesium	Good	Good	Non-heat-treatable
6xxx	Magnesium and silicon	Good	Good	Heat-treatable
7xxx	Zinc	Fair	Excellent	Heat-treatable

In addition to the huge variety of alloys that are available, the temper of each alloy can create considerable differences in their characteristics and how they react to various fabrication processes (forming, welding etc.). As it can be seen in Table 2.1, there are heat treatable and non-heat treatable aluminium wrought alloys. Alloys in the non-heat-treatable group can not be strengthened significantly by heat treatment, and their properties depend upon the degree of cold work. On the other hand, heat treatable alloys have increased strength beyond the strengthening effect of adding alloying elements. Both heat treatable and non-heat treatable alloys can be strengthen by strain-hardening (*cold working*), which is achieved by mechanical deformation of the material at ambient temperature. As the material is strain-hardened, it becomes resistant to further deformation and its strength increases. This strain-hardened alloy can be heat treated to stabilize properties so that strength does

not decrease over time (*age softening*). First, the material can be solution heat treated. This allows soluble alloying elements to enter into solid solution; they are retained in a supersaturated state upon *quenching*, a controlled rapid cooling usually performed using air or water. Next, the material may undergo a *precipitation heat treatment*, also called *artificial aging*, by which constituents are precipitated from solid solution to increase the strength. An example of this process is the production of 6xxx series T6 tempers [6].

The primary alloying elements of 6xxx series are magnesium and silicon in proportions that form magnesium silicide (Mg_2Si). Despite the lower strength than 2xxx and 7xxx series alloys, 6xxx series alloys is widely used in architecture, marine and automotive industry, due to its excellent formability, weldability, machinablity and corrosion resistance. However, the most important advantage of these alloy series is extreme extrudability in combination with good strength, which allows its application to various industries. Alloy 6005-T6 is one of the most popular alloys in aircraft and automotive industry. It is used for the construction of the vehicles profile structures and the battery cases, as well as for fabrication of railways, platforms and pipelines. 6005-T6 wrought alloy contains up to 1.5% each of magnesium and silicon. The additions of magnesium increase the strength of aluminium without unduly decreasing ductility and the additions of silicon reduce cracking tendency of aluminium alloys [5]. Chemical composition limits for 6005 wrought alloy are displayed in Table 2.2.

Table 2.2: Chemical composition limits for 6005 wrought alloy in percentage [%] [6]

Alloy designation	Si	Fe	Cu	Mn	Mg	Cr	Zn	Ti	Al minimum
6005	0.6-0.9	0.35	0.1	0.1	0.4-0.6	0.1	0.1	0.1	Remainder

2.2 Swift-Voce hardening law

In order to correctly predict the behaviour and damage of components and structures made of the 6005-T6 aluminium, it is necessary to develop a material model which corresponds to the real material. Basic material properties, like Young's modulus, Poisson modulus and density, must be known for accurate crash simulation. Furthermore, strain hardening curve of the material is crucial for damage modelling as it contains information about the material response in the plastic area. Material properties such as Young's modulus, Poisson modulus, ultimate tensile strength, yield strength and stress-strain relationship are identified through the uniaxial tensile test. Material hardening is usually

described by the hardening (flow) laws which are analytical expressions used to fit plastic region of an experimental true stress-strain data. As it can be seen in Figure 2.2, there are many different hardening laws available in the literature. Most of them fit well with the real material flow curve up to the point of necking, but the extrapolation for large strains can differ depending on the model considered.

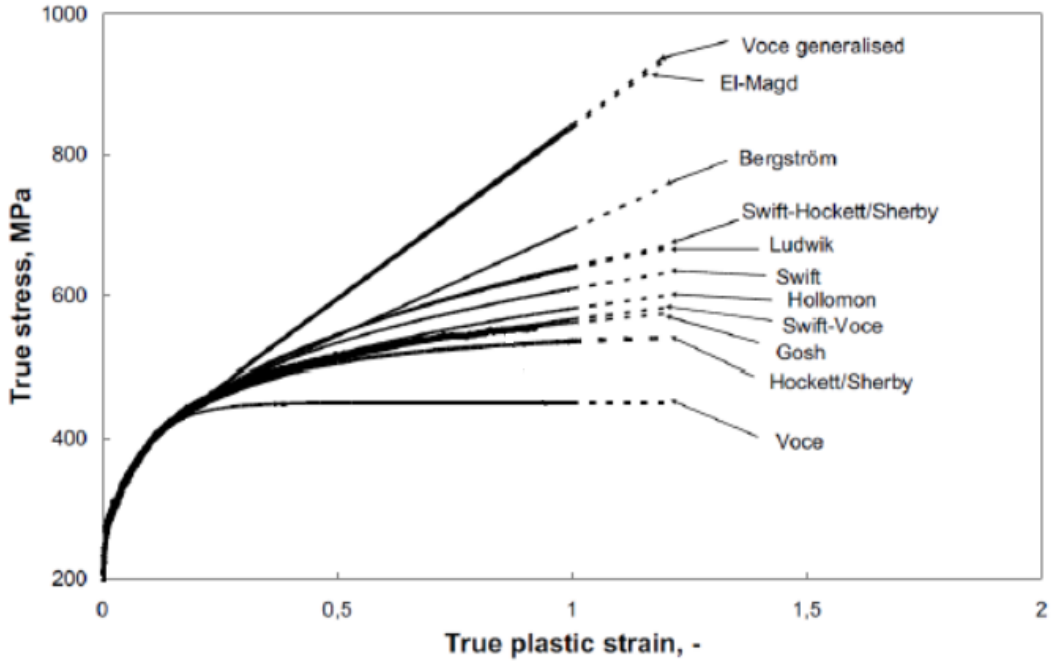

Figure 2.2: Stress-strain relationship for different hardening laws [7]

According to Papasidero *et al.*[8] combined Swift-Voce hardening law is the most suitable for numerical modelling of aluminium alloys. It is linear combination of Swift and Voce isotropic flow laws. Isotropic hardening is widely used in describing the work hardening because it is very easy to implement in numerical simulation code. During the isotropic hardening, yield surface expands equally in all directions of the stress space while its shape remains constant [9]. Evolution of the yield surface under loading is shown in Figure 2.3.

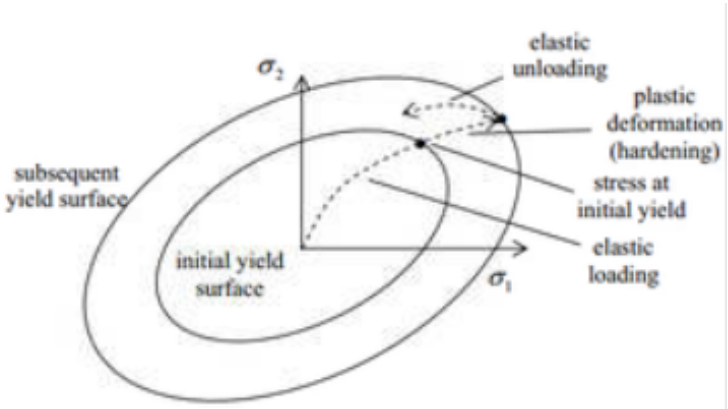

Figure 2.3: Yield surface expansion under isotropic hardening [9]

On the other hand, the isotropic hardening presumes that yield strength in compression and tension are initially the same and that they remain equal as the yield surface develops with the plastic strain. That implies that material loaded in tension past yield, when it is unloaded and subjected to compression, it will not yield in compression until it reaches the stress that was reached when loading it in tension. However, this problem is related to the cyclic loading [11].

The yield function is expressed as:

$$f(\sigma_{ij}, \varepsilon_{ij}^{p}) \leq 0, \tag{2.1}$$

Every stress state at some point within a material is determined by a single point in the principal stress space. If that point is inside the yield surface, $f < 0$, the the material is in an elastic stress state, without any plastic deformation. However, if $f = 0$ plastic strain occurs. The expression in which the yield surface is greater than zero, $f > 0$, has no physical meaning. Yielding in the isotropic materials depends only on the values of the principal stresses and not on their directions because all directions are equally valued. In this work, yielding and the yield surface were described by the Von Mises yield criterion:

$$f(\sigma_{ij}, \varepsilon_{ij}^{p}) = \frac{1}{\sqrt{2}}\sqrt{(\sigma_1 - \sigma_2)^2 + (\sigma_2 - \sigma_3)^2 + (\sigma_3 - \sigma_1)^2} - \sigma_{\mathrm{Y}}(\varepsilon_{ij}^{p}) = 0, \tag{2.2}$$

where σ_{Y} is the yield stress in uniaxial tension and σ_i are the principal stresses. The Von Mises yield criterion is illustrated in Figure 2.4 and it corresponds to a circular cylinder. The axis equally inclined to all three principal axes is called hydrostatic axis and the experiments show that the yielding is unaffected by uniform hydrostatic tension or compression. The plane perpendicular to the hydrostatic axis is called π-plane or a deviatoric plane. Yield surface and deviatoric plane intersect in a curve called yield curve or yield locus.

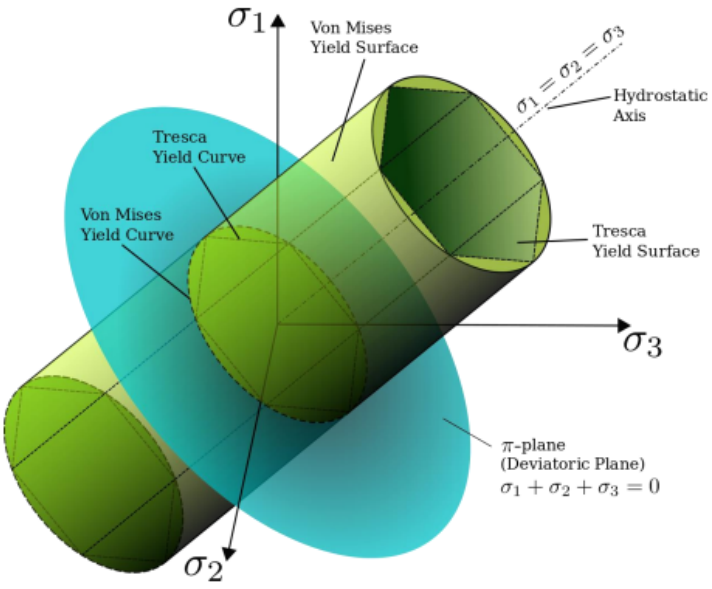

Figure 2.4: Visual representation of yielding criteria in the principal stress space [10]

The yield stress σ_Y is related to the effective plastic strain, and its functional dependence on the effective plastic strain is given by the universal flow curve of the material [11]. As said, Swift and Voce isotropic hardening laws are the most appropriate for determination of flow curves of the aluminium alloys, especially sheet metals. Swift law is a power law and it is defined as:

$$\sigma_s[\overline{\varepsilon}_p] = A(\overline{\varepsilon}_p + \varepsilon_0)^n, \tag{2.3}$$

with material coefficients ε_0 (elastic strain at the initial yield point), A, n known as strength coefficient (A) and strain hardening exponent (n). $\overline{\varepsilon}_p$ is true effective plastic strain which is calculated from plastic strain tensor. Furthermore, Voce hardening law is exponential law and it is described by the following equation:

$$\sigma_v[\overline{\varepsilon}_p] = k_0 + Q(1 - e^{-\beta\overline{\varepsilon}_p}), \tag{2.4}$$

in which the material coefficients are initial yield stress (k_0), stress difference between saturated stress and k_0 (Q) and the strain coefficient (β). $\overline{\varepsilon}_p$ is still true effective plastic strain. The final hardening curve of combined Swift-Voce hardening law is approximated by linear combination of the power and exponential law [12]:

$$\begin{aligned} \sigma_Y &= \alpha \cdot \sigma_s + (1 - \alpha) \cdot \sigma_v, \\ \sigma_Y &= \alpha \cdot A(\overline{\varepsilon}_p + \varepsilon_0)^n + (1 - \alpha) \cdot [k_0 + Q(1 - e^{-\beta\overline{\varepsilon}_p})]. \end{aligned} \tag{2.5}$$

As it can be seen in Figure 2.5, the Voce law expresses the strain hardening by the saturation

law, which means that the stress increase is zero at high plastic strains. On the other hand, the Swift law exhibits non-saturation hardening behaviour at high plastic strains. The linear combination of Swift and Voce law incorporates both saturating and non-saturating material behaviour through the use of weighting factor α, which plays important role in post-necking area.

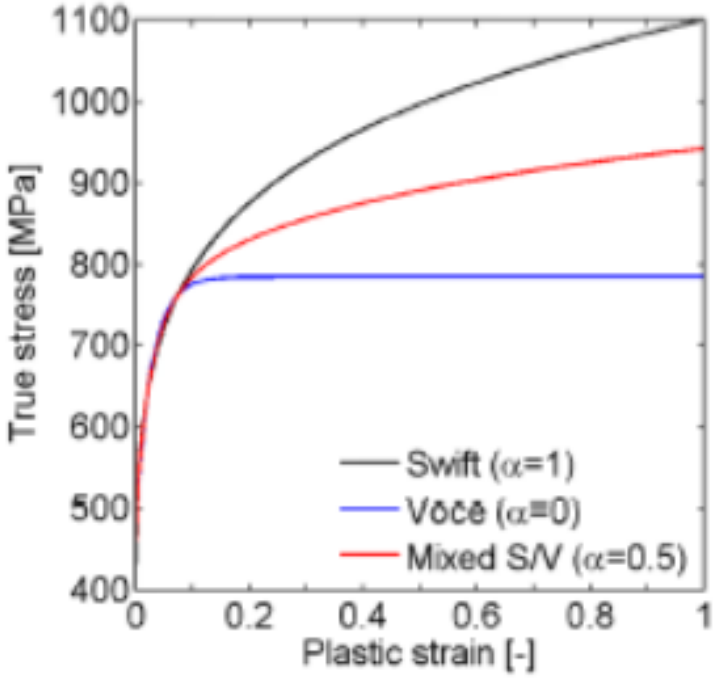

Figure 2.5: Stress-strain curves for Swift, Voce and Swift-Voce laws [13]

The usual way to gain material coefficients from equations (2.3) and (2.4) is through curve fitting of experimental true stress-plastic strain data up to the point of necking onset. For the purposes of this paper, a workflow has been developed to obtain material parameters and it is shown in Figure 2.6. Most of the experimental results are presented in the form of force-displacement curves or in the engineering stress-engineering strain data. Therefore, the true stress-true strain data must first be calculated from available engineering stress-engineering strain data by the following expressions:

$$\begin{aligned} \sigma_{true} &= \sigma_{eng} \cdot (1 - \varepsilon_{eng}), \\ \varepsilon_{true} &= \ln(1 + \varepsilon_{eng}). \end{aligned} \tag{2.6}$$

It is important to emphasize that this transformation is valid only until the ultimate tensile strength point, which is also onset of the significant necking. In addition, logarithmic plastic

strain is obtained by subtracting the elastic deformation from the total true strain:

$$\overline{\varepsilon}_p = \varepsilon_{true} - \frac{\sigma_{true}}{E}. \tag{2.7}$$

At this point, it is possible to combine true stress and plastic strain data, which is suitable for determining Swift and Voce material parameters. These points need to be approximated using the Swift law equation (2.3) and the Voce law equation (2.4) by some curve fitting tool, like *Matlab*. After the material coefficients of each law are identified, there is only one unknown parameter, weighting factor α, which is determined through inverse analysis using finite element method and *Abaqus* solver. The identification of α is posed as a minimization problem, as the difference between experimental and simulated force-displacement curve needs to be minimized. In order to correctly predict damage and fracture of the component, it is crucial to have an accurate strain hardening model of the material.

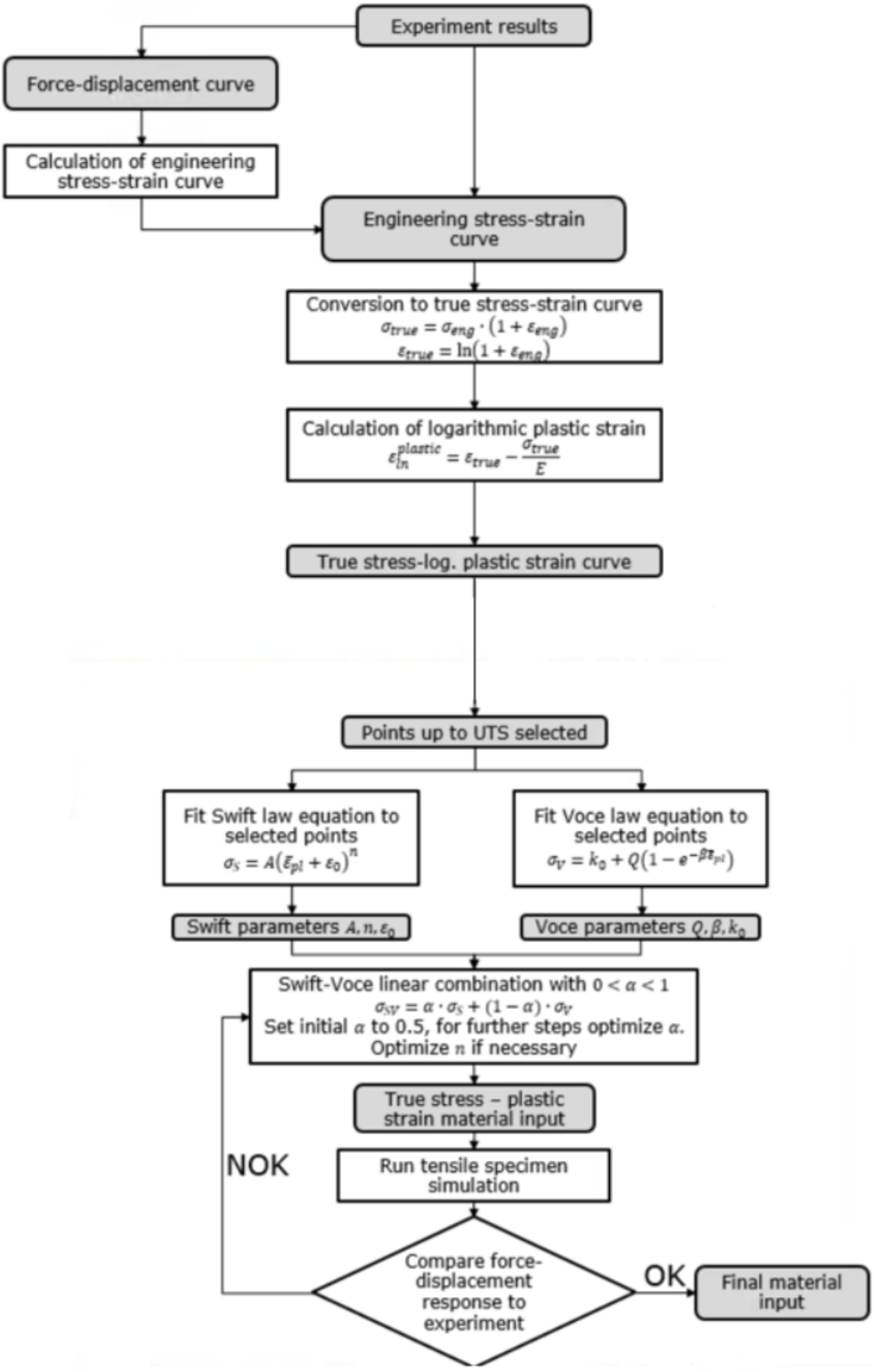

Figure 2.6: Swift and Voce material parameters determination workflow

2.3 Ductile damage

Depending on the material, there are two different types of fracture, brittle and ductile fracture. Brittle fracture occurs without development of large permanent plastic deformation, while the ductile materials exhibit significant plastic deformation before failure. Furthermore, due to large plastic deformation, crack growth during the ductile fracture is slowed. On the other hand, crack growth in brittle materials is sudden, as the whole fracture energy is concentrated in the crack tip. Some of the main reasons why it is desirable to use ductile materials when designing are the following:

- ductile materials deform very plastically and thus slow down the fracture process, which allows more time to eliminate the problem,
- in case of certain design errors, economic and other losses can be prevented by a prompt reaction,
- a larger amount of energy is required to deform ductile materials [14].

Ductile fracture occurs because of the imperfections in the material structure, which cause the nucleation of the voids (Figure 2.7 stage 1). As material deforms plastically, preexisting (primary) voids evolve and new ones nucleate, which reduces the internal resistance of the material (Figure 2.7 stage 2). Moreover, due to this void growth and nucleation, the porosity of the material increase and that results in formation of a primary band of localization at the mesoscale (Figure 2.7 stage 3). According to [15] and [16] the order of the inter-void spacing defines the width of a primary band of localization. As the result, the void growth and nucleation in the primary localization band is accelerated as it can be seen in stage 4 of Figure 2.7. Consequently, the porosity and the number of voids increases sharply in the zone of the primary localization and, as the material is subjected to further loading, the mechanical fields around individual primary voids begin to interact. This causes the localization of the voids nucleation and growth within secondary bands of localization at the microscale (Figure 2.7 stage 5 and 6). This bands are often several orders of magnitude smaller than primary localization band. The coalescence of voids inside the secondary localization band causes the creation and growth of the macroscopic cracks (Figure 2.7 stage 7), which lead to the complete material failure [12].

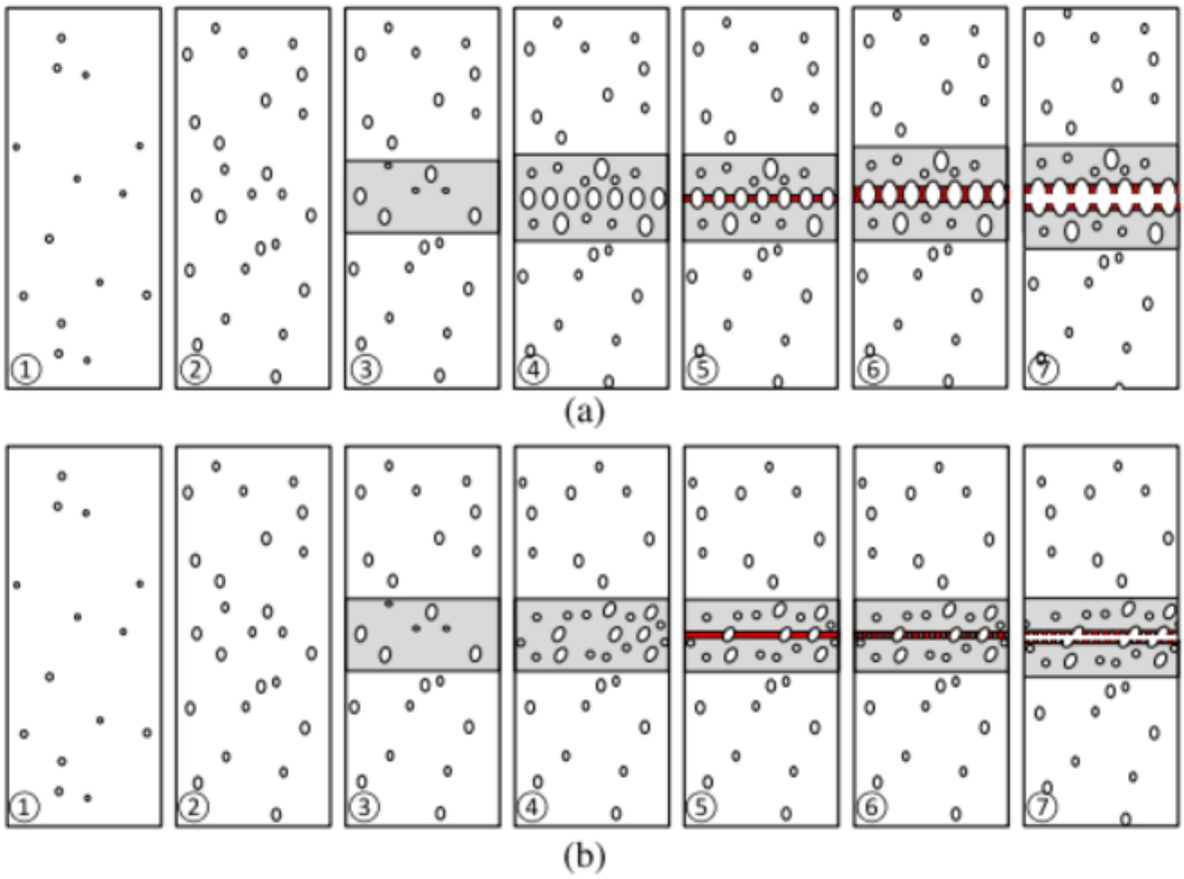

Figure 2.7: Schematic ductile fracture process [12]

The nucleation, growth and coalescence of voids in material pictured using computed tomography are shown in Figure 2.8.

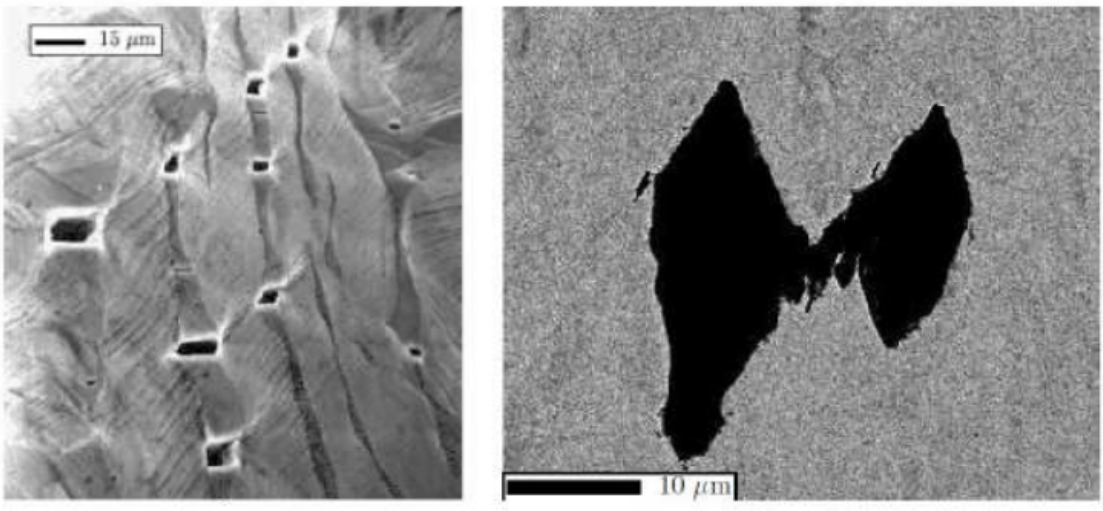

Figure 2.8: The nucleation and coalescence of voids [17]

The most of the research on ductile fracture have addressed the first stages of the failure process in order to prevent the voids initial nucleation and growth. In addition, numerous ductile damage models have been developed to predict the amount of damage

due to the nucleation, growth and coalescence of microcracks within the material. In attempt to model ductile damage, different authors have proposed several approaches, each of them leading to a number of damage models [18].

The first group of models is so called Gurson group of models, which try to represent directly the nucleation-growth-coalesce behaviour of voids. Hence, they are also known as micro-mechanical models. Rice and Tracey proposed the first void growth based damage model in 1969 in which the fracture was modelled as a series of processes of nucleation, growth and coalescence of micro voids [19]. Later, Gurson (1977) introduced a new damage parameter, the void volume fraction, and proposed porous plasticity fracture model [20]. Gurson's model was later improved by Tvergaard and Needelman (1984) [21].

The second approach is continuum damage mechanics method (CDM), in which the damage inside material is expressed as an internal parameter from a macro perspective and defects like nucleation are not studied individually. In these models the thermodynamic laws of irreversible processes was used to develop an expression for damage. The damage initiation and evolution could be represented only as function of plastic strains in the CDM. The foundations of these methods were set by Kachanov (1986) and it was later developed by Lemaitre, Desmorat and Bonora [22, 23, 24]. These authors proposed CDM models for ductile damage based on a linear and a logarithmic accumulation of damage.

Finally, in the phenomenological models, fracture is considered to occur when the damage indicator, expressed as stress or strain at a point in the material, reaches threshold value. These models are also called empirical models and they are focused on predicting material fracture rather than on characterising the evolution of damage. The model calibration consists in fitting the proposed ductility curve to the experimentally obtained fracture data. Therefore, an expression for for the equivalent plastic strain to failure ($\varepsilon^p_{eq,f}$) is proposed and material failure is considered when the equivalent plastic strain reaches that value ($\varepsilon^p_{eq} = \varepsilon^p_{eq,f}$). The most important models of this group were developed by Johnson and Cook (1985) [25], and by Xue and Wierzbicki (2008) [26].

2.3.1 Ductile fracture in *Abaqus* software

Since the *Abaqus* software was used for the simulation of ductile damage and fracture in this paper, the main principles of damage model implemented in *Abaqus* are studied in this section.

Abaqus supports a general framework for material fracture modelling and has the ability

to combine several different fracture mechanisms. In the most general case damage modelling requires the specification of the following:

- an elastic-plastic response of the material without implementation of damage (in this paper it is Swift-Voce hardening response),
- a damage initiation criterion,
- a damage evolution response, which includes the stiffness degradation and a choice of element removal.

Abaqus offers a variety of choices of damage initiation criteria for ductile metals, each associated with distinct types of material failure. Furthermore, it allows specifying multiple damage initiation criteria for the same material, which are treated independently. Once a certain damage initiation criterion is met, the material stiffness is degraded according to the specified damage evolution law for that criterion. However, if the material damage evolution law is not determined, the material stiffness is not degraded [27].

There are two main phenomenological mechanisms implemented to *Abaqus*, ductile criterion due to the nucleation, growth, and coalescence of voids and shear criterion due to shear band localization. These two damage initiation mechanisms call for different forms of the criteria for the onset of damage. Since the ductile initiation criterion is used in this paper, the above-mentioned criterion and the mechanism of ductile fracture are briefly described below.

The ductile criterion is a phenomenological model for predicting the damage initiation due to nucleation, growth and coalescence of voids or microcracks. The main assumption of this model is that the equivalent plastic strain at the onset of damage is a function of stress triaxiality and plastic strain rate:

$$\overline{\varepsilon}^{pl}_{\mathrm{D}}(\eta, \dot{\overline{\varepsilon}}^{pl}_{\mathrm{D}}), \tag{2.8}$$

where η is the stress triaxiality and $\dot{\overline{\varepsilon}}^{pl}_{\mathrm{D}}$ is the equivalent plastic strain rate. Furthermore, the criterion for damage initiation is met when the following condition is satisfied:

$$\omega_{\mathrm{D}} = \int \frac{\mathrm{d}\overline{\varepsilon}^{pl}}{\overline{\varepsilon}^{pl}_{\mathrm{D}}(\eta, \dot{\overline{\varepsilon}}^{pl}_{\mathrm{D}})} = 1, \tag{2.9}$$

where ω_{D} is a state variable that increases monotonically with plastic deformation [27]. At

each increment during the analysis the incremental increase in ω_{D} is computed as:

$$\Delta\omega_{\mathrm{D}} = \frac{\Delta\overline{\varepsilon}^{pl}}{\overline{\varepsilon}^{pl}_{\mathrm{D}}(\eta, \dot{\overline{\varepsilon}}^{pl}_{\mathrm{D}})} \geq 0. \tag{2.10}$$

As it is mentioned above, damage initiation depends on stress triaxiality η, which is defined according to the following equation:

$$\eta = -\frac{p}{q}, \tag{2.11}$$

in which p is the hidrostatic pressure stress and q is the Mises equivalent stress. These variables are calculated from the equations:

$$p = -\frac{\sigma_1 + \sigma_2 + \sigma_3}{3}, \tag{2.12}$$

and

$$q = \sqrt{\frac{1}{2}\left[(\sigma_1 - \sigma_2)^2 + (\sigma_2 - \sigma_3)^2 + (\sigma_3 - \sigma_1)^2\right]}, \tag{2.13}$$

where σ_1, σ_2 and σ_3 are the principal stresses [28]. Stress triaxiality can also be expressed by using the stress tensor invariants:

$$\eta = \frac{I_1}{3\sqrt{3J_2}}, \tag{2.14}$$

where I_1 is the first invariant of stress tensor ($\boldsymbol{\sigma}$) and J_2 is the second invariant of deviatoric stress tensor ($\mathbf{s}$) and they are calculated by the expressions:

$$I_1 = \mathrm{tr}[\boldsymbol{\sigma}], \tag{2.15}$$

and

$$J_2 = \frac{1}{2}\mathbf{s} : \mathbf{s}. \tag{2.16}$$

Deviatoric stress tensor $\mathbf{s}$ is calculated from the full stress tensor by:

$$\mathbf{s} = \boldsymbol{\sigma} - \frac{1}{3}I_1\mathbf{I}. \tag{2.17}$$

Aside from stress triaxiality and plastic strain rate, equivalent plastic strain at the onset of damage can be a function of Lode angle parameter, which is related to the third invariant of deviatoric stress. Combination of the stress triaxiality and the Lode angle parameter is very

useful for the stress state expression of isotropic materials [29]. Stress states of the isotropic material can be seen in Figure 2.9.

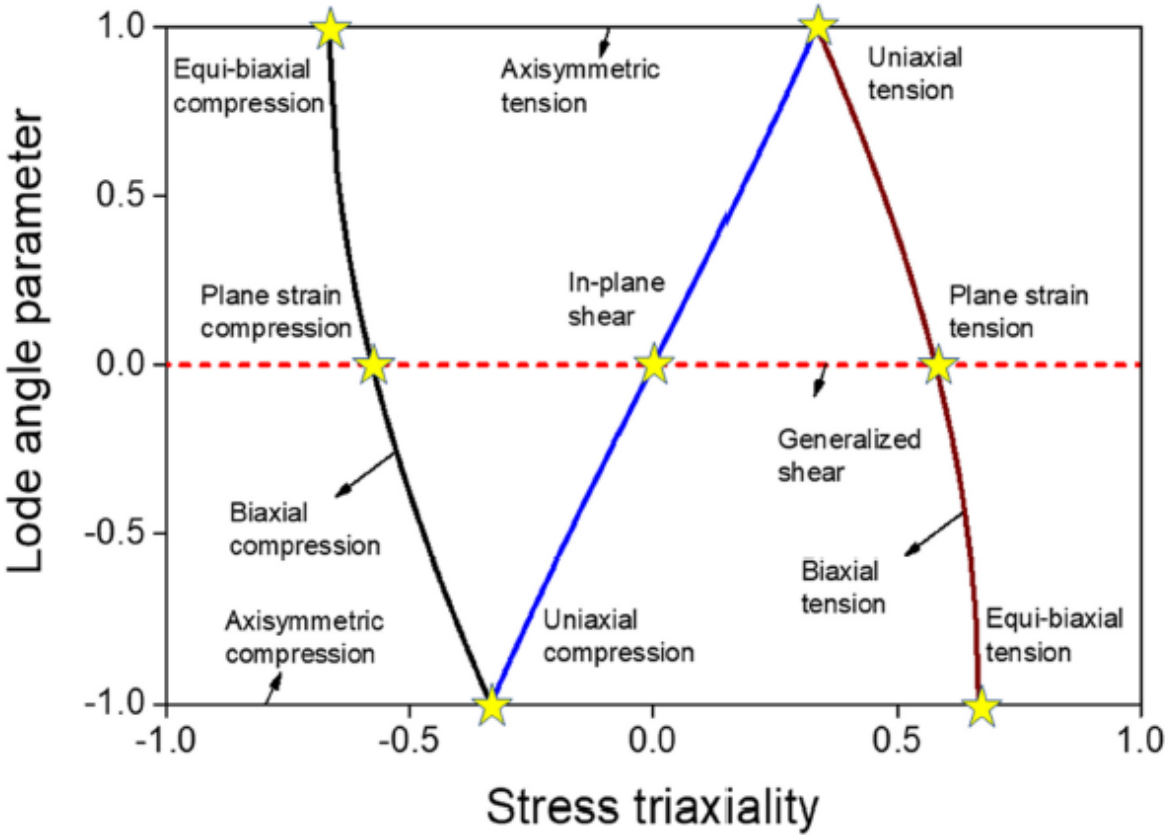

Figure 2.9: Stress states on the stress triaxiality and Lode angle parameter space [29]

The stress triaxiality has the values of in-plane shear ($\eta = 0$), uniaxial tension ($\eta = 1/3$), plane strain ($\eta = 1/\sqrt{3}$) and equi-biaxial tension ($\eta = 2/3$) in tension area $0 \leq \eta \leq 2/3$. The stress triaxiality rises as the material is undergoing a plastic deformation. During the static tensile test, the highest values of stress triaxiality will be in the critical area of the test sample in which the largest plastic deformations develop [28]. Since the no Lode angle parameter needs to be defined for the basic ductile criterion in *Abaqus*, only the dependence of stress triaxiality is used in this paper.

Once the ductile initiation criterion has been reached, the damage evolution law describes the rate of degradation of the material stiffness, leading to material failure. The stress tensor in the material is given by the scalar damage equation at any given time during the analysis:

$$\boldsymbol{\sigma} = (1 - D)\bar{\boldsymbol{\sigma}}, \tag{2.18}$$

where D is the overall damage variable and $\bar{\boldsymbol{\sigma}}$ is the undamaged stress tensor computed in current increment, i.e. the stress that would exist in the material in the absence of damage. The material has lost its load-carrying capacity when D=1 and that particular element is

removed from the mesh. It is important to emphasize that the damage evolution laws are strong mesh dependent.

Figure 2.10 shows the stress strain curve of the ductile material during the ductile damage initiation and evolution. The solid line represents the response of the material in the case of damage initiation and evolution, while the dashed line represents the response in the absence of damage. In elastoplastic materials with isotropic hardening, the ductile damage initiation and evolution cause gradual degradation of stiffness. Point c is the point of the damage initiation, with the corresponding ultimate yield strength σ_{y0} and the plastic strain at the onset of damage $\overline{\varepsilon}_0^{pl}$. Point c is followed by the softening, i.e. stiffness degradation up to the fracture marked by point d ($\overline{\varepsilon}_f^{pl}$ is the fracture plastic strain). The c-d curve depends on the parameters of the ductile damage, the stress triaxiality and the plastic deformation. Moreover, the c-d' curve is the material response without damage [27].

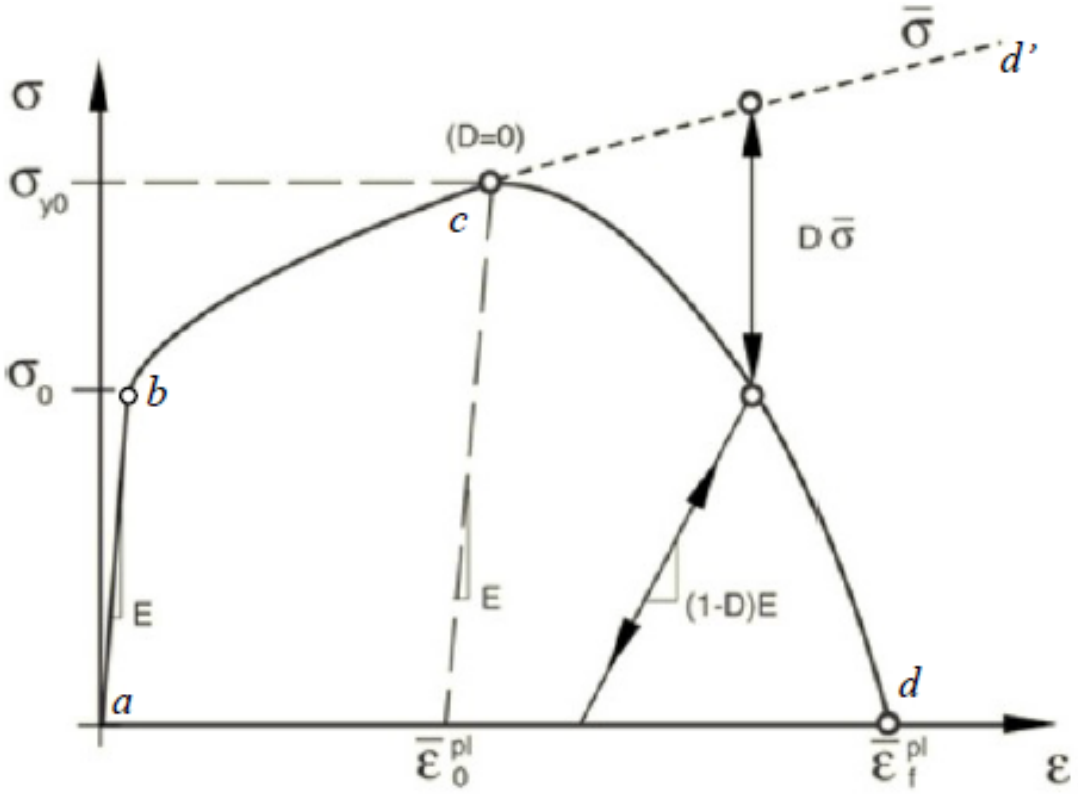

Figure 2.10: Stress-strain curve with progressive damage degradation [27]

The value of the equivalent plastic strain at failure, $\overline{\varepsilon}_f^{pl}$, depends on the characteristic length of the element and can not be used as a material parameter for the specification of the damage evolution law. Instead, the damage evolution law is specified in terms of equivalent plastic displacement, $\overline{u}^{pl}$, or in terms of fracture energy dissipation, G_f. In this paper, damage evolution was described by the equivalent plastic displacement.

Once the damage initiation criterion has been reached, the softening response is characterized by a stress-displacement response rather than a stress-strain response. The implementation of this stress-displacement concept in a finite element model requires the definition of a characteristic length associated with an integration point. The equivalent plastic displacement, $\overline{u}^{pl}$, is defined with the evolution equation:

$$\dot{\overline{u}}^{pl} = L\dot{\overline{\varepsilon}}^{pl}, \tag{2.19}$$

where L is the characteristic length of the element. The definition of the characteristic length depends on the element geometry and formulation. It is typical length of a line across an element for a first-order solid element, it is a half of the same typical length for a second-order element. For shells it is a characteristic length in the reference surface and for beams it is a characteristic length along the element axis. This definition of the characteristic length is used because the direction in which fracture occurs is not known in advance. Hence, elements with large aspect ratios will have rather different behavior depending on the direction in which they crack. However, some mesh sensitivity remains because of this effect, and elements that have aspect ratios close to unity are recommended [27].

3 Experimental procedure and numerical calibration of Swift-Voce parameters

In this chapter the specimen geometry, experimental procedure and the results obtained by the experiments on the sheet metals of 6005-T6 aluminium alloy are presented. Furthermore, numerical modelling of the strain hardening using a Swift-Voce law is shown.

3.1 Specimen geometry

In order to cover as many stress states as possible, the flat sheet metal specimens were made in several different geometries. Four types of tensile specimens covered the area of stress triaxiality from 0.33 to 0.57, i.e. from uniaxial tension to plane strain state. These geometries are selected based on the literature and paper of D. Mohr, *et al.* [30] and slightly modified. Moreover, three different types of shear specimen are selected in order to cover the zero triaxiality area, but due to similar results, only one type was used for the numerical modelling. Shear geometries are based on the study of Roth and Mohr [13]. Additionally, all geometry types were made of two plate thicknesses, 2 and 3 mm. Most importantly, all samples are cut along the extrusion direction with cutting tolerance within 0.01 mm. The tensile specimens are shown in Figure 3.1. The first tensile specimen is UT (uniaxial tension) specimen and the corresponding triaxiality in elastic region is constantly 0.33. As the material undergoes the plastic strain, triaxiality rises. Its gage section is 10 mm wide. The following two tensile specimen are made with the circular cutouts of 20 mm and 6.67 mm radius, known as NT20 and NT6 respectively, and they cover triaxiality area form 0.4 to 0.57. These specimens are 20 mm wide but the notches reduce the width of the gage section to 10 mm in center. The last tensile specimen features a 20 mm wide gage section with an

5 mm diameter hole in the center. Hence, it is called CH specimen (central hole).

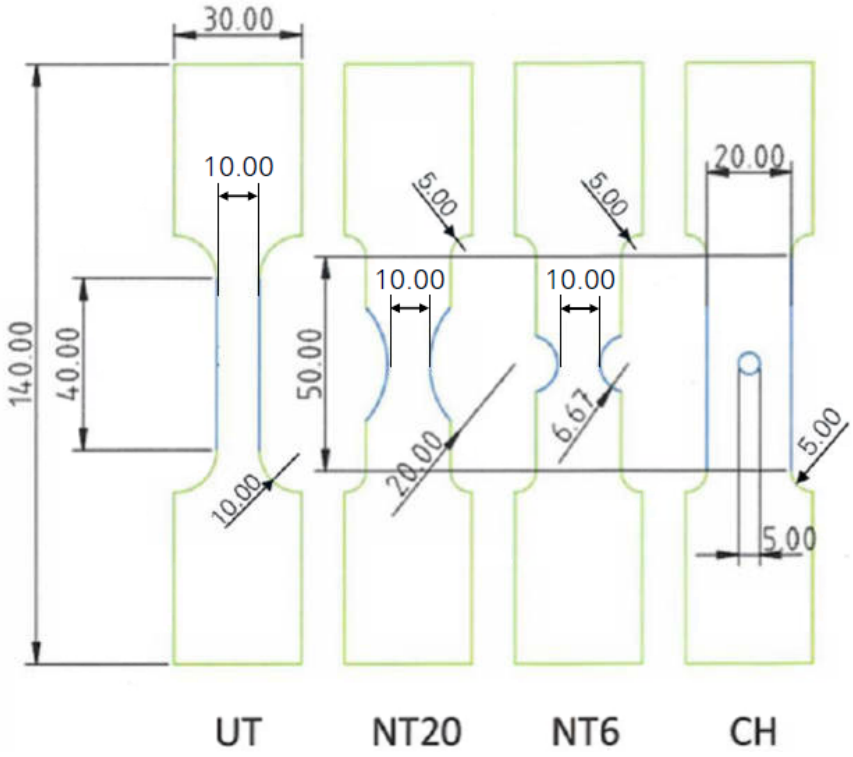

Figure 3.1: Tensile specimens geometry

In practice, there are numerous shear test specimens which are suitable for different types of materials. Shear test specimens from Figure 3.2 are suitable for all types of hardening behavior, depending on the degree of ductility [13].

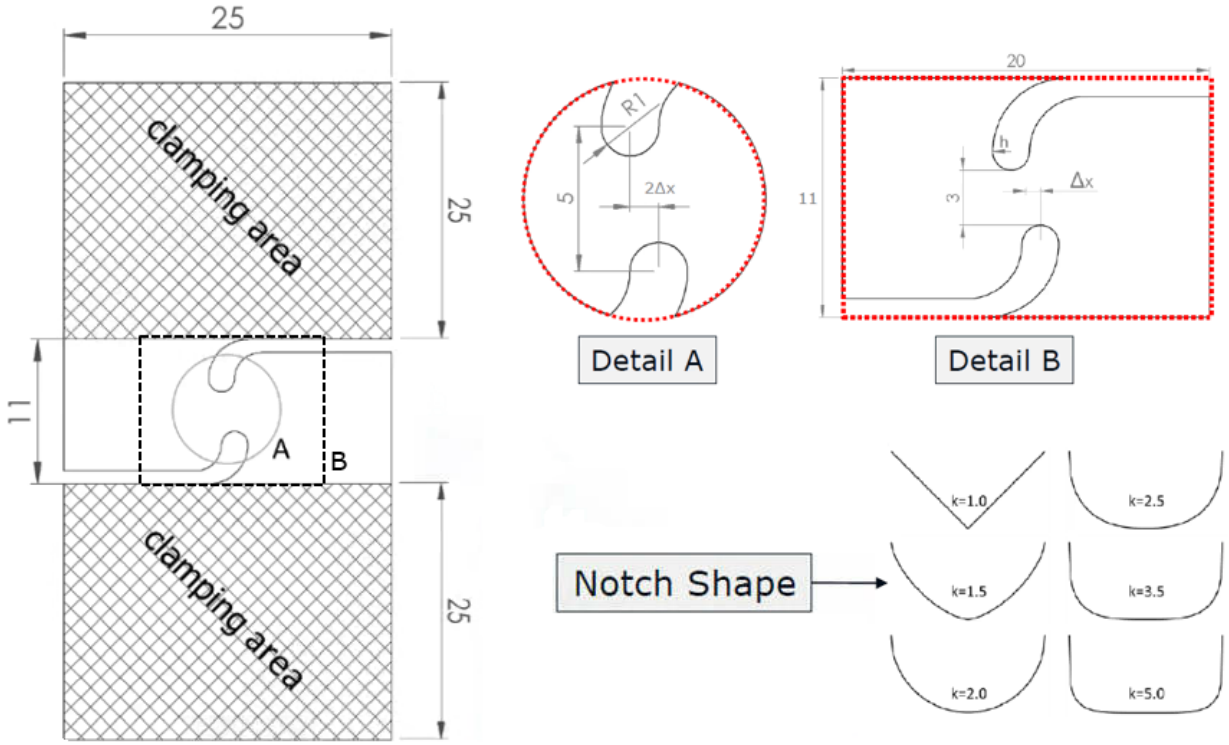

Figure 3.2: Shear specimens geometry

Notch shape is defined by the parameters k and h according to the following equation with x-y coordinate frame:

$$y = (h^k - |x|^k)^{\frac{1}{k}}, \tag{3.1}$$

with h describing half of the overall notch width. The blunter the notch shape is, there will be more damage accumulated in the center of the specimen which leads to fracture initiation under a shear stress state within the gage section. Moreover, geometry is also defined by the notch offset (Δx). A larger offset leads to higher accumulation of plastic strains in the gage section. These parameters must be properly defined, in order to ensure a fracture location in the gage section as well as avoiding the formation of a critical condition at the free boundary of the specimen. Depending on the parameters h, k and Δx, shear specimens are separated in three categories.

- SH-LD specimen which is suitable for "low" ductility materials. It is the combination of a large offset (Δx=0.8 mm) and blunt notch (k=3.25).
- SH-MD specimen: the combination of a medium offset (Δx=0.65 mm) and an approximately circular notch (k=2.25). Suitable for materials with moderate ductility.
- SH-HD specimen is characterized by a pointed notch (k=1.75) and a small offset (Δx=0.5 mm). Suitable for highly ductile materials.

The half of the overall notch width h is 1 mm for all three specimens. As the material ductility in shear condition is not known a priori, it is recommended to conduct testing of all three specimen geometries [13].

3.2 Experimental setup

As part of this research, measurements on force, displacement and strain fields were performed on the above-mentioned specimens. The experimental measurements were conducted on the universal tensile machine *Inspekt 20-1* of the German manufacturer *Hegewald & Peschke* in cooperation with the company *Topomatika*. Force results of tested specimens were directly extracted from tensile machine data. Furthermore, displacement and strain fields were obtained by the *Aramis* software and the digital image correlation method (DIC method). This method is non-contact optical method that is based on monitoring the changes of the points positions on the test sample surface such that the

position of measured point in the deformed state is compared with its position in undeformed state. Therefore, one or more measuring cameras are required and in this work *ATOS Core* optical measuring system was employed. Prior to testing, a random speckle pattern is applied to the specimens in order to monitor the displacement of the specific points. Digital images and the surface of the specimen are discretized by smaller fields of pixels called subsets of facets which form a measuring volume. In the center of each facet is a central point which is the measuring point in which the displacement and deformation results are saved. The result of this method are full displacement and strain fields on the specimen surface inside the measuring volume. For the purpose of this paper, two digital images were recorded every second in each measurement (2 Hz recording resolution). The described experimental setup is shown in Figure 3.3.

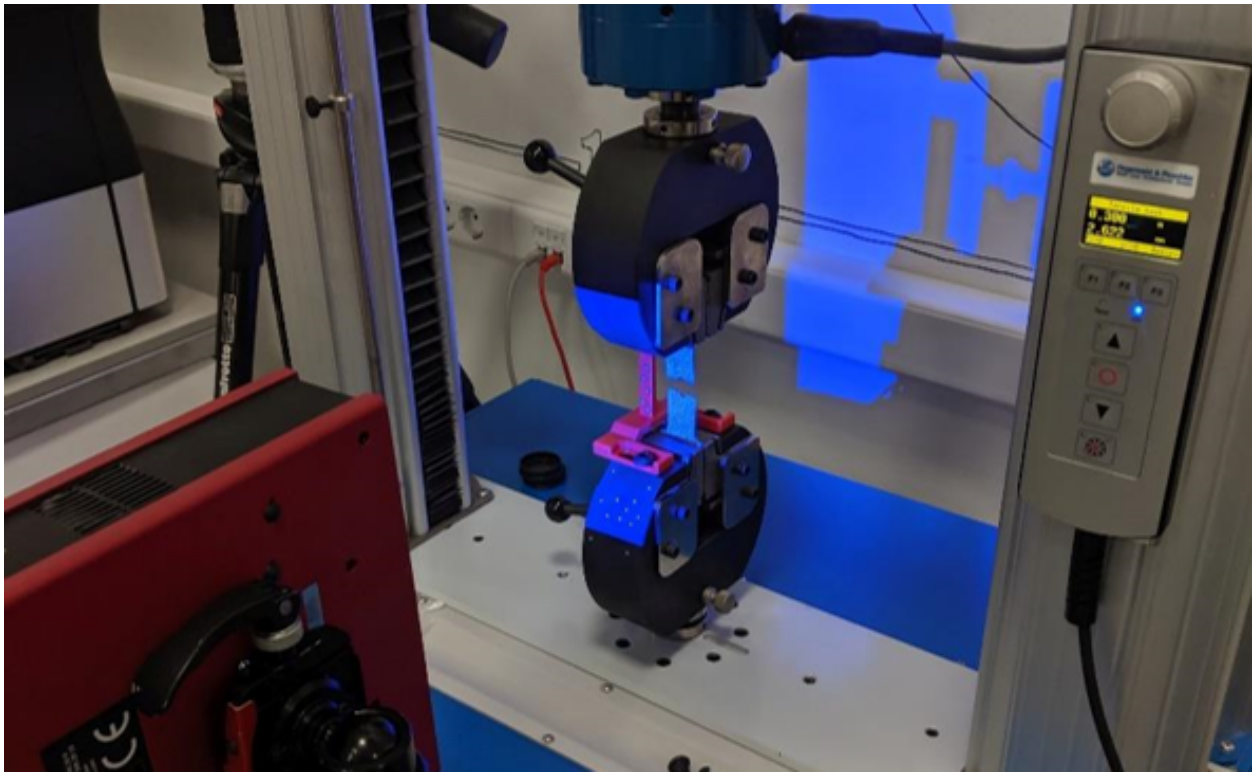

Figure 3.3: Measuring setup

All the tests were conducted at room temperature of $20 \pm 1°C$. Moreover, in order to ensure a quasi-static response, all tests were performed with the loading rate 1 mm/min. Thus, strain rates of observed specimens are low and inertial effects can be neglected. The measuring volume size of 45 mm with pixel size of 0.0018 mm was selected for tensile specimens, because this provided a satisfactory number of measuring points. However, due to the small geometry of the shear specimens, the measuring volume of 5 mm was chosen for them.

3.3 Experimental force-displacement results

A total of 112 specimens, 8 units of each 7 different specimens on two plate thickness, were available for the measurement. Obtained results for 2 mm tensile specimens are shown in Figure 3.4. As mentioned earlier, force data were obtained from tensile machine data. In addition, the relative displacement of two points on the specimen surface was measured in all experiments by means of digital image correlation, using a *GOM Correlate* software. These points are located on the longitudinal symmetry axis and the initial distance between these points is 20 mm, 10 mm above and below the center of each specimen.

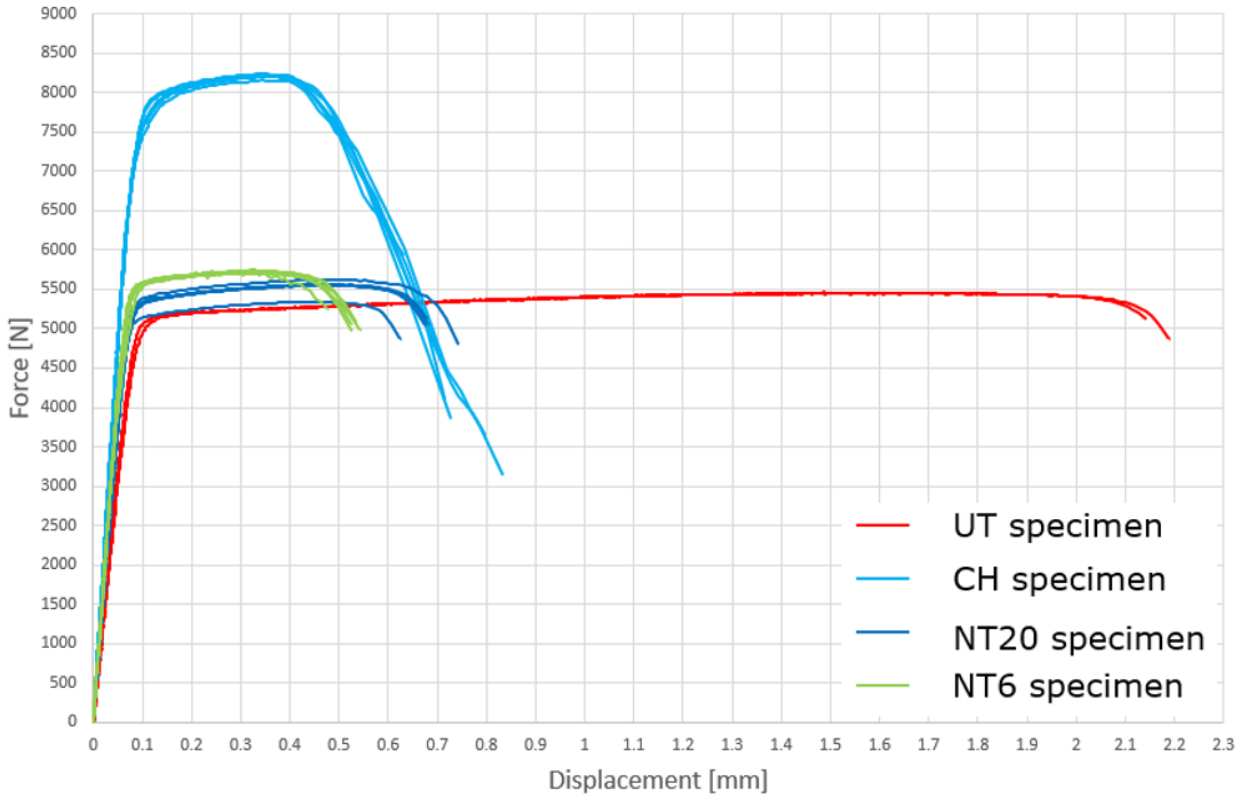

Figure 3.4: Force-displacements results of 2 mm tensile specimens

According to Figure 3.4 the UT specimen exhibits the greatest elongation until the fracture. Moreover, due to damage to the speckle pattern coating on the specimen surface and fractures outside the measuring volume, only two valid results of UT specimens were obtained. All experiments show a force maximum prior to the onset of fracture. However, the CH specimen exhibits significantly the highest force level. Furthermore, it is remarkable that the decrease in force, between the fracture initiation and the failure, is similar for UT, NT20 and NT6 specimens, while the fracture propagation is most pronounced for CH specimens. Also, no significant difference is observed in measured force-displacement results

of each specimen type. Hence, only one sample of each specimen is selected for hardening and damage calibration.

Force-displacement results of 3 mm tensile specimens (Figure 3.5) show similar behavior as results of 2 mm specimens. The highest elongation is again achieved for the UT specimen. Only one UT specimen result was extracted because of fractures in upper or lower parts of the gage section as well as the coating damage. Due to increased stiffness of the specimens, the force level is higher than that of the 2 mm specimens (Figure 3.4), with force reaching its maximum for CH specimen. Damage evolution of thicker specimens is significantly greater for all types. UT, NT20 and NT6 specimens again have similar fracture behavior. CH specimen is used for damage evolution calibration, because of the most pronounced fracture propagation for both thicknesses. One force-displacement curve of each specimen is used for hardening and damage calibration in the same way as for 2 mm specimens.

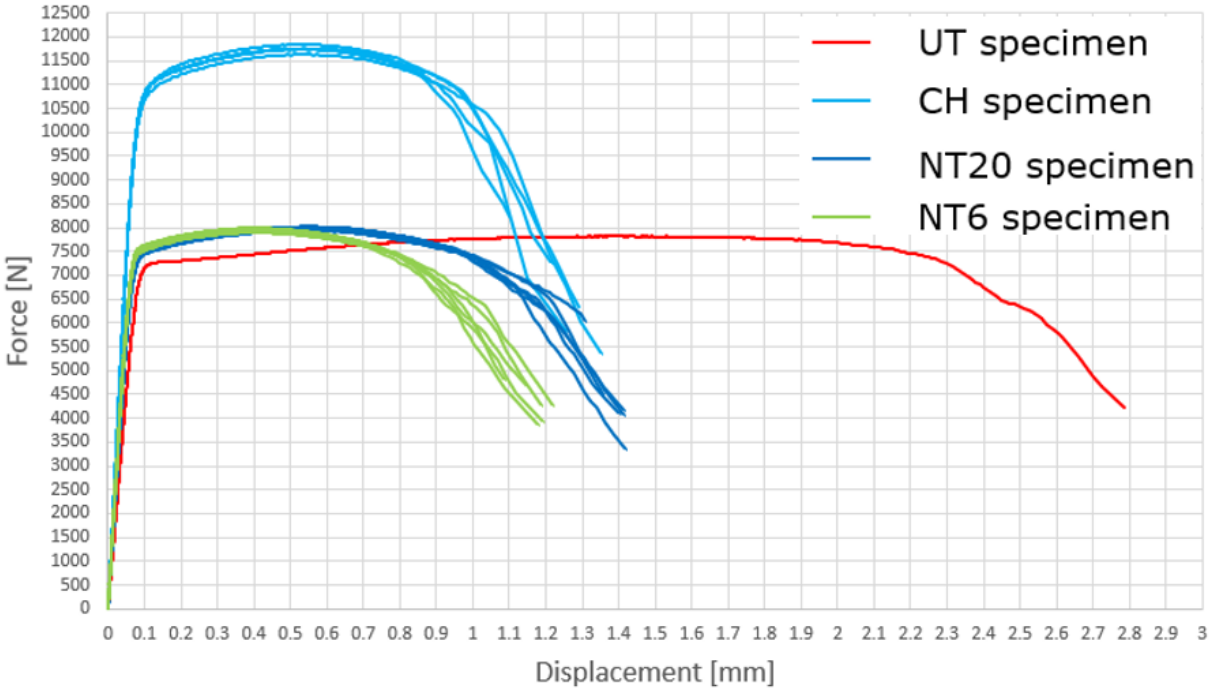

Figure 3.5: Force-displacements results of 3 mm tensile specimens

In addition to tensile specimens, experiments with the shear specimens were also conducted. The samples (shown in Figure 3.2) were clamped and subjected to tensile loading. Due to the specific geometry in central area, the fracture occurs under shear stress state. Force data was directly extracted from tensile machine. Relative displacement for shear specimens was measured between two points on the line perpendicular to the shear zone and 3 mm apart (Figure 3.6). The displacement component vertical to the extrusion direction was not negligible, so the in-plane relative displacement was calculated.

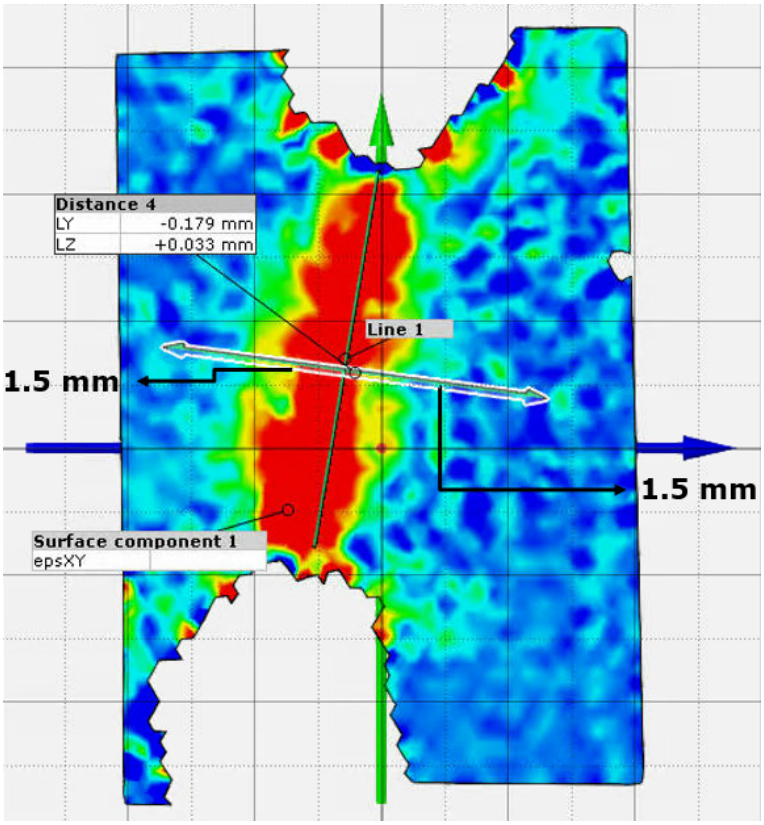

Figure 3.6: Displacement extraction points for shear specimen

As seen in the Figure 3.7, all types of the shear specimens have similar response. The results on an enlarged scale are shown in a dashed square and visible in Figure 3.8.

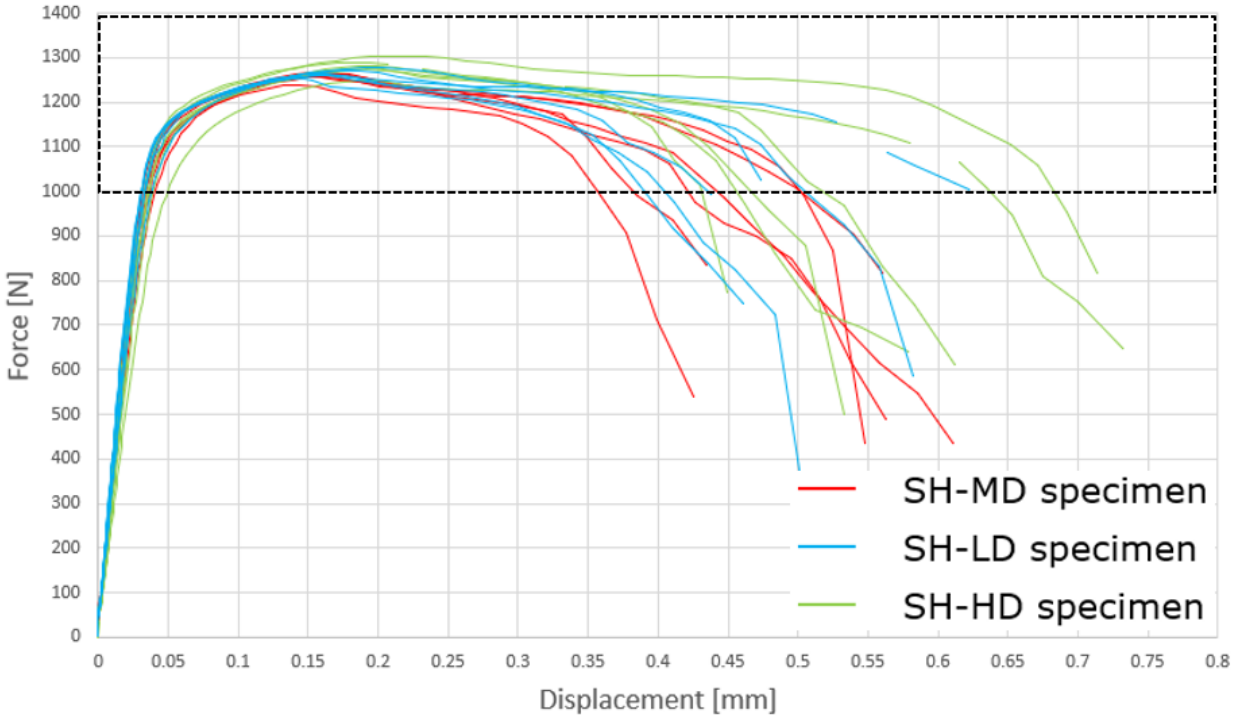

Figure 3.7: Force-displacements results of 2 mm shear specimens

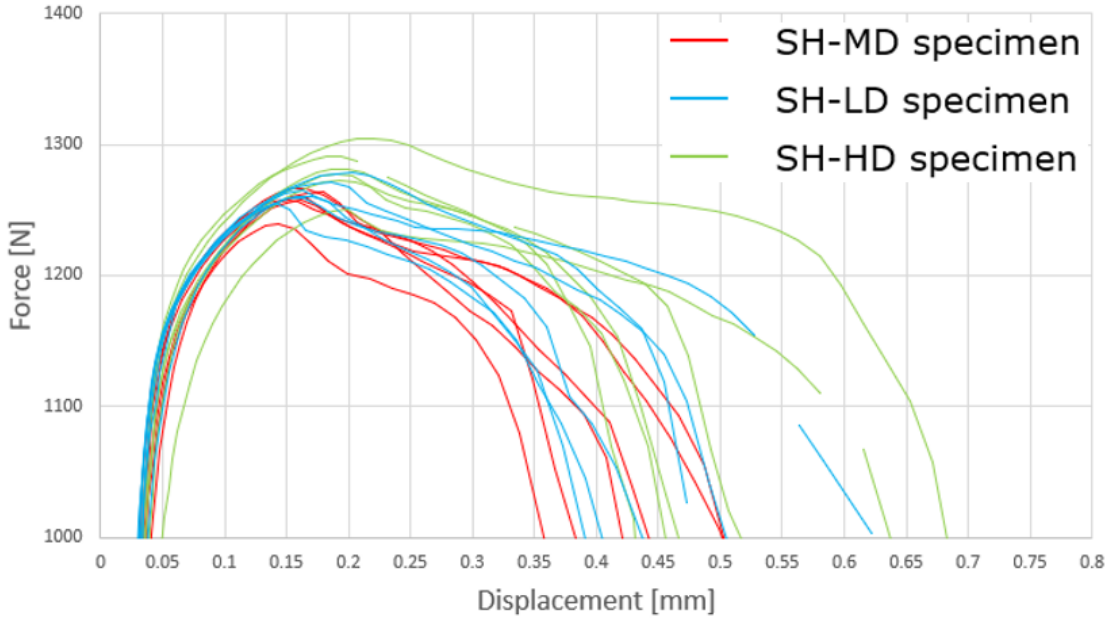

Figure 3.8: Force-displacements results of 2 mm shear specimens-detail

The highest achieved force is significantly smaller than in the tensile specimens. Moreover, the fracture occurred quickly, so a smaller number of images were taken. This results in a large displacement, force and strain increase in a single step. Therefore, the determination of the correct fracture initiation moment is difficult. Force decrease after the fracture initiation and damage evolution is very pronounced for all shear specimens. Due to similar response, only one type of shear specimen is selected for damage calibration. It is a SH-MD specimen, because of its "medium" properties and suitability for materials with moderate ductility.

Shear specimens of 3 mm thickness were cut with notch along the extrusion direction by mistake (Figure 3.9).

Figure 3.9: Shear specimen 3 mm

During the loading, damage was localized along the notch and the failure occurred because of the notch effect. Hence, the results for 3 mm specimens could not be used for calibration of ductile damage parameters, and they are not included in this master thesis.

3.4 Numerical quasi-static analysis

In order to determine the Swift-Voce hardening parameters, it is necessary to use numerical simulations. *Abaqus* software, based on the finite element method, was used for the purpose of this research. All specimen geometries were discretized using first order solid hexahedron with reduced integration, C3D8R (Figure 3.10). This type of element has 8 nodes with 3 translation degrees of freedom (DOF) for each node, total 24 DOFs. Reduced integration was used to reduce the computational time and to avoid shear and volumetric locking [27]. Every specimen was prepared for numerical simulation in *Abaqus/Explicit* by using an *ANSA* pre-processor, which is widely used in automotive industry.

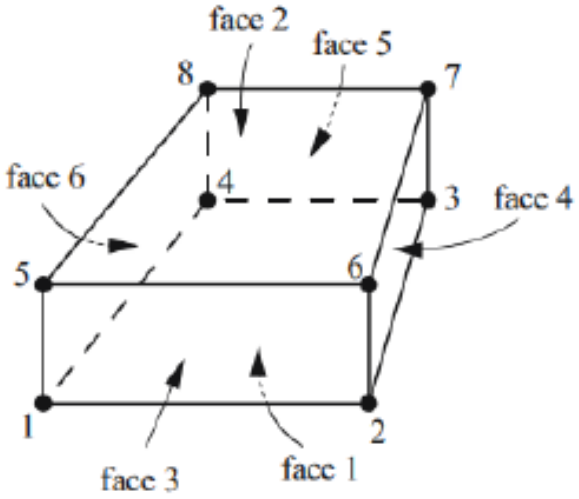

Figure 3.10: C3D8R element [27]

3.4.1 Quasi-static analysis using *Abaqus/Explicit*

High-speed numerical analysis, including material stiffness degradation due to damage, are generally performed using *Abaqus/Explicit*, whereas performing such analyses in *Abaqus/Implicit* usually causes convergence difficulties. Explicit analysis are performed in a large number of increments, in which the solution is determined without iterating by explicitly advancing the kinematic state from the end of the previous increment. At the

beginning of the increment *Abaqus/Explicit* solves the dynamic equilibrium equation:

$$\mathbf{M} \cdot \ddot{\mathbf{u}} = \mathbf{P} - \mathbf{I}, \tag{3.2}$$

where $\ddot{\mathbf{u}}$ is the vector of nodal acceleration, $\mathbf{M}$ is the nodal mass matrix and $\mathbf{P}$ and $\mathbf{I}$ are respectively the vector of external forces and the vector of internal element forces, respectively. The vector of nodal accelerations at the beginning of the increment (time t) is calculated from equation:

$$\ddot{\mathbf{u}}|_{(t)} = \mathbf{M}^{-1}(\mathbf{P} - \mathbf{I})|_{(\mathbf{t})}. \tag{3.3}$$

Furthermore, the nodal velocities at the middle of the current increment are calculated by accelerations integration through time using the central difference rule, and addition to the velocity at the middle of the previous increment:

$$\dot{\mathbf{u}}|_{(t+\frac{\Delta t}{2})} = \dot{\mathbf{u}}|_{(t-\frac{\Delta t}{2})} + \frac{\Delta t|_{(t+\Delta t)} + \Delta t|_{(t)}}{2} \cdot \ddot{\mathbf{u}}|_{(t)}. \tag{3.4}$$

The calculated nodal velocities are integrated and through time and added to the displacements at the beginning of the increment to obtain the nodal displacements at the end of the increment:

$$\mathbf{u}|_{(\mathbf{t}+\mathbf{\Delta t})} = \mathbf{u}|_{(\mathbf{t})} + \mathbf{\Delta t}|_{(\mathbf{t}+\mathbf{\Delta t})}\dot{\mathbf{u}}|_{(\mathbf{t}+\frac{\mathbf{\Delta t}}{\mathbf{2}})}. \tag{3.5}$$

The state at the end of the increment $(t + \Delta t)$ is based solely on the displacements, velocities, and accelerations at the beginning of the increment (t). This method assumes that accelerations are constant during an increment, so in order to produce the accurate results, the time increment must be quite small. Therefore, the analyses usually require a large number of increments. However, each increment is computational inexpensive because there are no simultaneous equations to solve. The key to the computational efficiency is the use of diagonal and lumped nodal mass matrix $\mathbf{M}$. This results in uncoupled equations of motion and therefore no tangential stiffness calculation is required for explicit analysis. Moreover, the inversion of $\mathbf{M}$ is trivial, which reduces the cost of the analysis. [27, 31].

The size of the increment, in which the state can be advanced and still remain an accurate representation of the problem, is limited by the stability factor. A possible effect of exceeding the stability limit is a numerical instability and inaccuracy. The stability limit is calculated based on the highest frequency of the observed structure, the calculation of which is not computationally feasible. Hence, it is generally not possible to determine the

stability limit exactly, so conservative estimates are used instead. The estimation of the stability limit, which is efficient and conservative, is calculated by the following expression:

$$\Delta t \approx \frac{L_{min}}{c_d}, \tag{3.6}$$

where L_{min} represents the smallest element dimension and c_d represents the dilatational wave speed. The shorter the element length, the smaller the stability limit. The dilatational wave speed is the material property and it is calculated using the equation:

$$c_d = \sqrt{\frac{E}{\rho}}, \tag{3.7}$$

where ρ is the mass density and E is Young's modulus. Since the stable time increment is estimated based on the dilatational wave speed, the stability limit represents the smallest time required for the dilatational wave to cross any element of the mesh [31].

Energy balance is an important part of the *Abaqus/Explicit* analyses accuracy assessment. The total energy of the entire model consist of several components, and it should be constant:

$$E_{Total} = E_I + E_{FD} + E_V + E_K + E_{IH} - E_W - E_{PW} - E_{CW} - E_{MW} - E_{HF} = \text{constant}, \tag{3.8}$$

where E_I is the internal energy, E_{FD} is is the frictional dissipated energy, E_V is the viscouss dissipated energy, E_K is the kinetic energy and E_{IH} is the internal heat energy, whereas E_W, E_{PW}, E_{CV} and E_{MW} are respectively the work done by the external applied loads and the work done by contact penalties, constraint penalties and added mass. Lastly, E_{HF} is the energy developing through external fluxes. Additionally, the internal energy is the sum of the recoverable elastic strain energy, E_E, the energy dissipated through inelastic processes such as plasticity, E_P, the energy dissipated through viscoelasticity or creep, E_{CD}, the artificial strain energy, E_A, the energy dissipated through damage, E_{DMD}, the energy dissipated through distortion control, E_{DC}, and the fluid cavity energy, E_{FC}:

$$E_I = E_E + E_P + E_{CD} + E_A + E_{DMD} + E_{DC} + E_{FC}. \tag{3.9}$$

The artificial strain energy , E_A, includes energy stored in hourglass resistances and transverse shear in shell and beam elements. Large values of artificial strain energy indicate that mesh refinement is necessary.

Furthermore, in quasi-static analyses inertia effects are negligible because of low strain rates of observed structure. If a quasi-static analysis is performed in its natural scale, the solution should be almost the same as a truly static solution. However, it is computationally impractical to model the process in its natural time period because millions of time increments would be required. Hence, artificially increasing the speed of the process in simulation is necessary to obtain an economical solution, while preserving negligible inertial effects. Due to significant inertial forces, the solution tends to localize resulting in e.g. excessive local plastic deformation. The often used approach to obtain economical quasi-static solutions with an explicit dynamic solver is increasing the loading rates, as long as the inertial forces are still insignificant. Preservation of the quasi-static response is ensured by the energy control, whereas the ratio of kinetic to internal energy does not exceed 10% throughout the analysis. Hence, the work done by the external applied loads is approximately equal to the internal energy of the system (Figure 3.11) [27, 31].

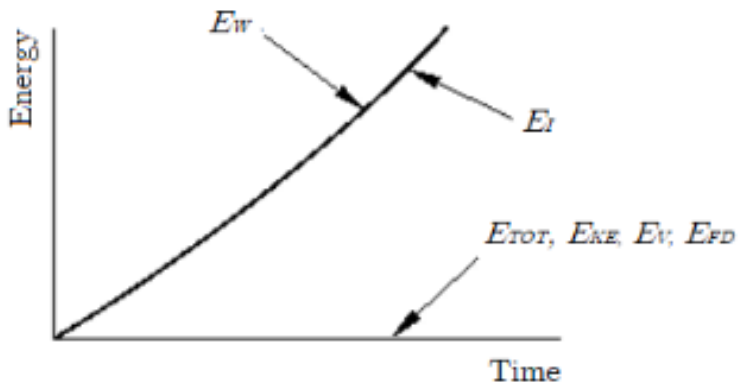

Figure 3.11: Energy distribution in quasi-static analysis [27]

In a quasi-static analysis the first mode of the structure usually dominates the response Therefore, the loading rates are estimated on the period of the lowest mode natural frequency. Increased loading rates reduce the time scale of the simulation, with fewer increments needed to complete the job. However, inertial forces become more dominant with increased loading rates. Hence, the fastest loading rate without the inertial effects and localization should provide the quasi-static response with the most economical solution and accurate results [31].

3.4.2 Loading rate determination

In order to accelerate the simulation, an appropriate loading rate, which ensures the quasi-static response, should be defined. The loading rate of the experiment is slow, just 1 mm/min, therefore the simulation loading rate is artificially increased. The workflow for loading rate definition is displayed in Figure 3.12.

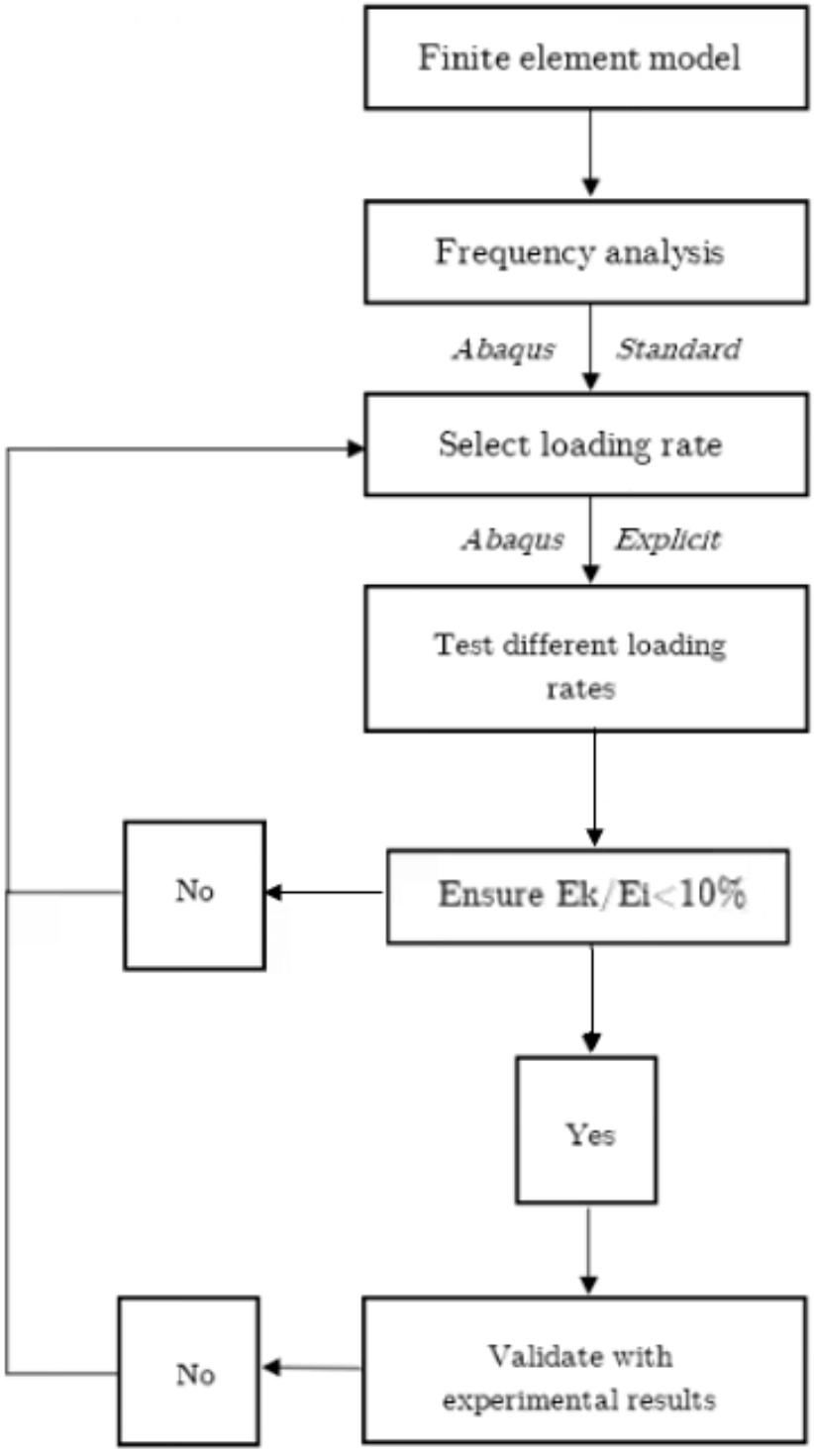

Figure 3.12: Appropriate loading rate definition algorithm [31]

As noted above, the first structural mode dominates the response of the quasi-static analysis. Hence, the loading rate is estimated on the period of the lowest natural frequency. The natural frequency can be calculated easily in *Abaqus/Standard*. Moreover, the truly quasi-static solution is ensured if the loading time is 10 times greater than the period of the lowest frequency mode. Usually, the quasi-static response is ensured if the loading duration is at least 3 to 5 times greater than the period of the lowest frequency [27].

The UT specimen mesh is used to evaluate the effect of the mesh density on the fundamental frequency. The meshes are shown in the Figure 3.13. The approximate size of the C3D8R elements in gage section is 2.5 mm, 1 mm, 0.5 mm and 0.2 mm respectively.

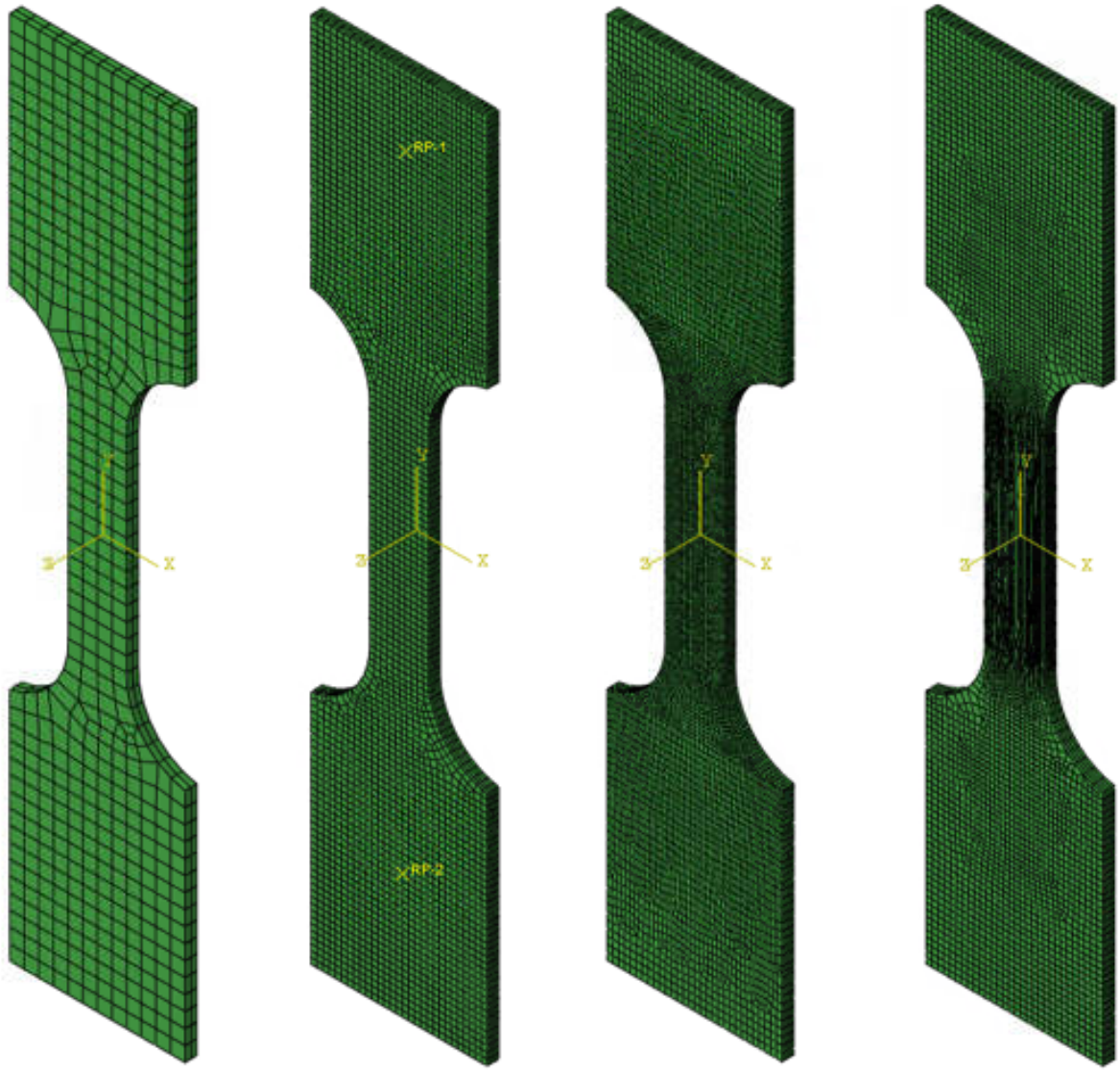

Figure 3.13: UT specimen meshes with C3D8R elements of different size

In order to determine appropriate loading rate, the first natural frequency of the 2 mm UT specimen is converged with respect to the size of the C3D8R elements in gage section.

The values of the frequency are listed in Table 3.1.

Table 3.1: Values of first natural frequencies of UT 2 mm specimen

C3D8R element size, mm	f_1, Hz
2.5	2165.1
1	2305.2
0.5	2327.0
0.2	2333.9

Furthermore, the tabular results from Table 3.1 are visualized in Figure 3.14.

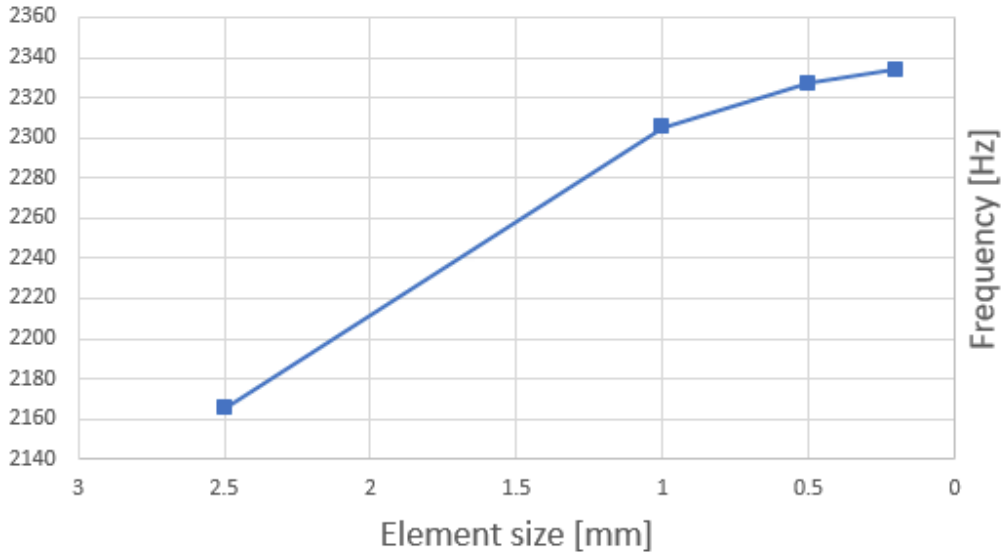

Figure 3.14: Frequency values for different element sizes

As it can be seen in Table 3.1 and Figure 3.14, an element size has significant influence on the value of the fundamental frequency. The difference between frequencies of 2.5 mm and 1 mm element size is much greater than the difference between 1 mm and 0.5 mm. Moreover, the first natural frequency does not change significantly with the element size reduction from 0.5 mm to 0.2 mm. In addition, further element size reduction would lead to increased simulation duration and less computational efficiency. Therefore, the numerical model consisting of C3D8R elements with size of 0.5 mm in gage section is used for tensile specimens to obtain correct and economical solution. The period of the lowest frequency for an element size of 0.5 mm is 0.4297 ms. Since the approximate quasi-static loading rate highly depends on the increase of the period of the lowest frequency, different loading rates were evaluated. The energy distribution for different loading rates is displayed in the following figure.

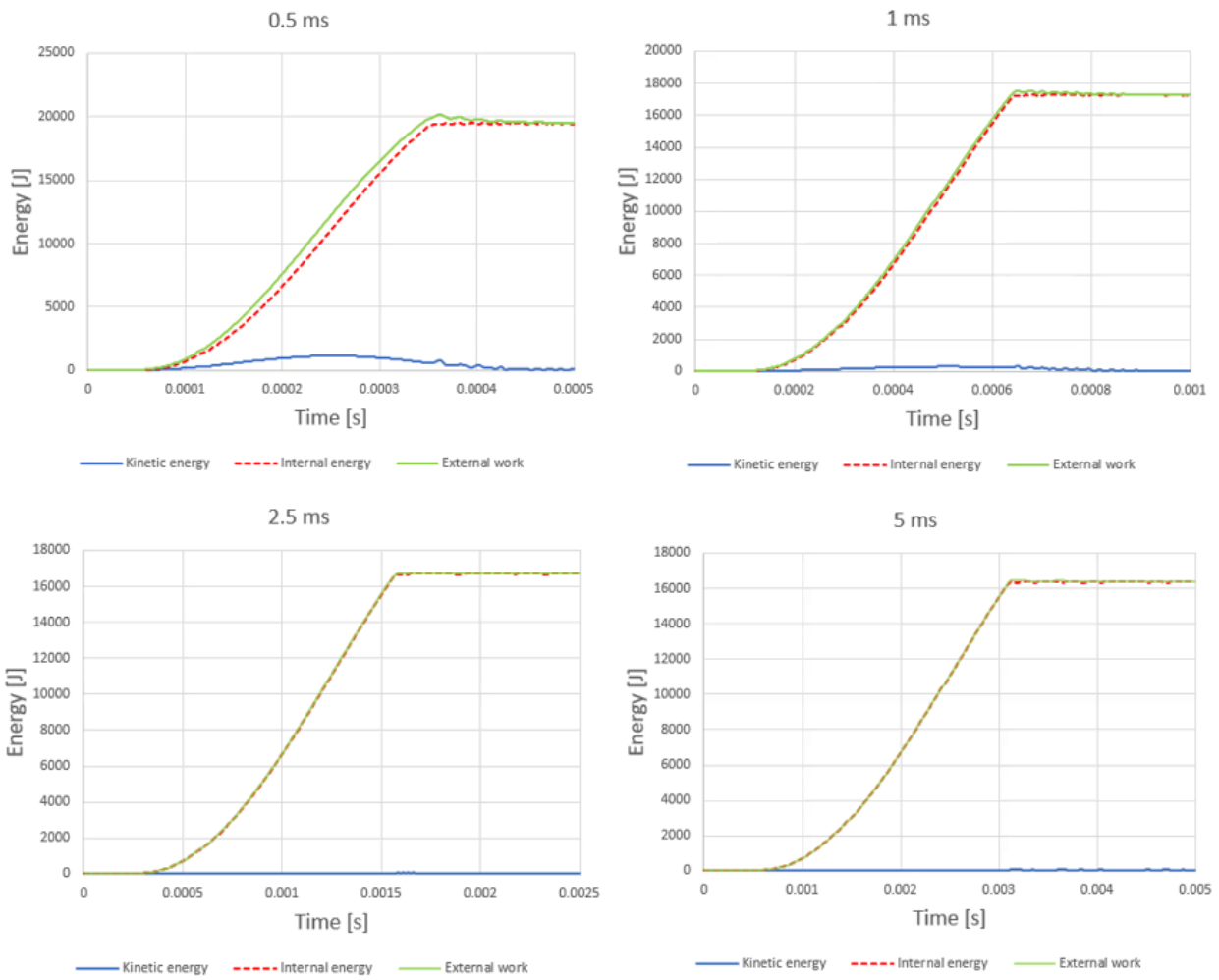

Figure 3.15: Energy distribution during quasi-static analyses with different loading rate

As it can be seen in Figure 3.15, the energy conservation criterion ($(E_k/E_i)\cdot 100 < 10\%$) is not satisfied for 0.5 ms loading rate, due to the significant inertial effects. The inertial effects are completely eliminated for the simulation duration time at least 3 times higher than the period of the lowest frequency. According to the recommendations in [27], the loading rate 10 times greater than the period of the fundamental frequency is selected for the numerical quasi-static analyses. Moreover, the simulation duration of 5 ms ensures the quasi-static response for all specimen types and both thicknesses.

3.4.3 Numerical model

Every specimen geometry was prepared in *ANSA* pre-processor to match the actual conditions of the experiment. Two clamping areas, shown in Figure 3.16, were modelled to suit the experimental clamping areas. The lower clamping zone was coupled with the reference point, in which all degrees of freedom were fixed. Furthermore, the displacement load in the extrusion direction was applied in the upper reference point, which is coupled with

the upper clamping zone. All other degrees of freedom were fixed for this point, except for the shear models. Due to the observed shift in the transverse direction during the experimental measurement of the shear specimens, the transverse degree of freedom is allowed.

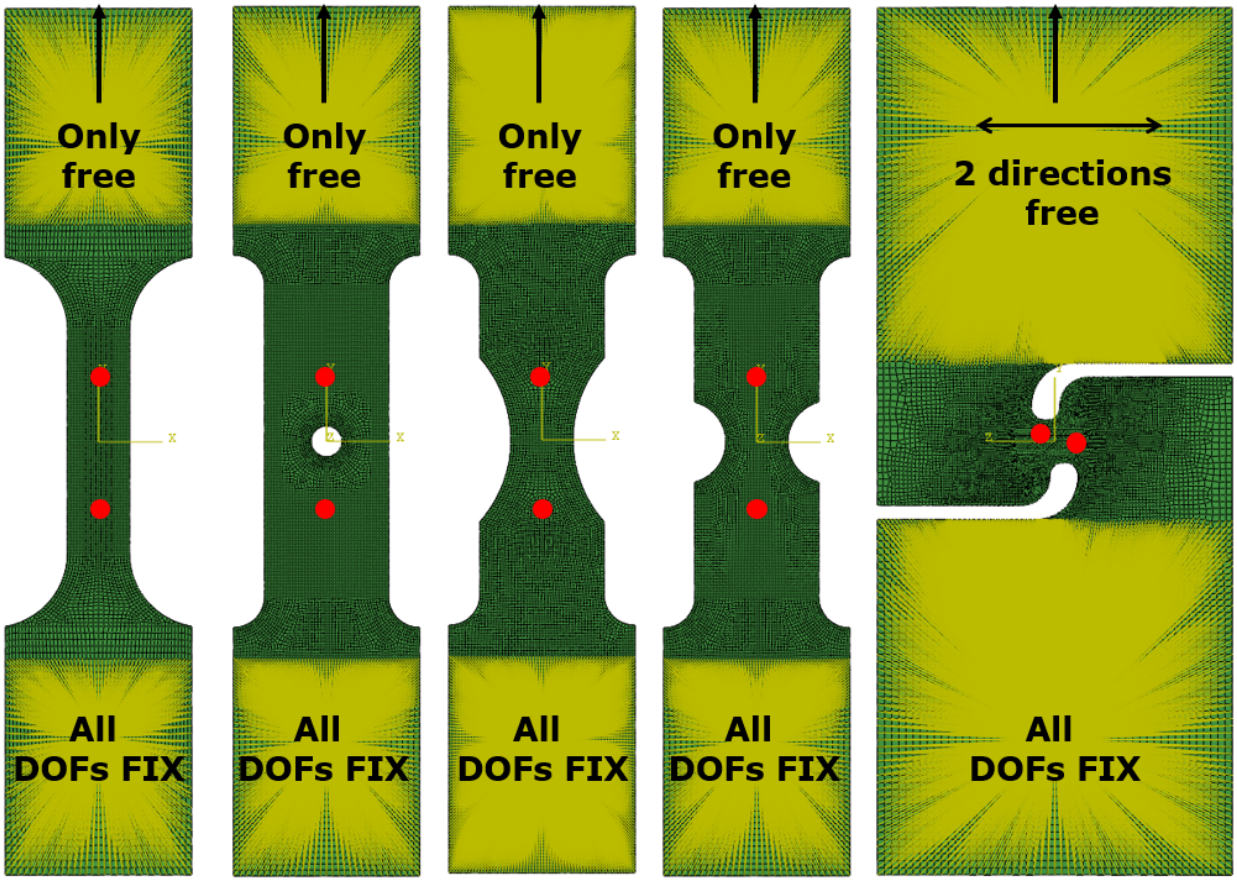

Figure 3.16: C3D8R numerical models with boundary conditions

Moreover, the displacement extraction nodes, ±10 mm from the model center, are marked with red dots in Figure 3.16, and they correspond to the experimental displacement extraction points. The reaction force data was obtained from fixed (lower) reference point. Additionally, due to significant strain localization in shear models, the element size of 0.5 mm was too coarse for these models. Hence, the element size was further reduced to 0.05 mm in shear gage section to avoid the localization influence. Consequently, the shear simulation computational time is increased due to smaller increment size. Therefore, 10 elements through thickness in combination with symmetry in the thickness direction were used to model only one half of the 2 mm SH-MD model. On the other hand, 2 and 3 mm tensile models (UT, CH, NT20, NT6) were modelled with 4 and 6 elements through thickness, respectively.

3.5 Swift-Voce hardening calibration

The calibration process used for the parameter determination is shown in Figure 2.6. The engineering stress-strain curves are calculated from force-displacement results of UT specimen for both thicknesses, shown in Figure 3.4 and 3.5. The force value is divided by the initial cross-sectional area in order to obtain the engineering stress. Furthermore, the engineering strain is calculated from the following expression:

$$\varepsilon_{eng} = \frac{l - \Delta l}{l}, \tag{3.10}$$

where l is initial point offset of 20 mm and Δl is the displacement. The engineering stress-strain curves of 2 and 3 mm thickness are shown in Figure 3.17. The 2 mm specimen exhibits higher stress values, while the 3 mm specimen is able to elongate more.

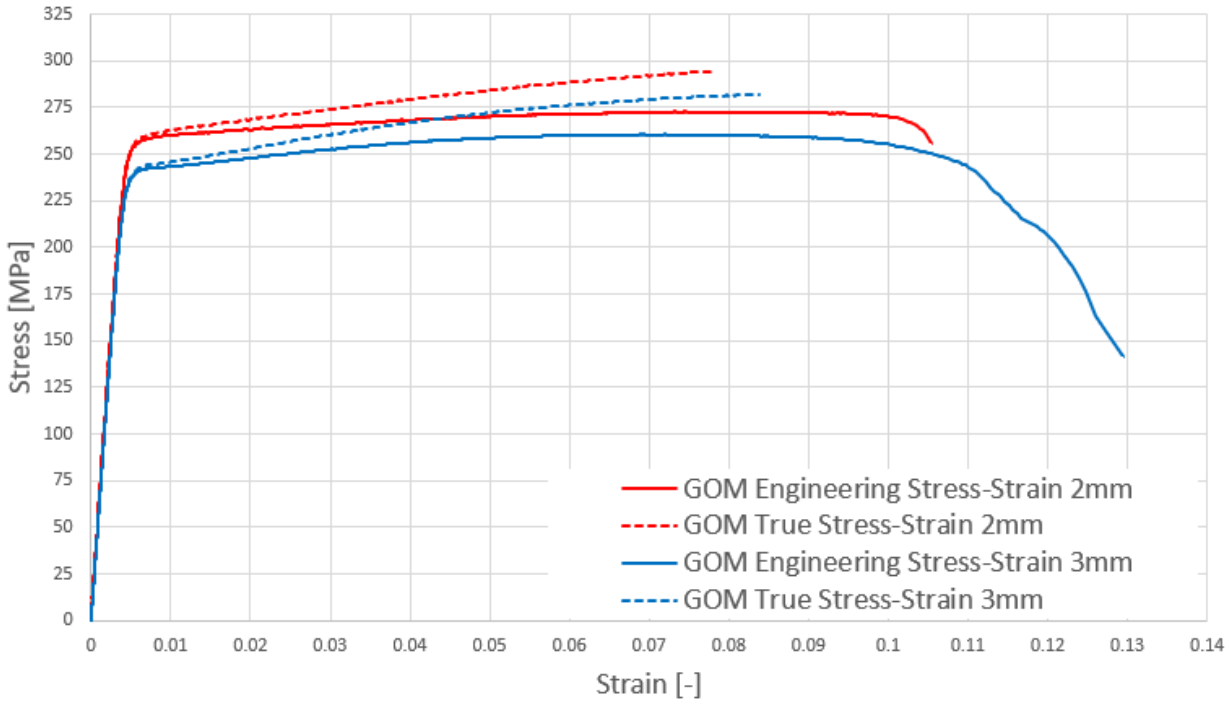

Figure 3.17: Engineering and true stress-strain curves of 2 and 3 mm thickness

However, engineering stress-strain data is not suitable for the *Abaqus* simulation input. Hence, the engineering stress-strain data is recalculated into true stress-strain data up to UTS using the equations (2.6) and it is displayed in Figure 3.17. Moreover, it is evident that the onset of necking occurs at low strains. Since the Swift and Voce hardening parameters are determined from true stress-plastic strain points, the elastic strain component needs to be subtracted from the total true strain by the equation (2.7). The resulting true stress-plastic

strain curves for both thickness are visible in Figure 3.18.

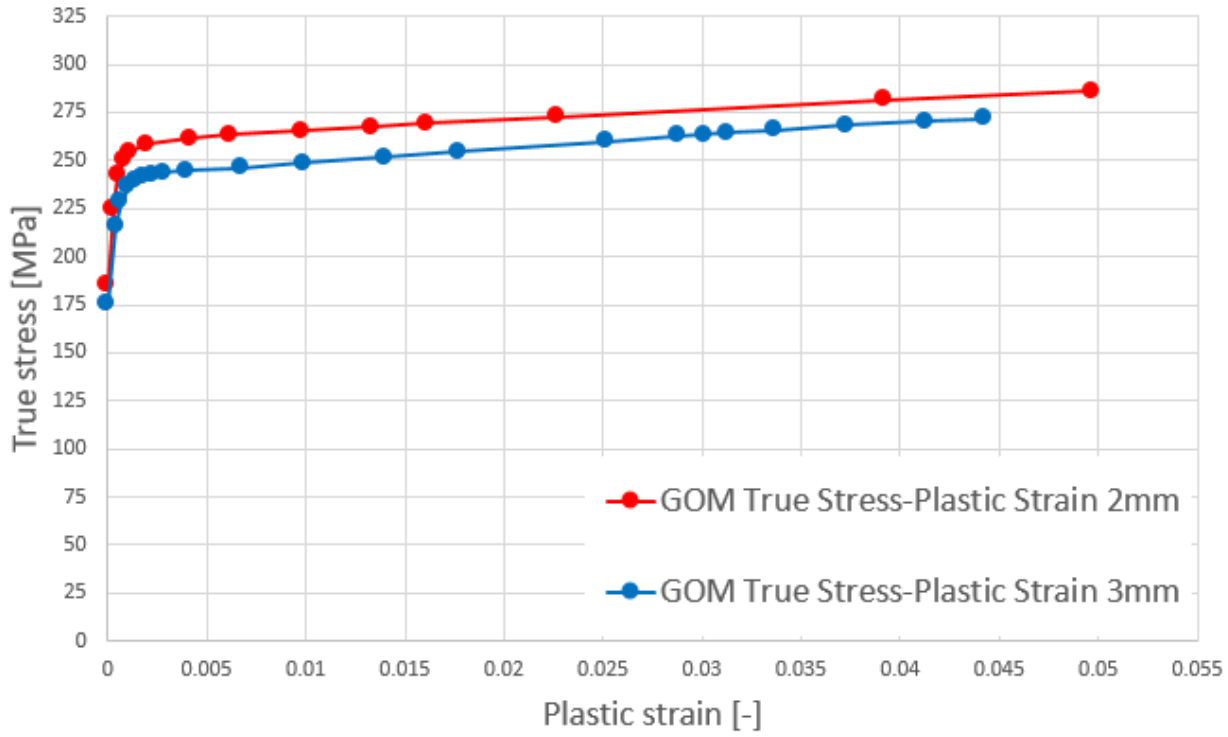

Figure 3.18: True stress-plastic strain curves of 2 and 3 mm thickness

Several points from both curves, shown in Figure 3.18, are selected and used for the hardening calibration. The Swift and Voce strain hardening parameters are obtained from a least-square fit of the selected points using the *Matlab* software. The parameters obtained from fitting the equations (2.3) and (2.4) are shown in Table 3.2.

Table 3.2: Swift and Voce hardening parameters for both thicknesses obtained by curve fitting

	2 mm	3 mm
Swift parameters		
A [MPa]	353.3	353.4
ε_0	$3.304 \cdot 10^{-6}$	$1.028 \cdot 10^{-5}$
n_{fit}	0.05124	0.06101
Voce parameters		
k_0 [MPa]	185.2	175.4
Q [MPa]	74.32	67.81
β	2640	2170

The Swift parameters for 2 mm specimen are slightly lower than 3 mm parameters, while the Voce 2 mm parameters are a bit greater than those of 3 mm specimen. Still, the parameter α, from the equation (2.5), is unknown and it is determined through inverse analyses using the simulations in *Abaqus*. The weighting factor α determines the influence of the each flow

law in the final hardening curve, and plays an important role in the post-necking range. Due to predetermined location of the necking and fracture, the NT20 specimen and its experimental results until the damage initiation are chosen to identify α. The α identification method represents a minimization problem, since the difference between the simulated and measured force-displacement response needs to be eliminated. The iterative identification loop is shown in Figure 2.6. Firstly, the initial 0.5 weighting factor α is selected to obtain the initial *Abaqus* plasticity input. Secondly, the simulation with NT20 numerical model is run and the corresponding force-displacement response is obtained and compared to experimental response. If the simulated response underestimates the real response, weighting factor should be increased, and vice versa. The simulation is run with new material input gained from the new weighting factor. As mentioned, the weighting factor has great influence on post-necking zone, i.e. high strains. On the other hand, the parameter n highly affects the stress values at lower strains. Therefore, if the force response at lower strains is mismatched, this parameter should also be included in inverse optimization. The increase of n leads to lower stress at the low strains, as well as the decrease of n leads to higher stress level at lower strains. Once the experimental and simulated force-displacement responses match, the weighting factor α and n_{opt} are determined. Hence, the final plastic material input is obtained and used in further damage model validation. The optimized n parameter and the weighting factor α are shown in Table 3.3.

Table 3.3: The weighting factor α and optimized parameter n for both thicknesses

	2 mm	3 mm
α	0.9	0.86
n_{opt}	0.07	0.08

The value of the weighting factor indicates that the Swift hardening law has the dominant role in the final hardening curve for both thicknesses. However, the use of Swift itself overestimates the force-displacement response of the real material. Each individual law for 2 and 3 mm specimen is shown in Figure 3.19 and 3.20. Since the onset of necking occurs at low strains, there is significant difference between Swift and Voce laws. It is evident that the Voce law exhibits saturation at the specific stress value. This saturated stress value is defined with the sum of the initial yield stress and coefficient Q. Furthermore, the stress values of 2 mm hardening laws are slightly greater than the 3 mm laws.

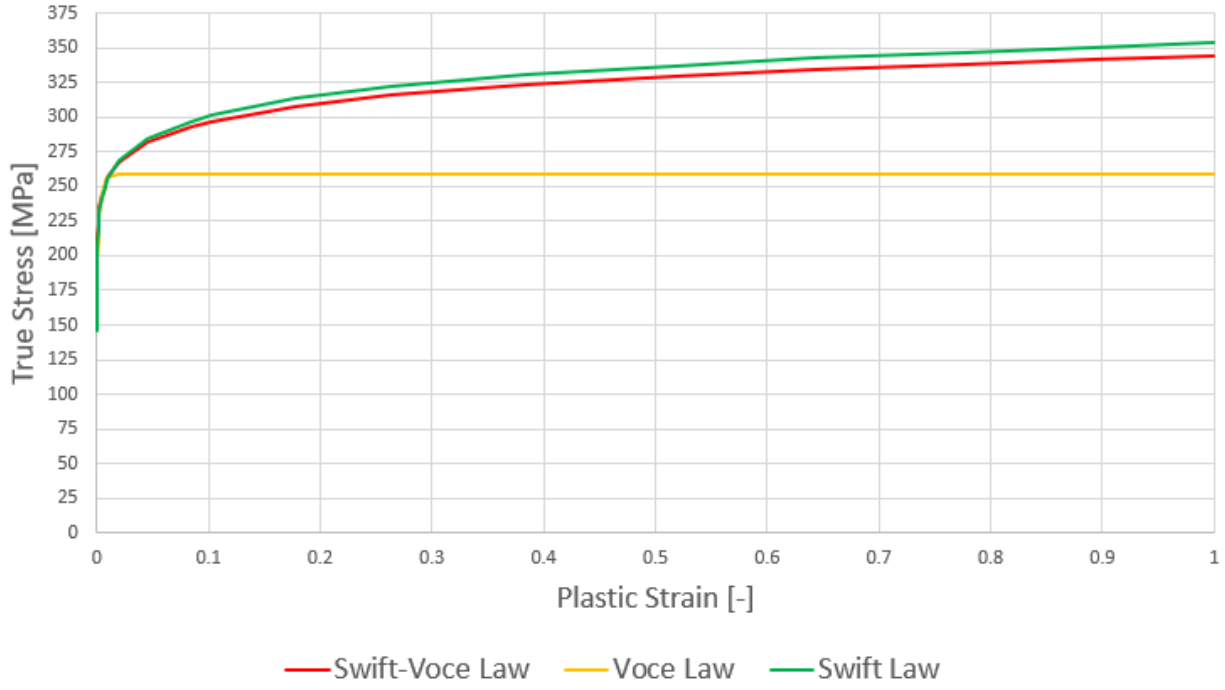

Figure 3.19: Swift, Voce and combined Swift-Voce hardening laws of 2 mm specimen

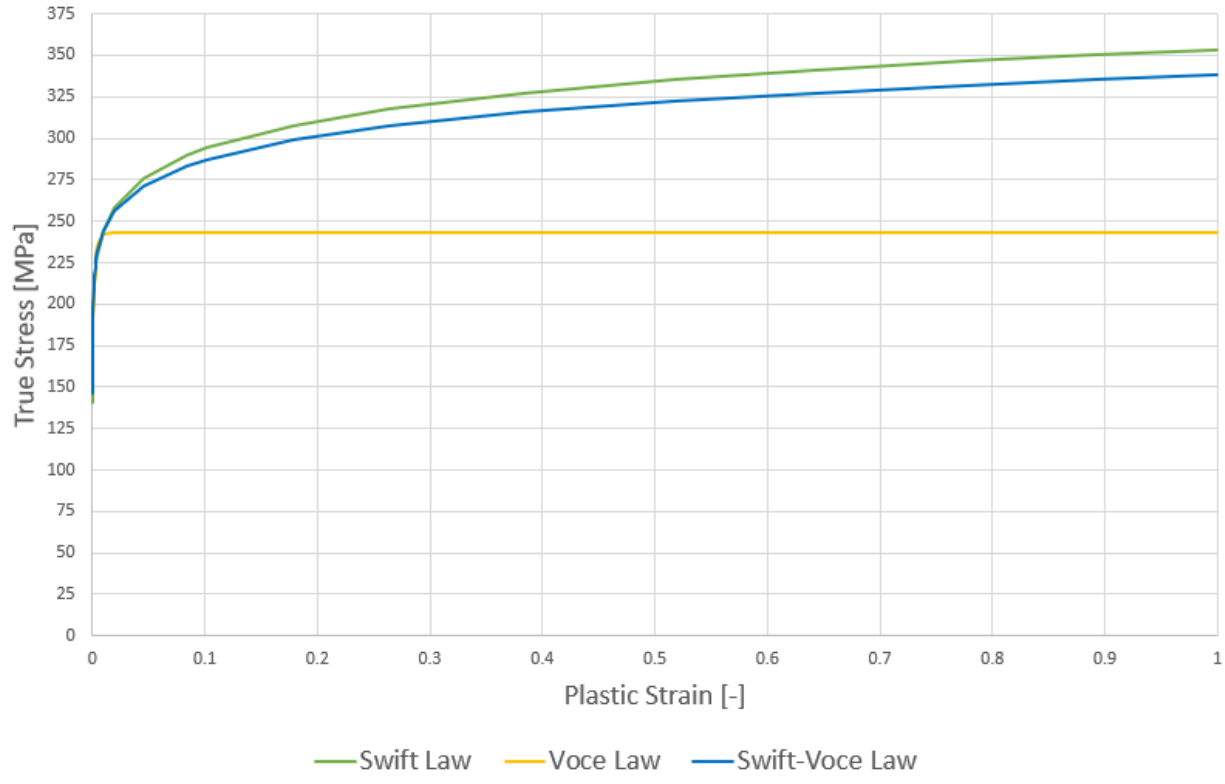

Figure 3.20: Swift, Voce and combined Swift-Voce hardening laws of 3 mm specimen

The comparison between 2 and 3 mm hardening curves is shown in Figure 3.21. Although the curves are very similar, one specific curve can not be used for both, 2 and 3 mm, material plasticity inputs.

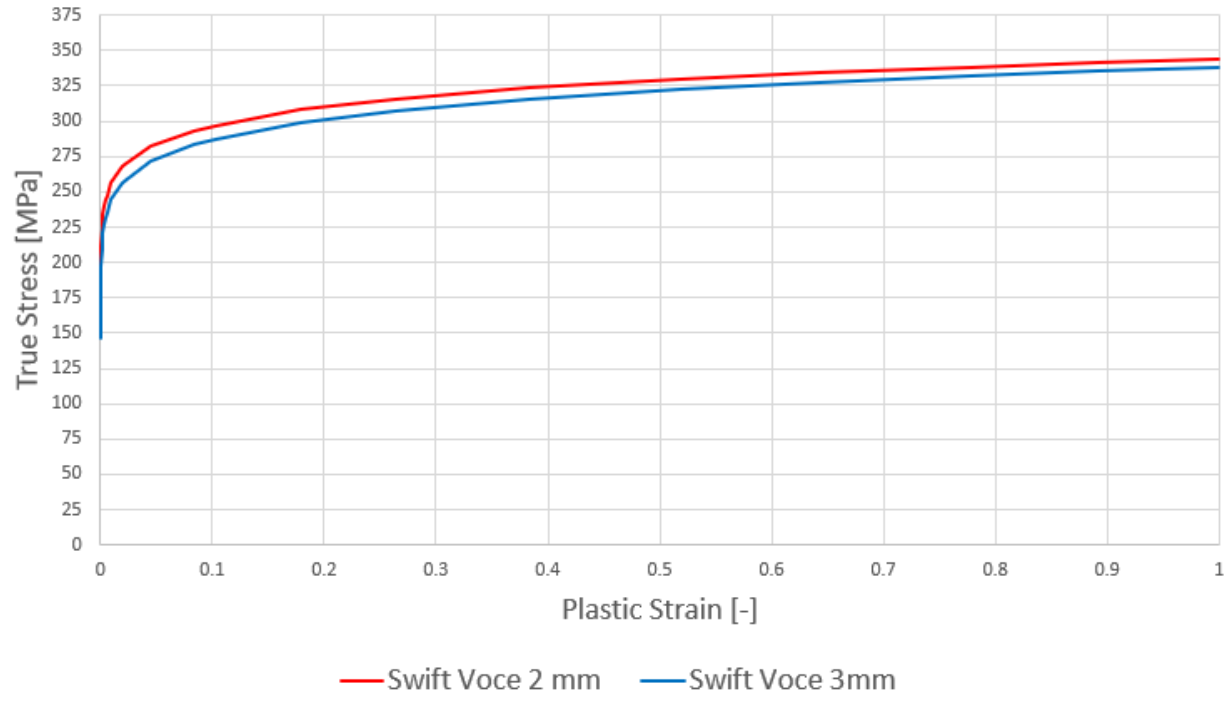

Figure 3.21: Comparison of combined Swift-Voce hardening of 2 and 3 mm specimens

3.5.1 Force-displacement response

The comparisons of the measured and simulated force-displacement response, without damage, are shown in the following figures. The proposed Swift-Voce hardening model accurately predicts the load-displacement relation for all 2 and 3 mm tensile specimens. However, the Swift-Voce flow law in combination with an isotropic hardening and the von Mises yield surface tends to underestimate the force response of the shear specimens.

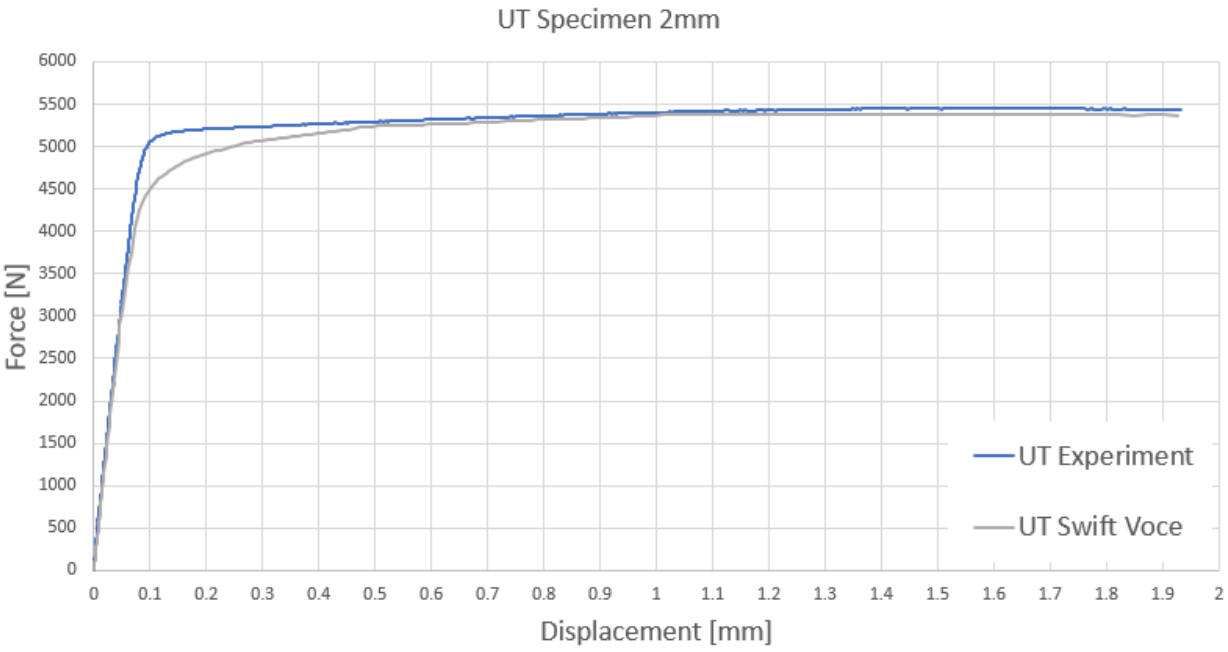

Figure 3.22: Force-displacement response of 2 mm UT specimen

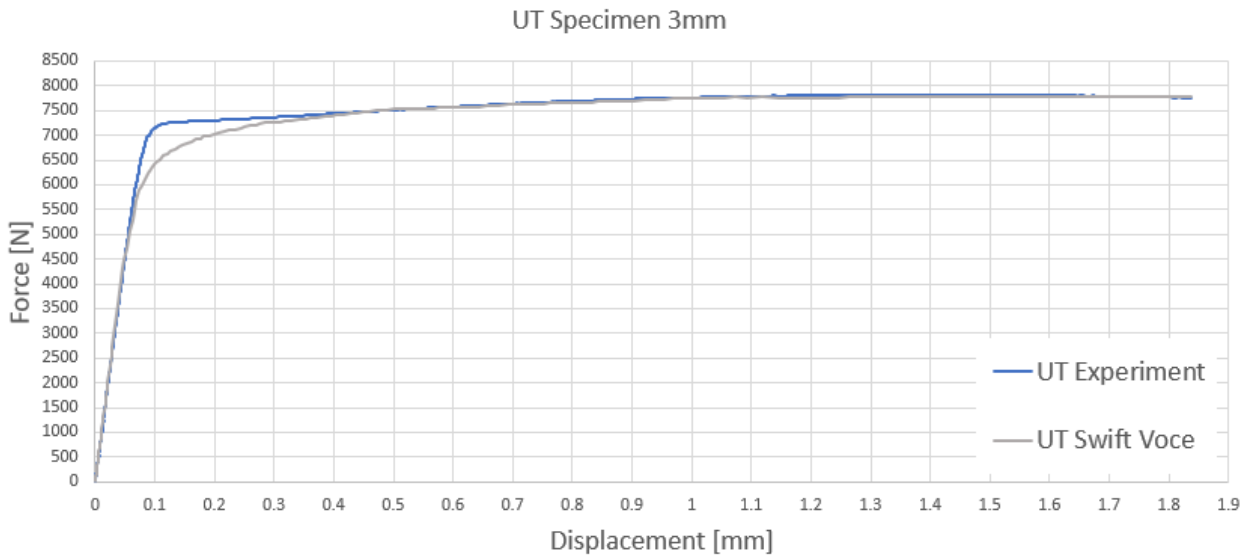

Figure 3.23: Force-displacement response of 3 mm UT specimen

The simulated uniaxial tensile specimen (UT) response (Figures 3.22 and 3.23) agrees well with the experiment, although there is slight difference in the initial yield area due to assumption of the isotropic hardening. On the other hand, the post-necking behavior is completely matched for 2 and 3 mm specimens.

The strain hardening at the onset of the inelastic deformation is underestimated for all specimen types. This is also the case with the CH specimen, shown in Figure 3.24 and Figure 3.25. Still, the magnitude of the maximum load as well as the corresponding displacement are well matched for both thicknesses.

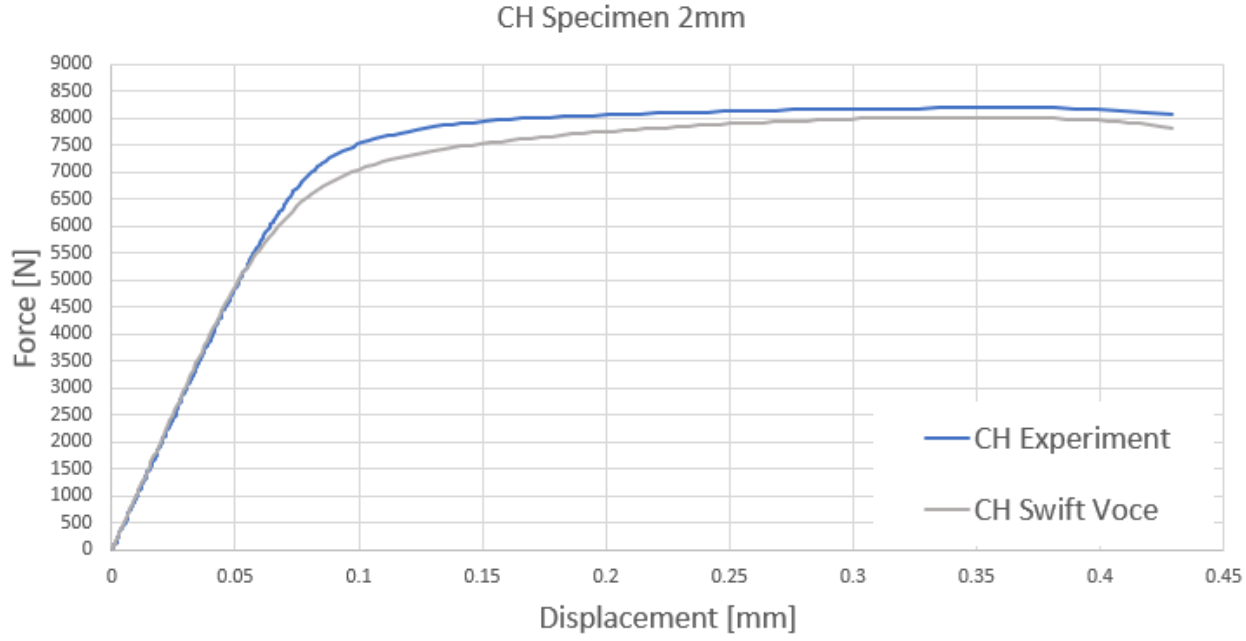

Figure 3.24: Force-displacement response of 2 mm CH specimen

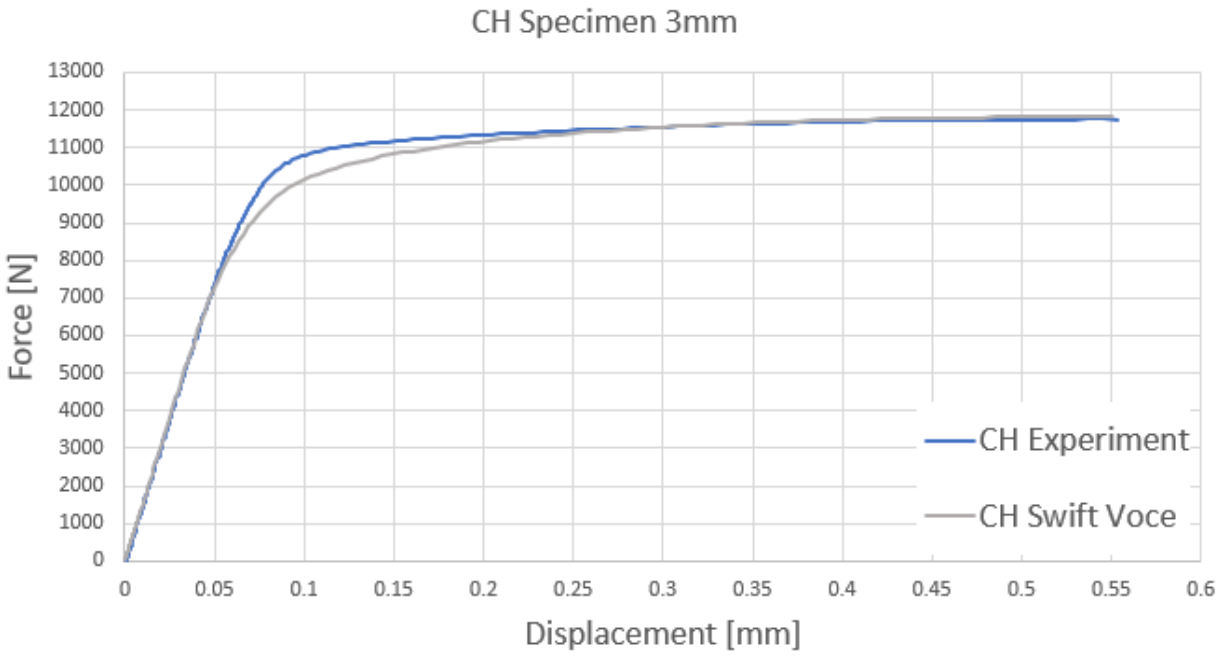

Figure 3.25: Force-displacement response of 3 mm CH specimen

Recall that the NT20 experiments have been used to calibrate the Swift-Voce hardening model. The overall prediction of the force-displacement response is satisfactory, except the initial force level at the onset of the plastic deformation (Figures 3.26 and 3.27). However, as the thickness increases, the force level is slightly overestimated.

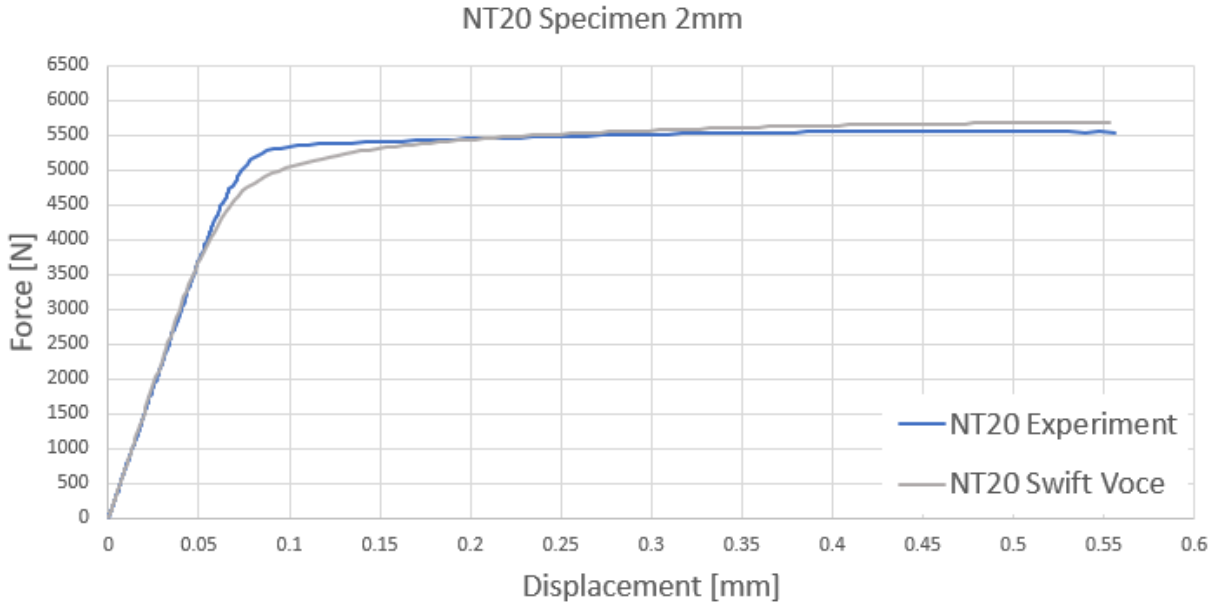

Figure 3.26: Force-displacement response of 2 mm NT20 specimen

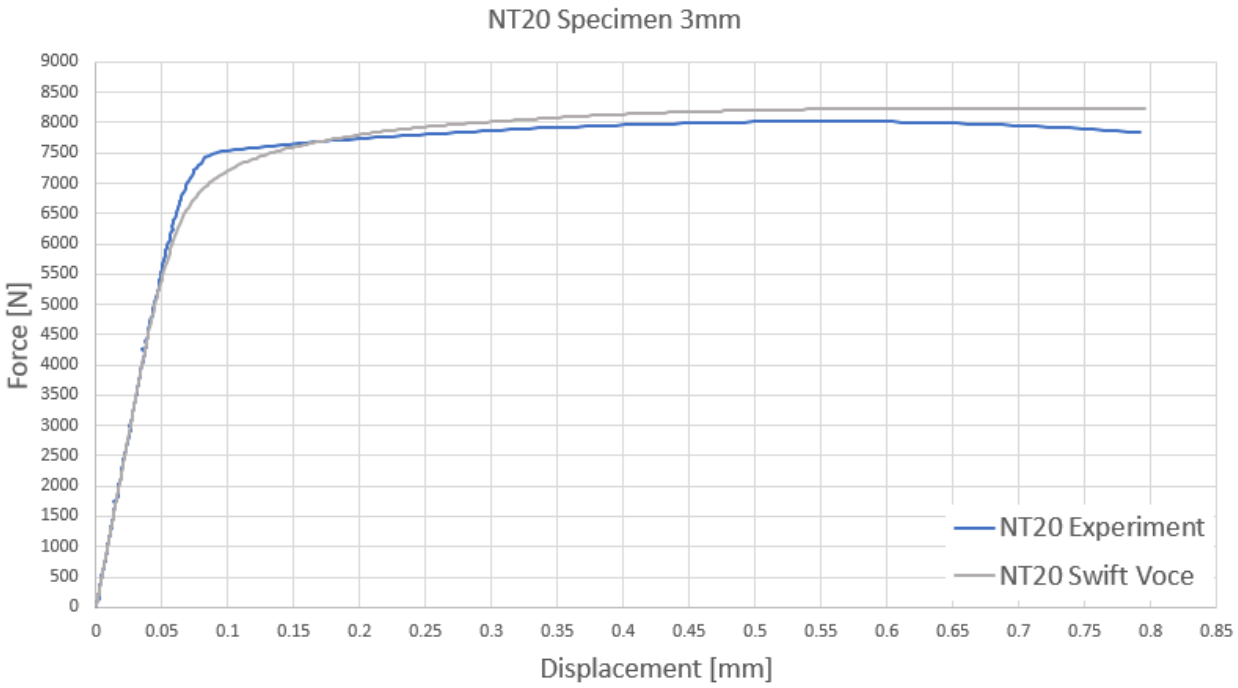

Figure 3.27: Force-displacement response of 3 mm NT20 specimen

The measured and simulated NT6 force-displacement curves of 2 and 3 mm specimens are shown in Figures 3.28 and 3.29. It is evident that the simulated response is a little bit overestimated for 2 mm specimen, while the 3 mm response exhibits even greater mismatch. The simulated force level is almost 10 % higher than the experimental 3 mm force response.

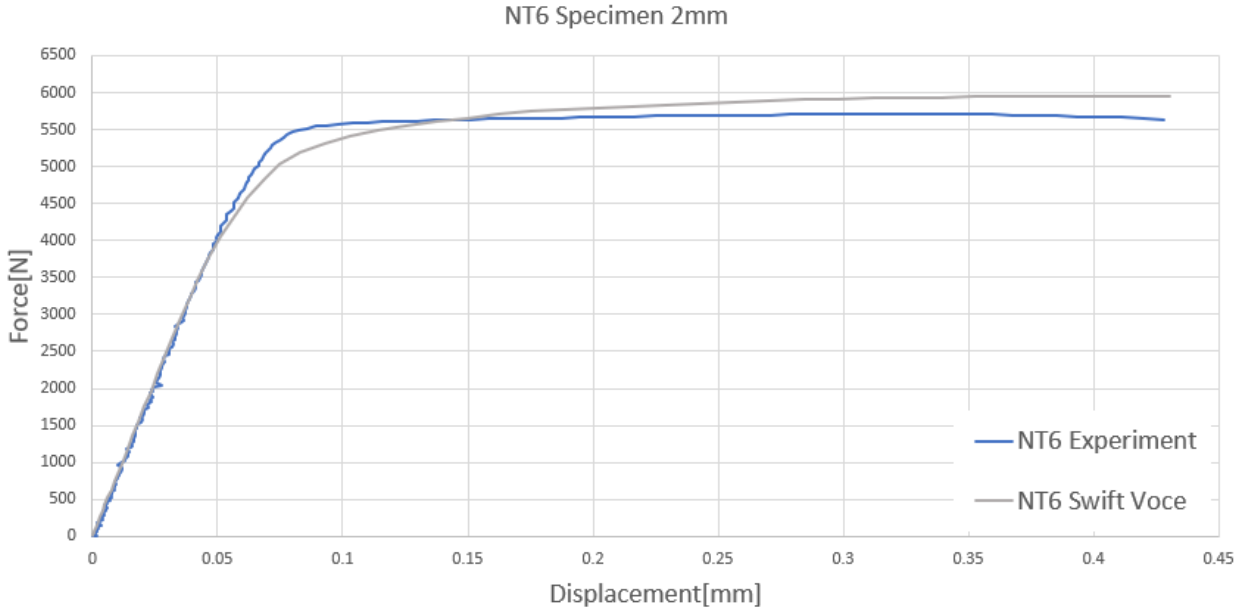

Figure 3.28: Force-displacement response of 2 mm NT6 specimen

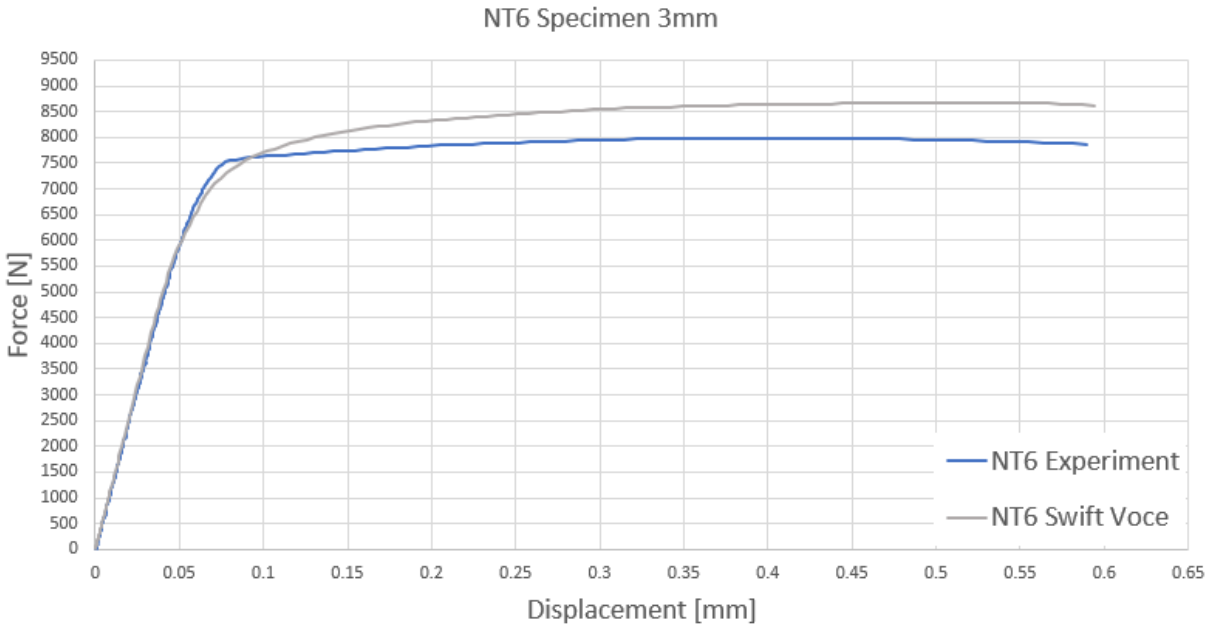

Figure 3.29: Force-displacement response of 3 mm NT6 specimen

Experimental and numerical force-displacement response up to the fracture initiation point of 2 mm shear specimen is shown in Figure 3.30. The 3 mm specimens were cut with a notch along the extrusion direction, as mentioned earlier, therefore these results are not used for hardening and damage calibration. It is evident from Figure 3.30 that the predicted force-displacement curve does not match the experimental. The response deviation during the elastic deformation is caused by the selection of points in which the displacement is extracted. The nodes, where the simulated displacement is obtained, do not lie on exactly the same coordinates as the experimental extraction points. However, the point coordinates offset is not big and the force deviation in the elastic region is negligible.

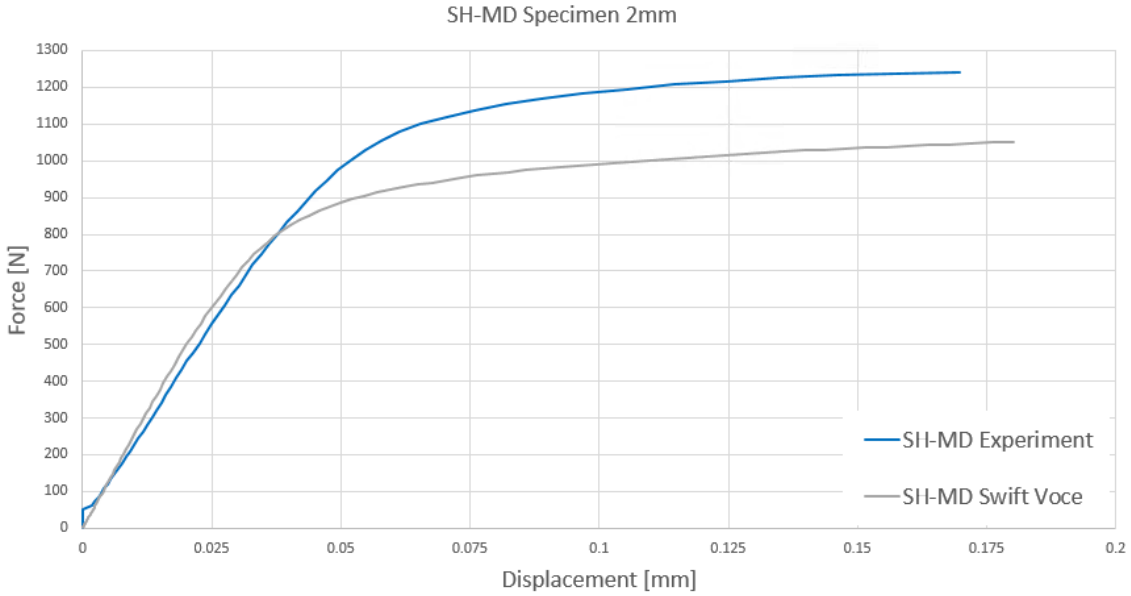

Figure 3.30: Force-displacement response for 2 mm SH-MD specimen

3.5.2 Major principal strain fields comparison

In addition to force-displacement response comparison, the major principal strain fields are compared to assess the accuracy of the Swift-Voce hardening model calibration. The distributions of the major principal strain within the NT20 specimen cross-section at various load stages are shown on the following figures.

The 2 mm NT20 simulated and measured major strain fields at the displacement of 0.15 mm are shown in Figure 3.31. The proposed Swift-Voce plasticity model provides reasonable estimates of the surface strains during the loading. Figure 3.31 b) shows that the measured strain field exhibits some strain localization due to used DIC method. However, the simulated strain values are slightly lower than the average of the experimental strain values in the observed gage section.

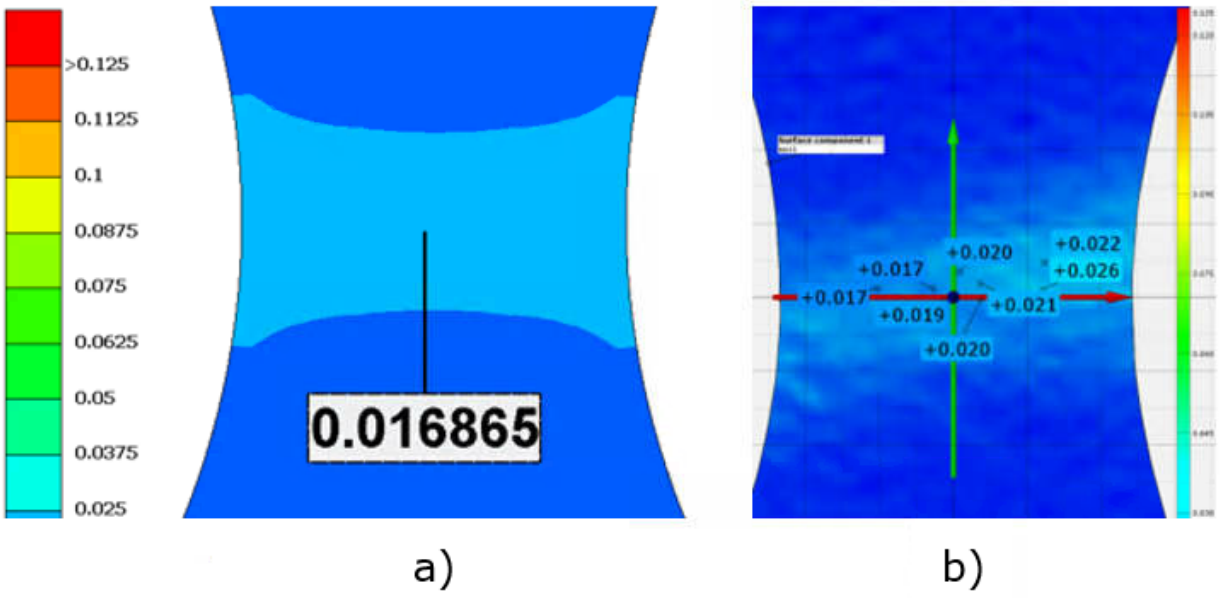

Figure 3.31: NT20 2 mm specimen major strain distribution at 0.15 mm: a) simulated b) experimental

While the specimen undergoes further loading, the strain values rise. Figure 3.32 presents the computed and experimental strain fields of NT20 2 mm specimen when the displacement of 0.3 mm is reached. As shown in the below figure, the strain distribution is still slightly underestimated. However, the difference is less than one percent, so it is concluded that the material model is accurate. Moreover, the strain contours indicate the equal further development of the strain fields.

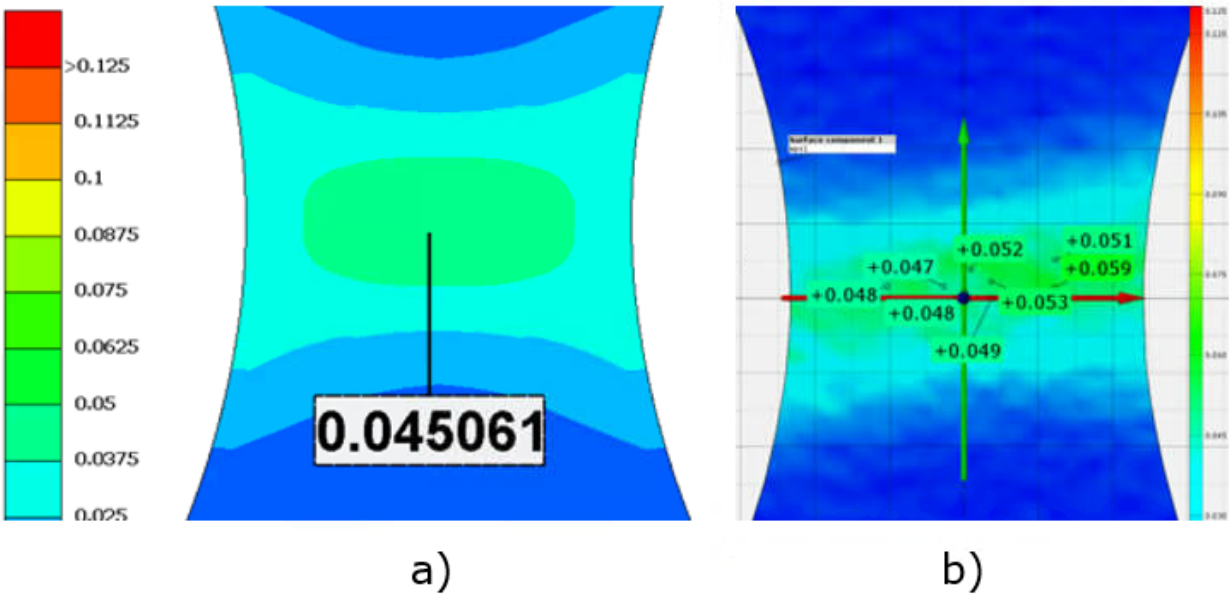

Figure 3.32: NT20 2 mm specimen major strain distribution at 0.3 mm: a) simulated b) experimental

The strain distribution at 0.45 mm displacement is shown in Figure 3.33. The computed major principal strain increasingly matches the measured values. In comparison to the strain distributions at smaller displacements, the difference is even smaller.

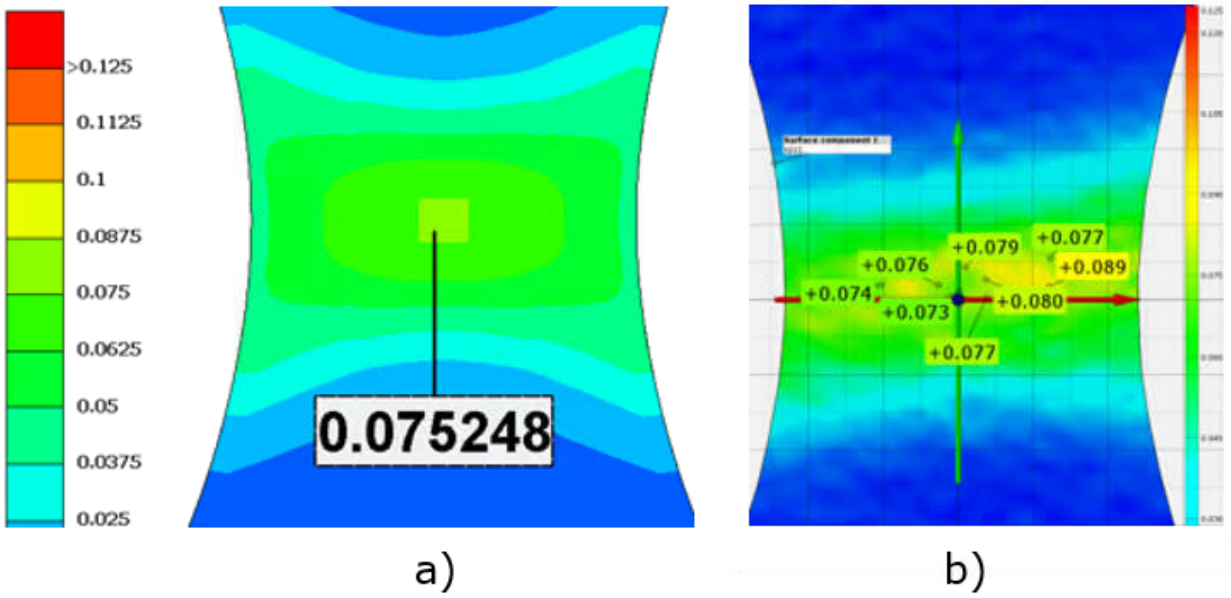

Figure 3.33: NT20 2 mm specimen major strain distribution at 0.45 mm: a) simulated b) experimental

Finally, the major principal strain fields before the onset of damage are shown in Figure 3.34. The highest values of the measured fields prevails at the center of the specimen, which corresponds to the simulated location. Furthermore, the difference between computed and real values is still negligible.

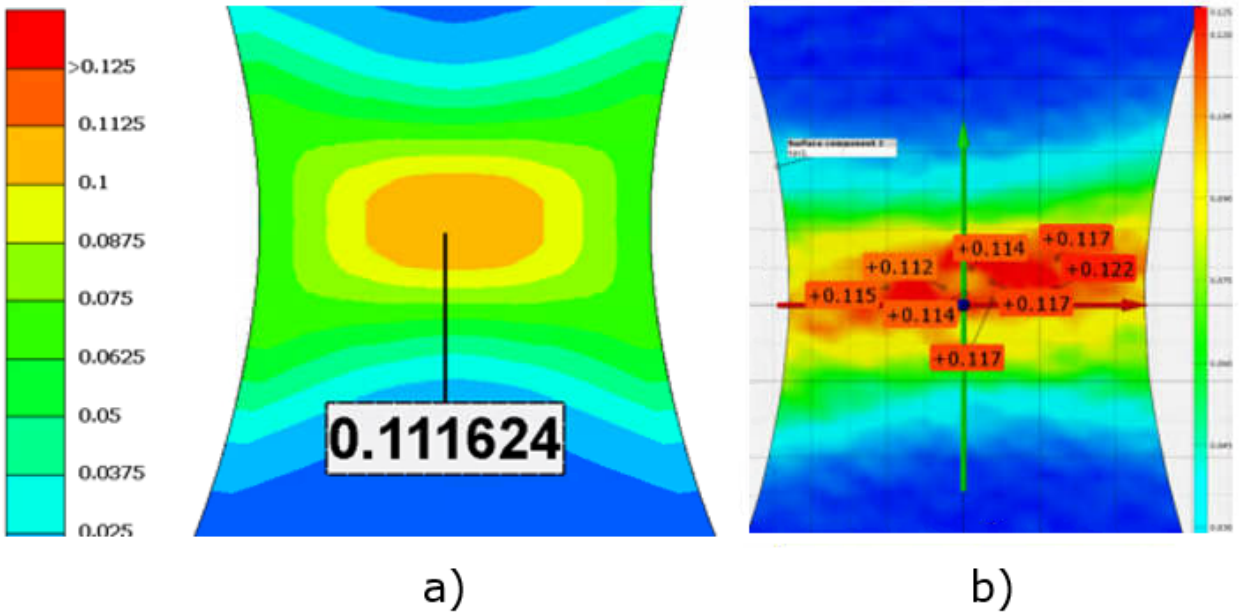

Figure 3.34: NT20 2 mm specimen major strain distribution at 0.6 mm: a) simulated b) experimental

The same comparison of major principal strain distribution is done for 3 mm thick specimens. The surface strain fields of NT20 specimen are shown in the following figures. The computed and measured major principal strain fields at the displacement of 0.206 mm are displayed in Figure 3.35. The computed strain field is quite consistent with the measured one.

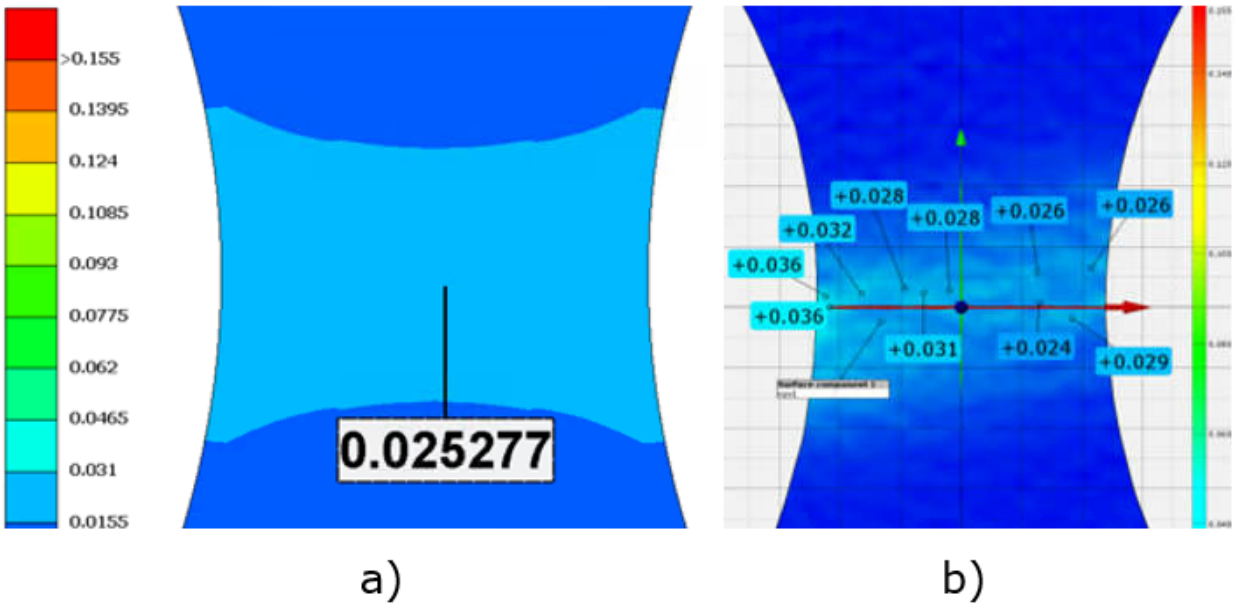

Figure 3.35: NT20 3 mm specimen major strain distribution at 0.206 mm: a) simulated b) experimental

Figure 3.36 displays strain distribution of 3 mm NT20 specimen for displacement of 0.401 mm. The major principal value of 6% matches the calculated average within the gage section. Also, the matching material behavior is evident from similar contour plots.

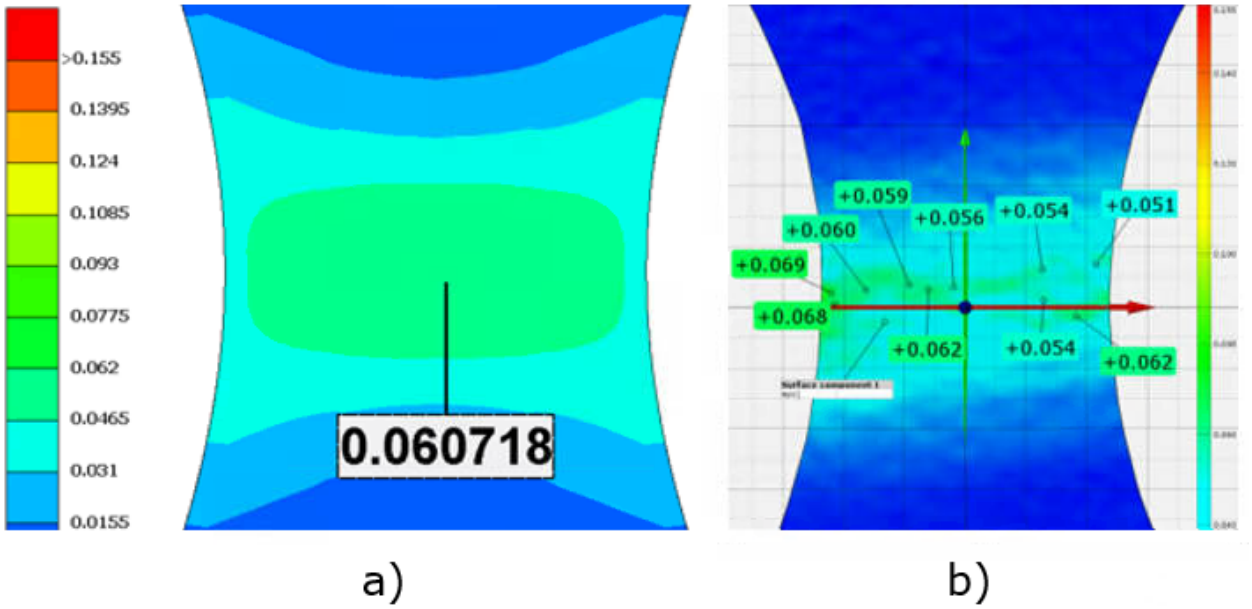

Figure 3.36: NT20 3 mm specimen major strain distribution at 0.401 mm: a) simulated b) experimental

The strain distribution at 0.6 mm is displayed in Figure 3.37. This figure shows that the used Swift-Voce model is able to correctly predict surface strain distribution through the entire post-necking area. The computed values, as well as the contour plots, are equal to the measured.

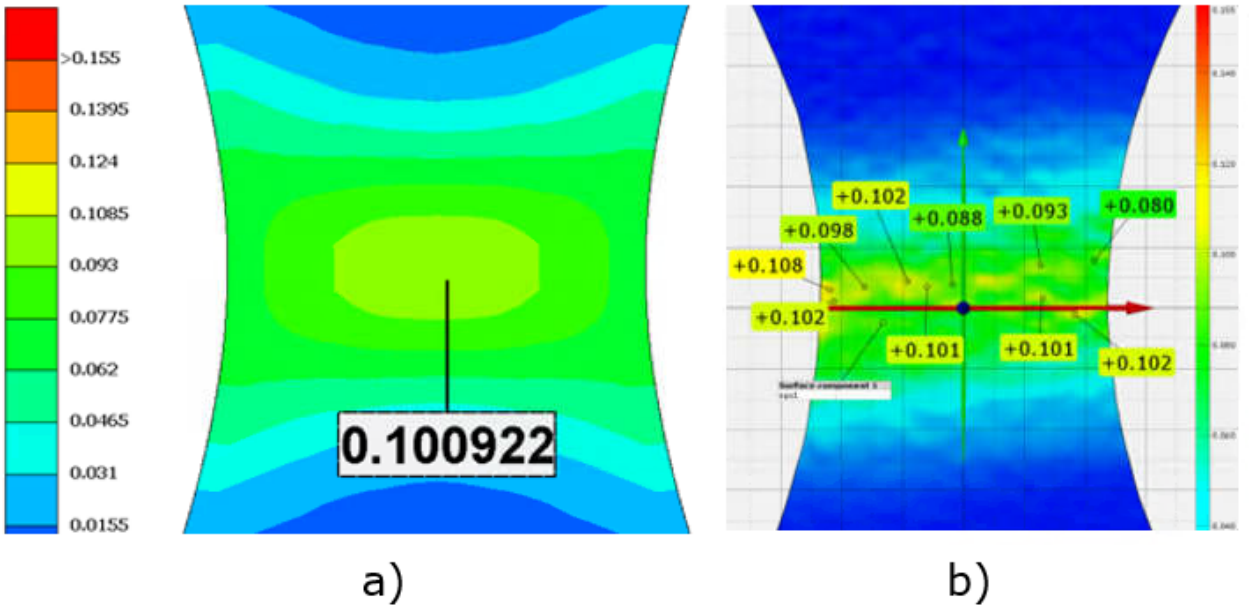

Figure 3.37: NT20 3 mm specimen major strain distribution at 0.6 mm: a) simulated b) experimental

3.6 Discussion

The force-displacement and strain fields comparison, presented in sections 3.5.1 and 3.5.2 respectively, leads to the conclusion that the proposed Swift-Voce hardening model adequately describes material behavior before the fracture onset. Excellent matching is achieved for the UT and CH specimens for both thicknesses (Figures 3.22-3.25). Triaxiality of these specimens varies from 0.33 to 0.4, therefore the stress state is very close to uniaxial stress state. Furthermore, the major principal strain field comparison for NT20 specimen shows that the computed surface strain matches the measured, from the elastic state until the onset of damage. Due to the large number of specimens as well as two thicknesses the comparisons of other strain fields are not shown, although an excellent matching is achieved for every specimen. However, the force-displacement responses of NT6 and SH-MD specimen deviate from the measured response (Figures 3.28, 3.29 and 3.30). As it is mentioned in the section 3.1, the NT6 specimen covers the triaxiality from initial 0.5 to 0.57, since the triaxiality rises as the material undergoes the plastic deformation. The stress state under this triaxiality almost corresponds to the biaxial stress state (triaxiality of 0.67), which means that the stress components in other directions have increased influence (Figure 3.38). The principal stress component in the perpendicular direction is almost one half of the major principal stress value.

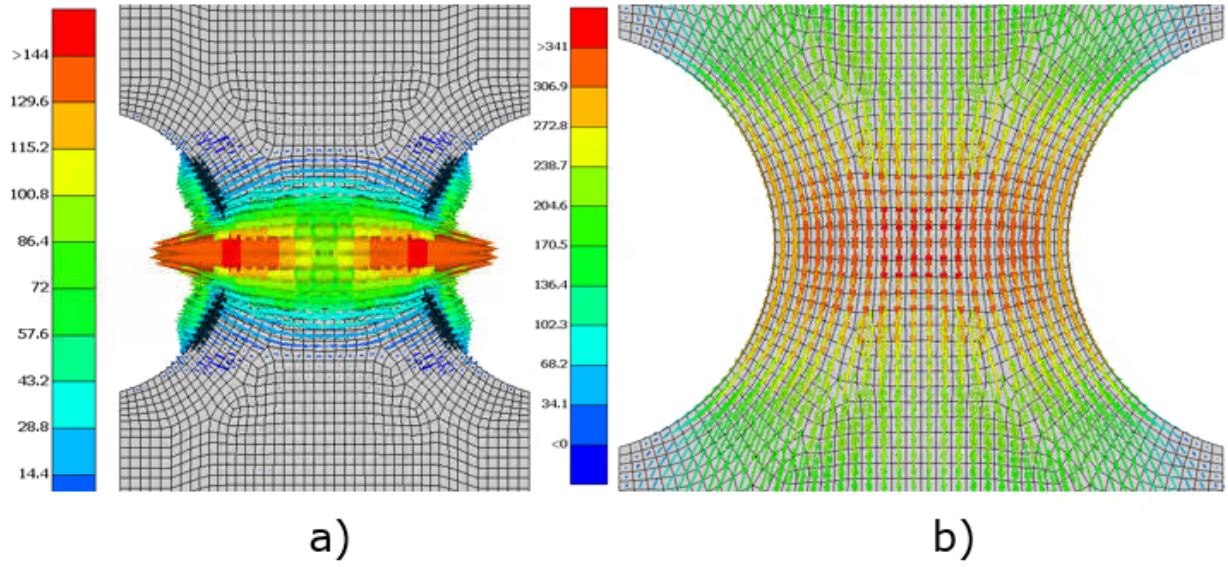

Figure 3.38: Principal stress components of NT6 3 mm specimen before the fracture initiation: a) perpendicular to extrusion direction, b) extrusion direction

The used Swift-Voce flow law assumes the isotropic hardening in combination with the von Mises yield surface. As it is described in the section 2.2, the isotropic hardening

presumes equal expansion in all directions, i.e. uniform deformation in all directions. However, this is not the case in the real extruded material, where anisotropy can cause significant deviations from the behavior predicted by the von Mises yield criterion. Anisotropy in extruded materials is caused by the formation of crystalline fibers in the direction of the extrusion, along which mechanical properties can be significantly higher compared to other directions [32]. The NT6 and SH-MD specimens exhibit high stress values in non-extrusion directions, hence the predicted response deviates from the experimental. The anisotropy due to preferred orientation is modeled well by the use of Hill's yield criterion [32]. Moreover, the Barlat Yld 2000-3D yield function is developed to describe the anisotropic behavior of sheet metal, especially aluminium alloy sheets [33]. The use of this yield functions should give better matching for NT6 and SH-MD specimen. The deviation of the simulated hardening behavior from the experimental leads to inaccuracies in damage initiation and evolution definition.

4 Ductile damage model validation

The used *Abaqus* ductile damage model is described in section 2.3.1. As mentioned, *Abaqus* uses phenomenological damage model, which describes damage as function of equivalent plastic strain $\bar{\varepsilon}_{\mathrm{D}}^{pl}$, stress triaxiality η and plastic strain rates $\dot{\bar{\varepsilon}}_{\mathrm{D}}^{pl}$. Since all the measurements and simulations are conducted with the same loading rate, the validated ductile damage model is not plastic strain rate dependent. Hence, the equivalent plastic strain at the onset of fracture is only stress triaxiality dependent. Furthermore, the main goal of ductile fracture experiments is to define the loading path to fracture, i.e. the evolution of the equivalent plastic strain as a function of the stress triaxiality. A combined experimental-numerical approach is therefore required. Plastic strain at the onset of fracture is determined from the experimental results. However, it is impossible to determine the exact fracture initiation point, as well as the exact initiation moment. Therefore, the fracture initiation displacement in this study is regarded as the point where the load is reduced sharply in the experiment. In addition, the displacement to fracture initiation determines the plastic strain at the onset of fracture. It is the highest plastic strain on the surface at that moment (Figure 4.1).

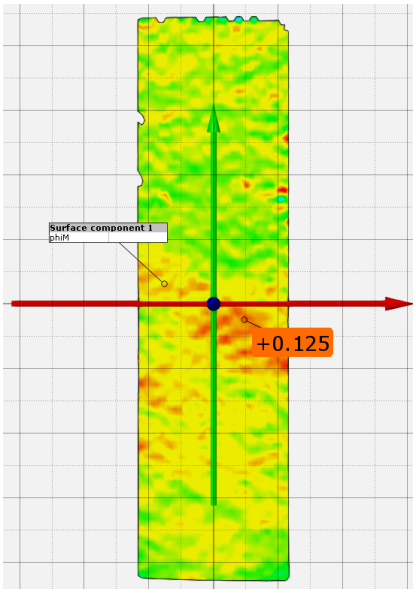

Figure 4.1: Plastic strain at the onset of fracture of 2 mm UT specimen

After the fracture strain is determined, the strain path to fracture is obtained using the numerical simulations without any implemented damage model. The equivalent plastic strain and stress triaxiality are extracted at the integration point of the element with the highest equivalent plastic strain. For tensile specimens (UT, NT20, NT6) it is the point at the very center of the specimen. However, for the CH specimen this point corresponds to a point on the specimen mid-plane at a distance of about 0.5 mm from the central hole boundary, because of the most pronounced thickness reduction at a small distance away from the hole boundary. In the SH-MD specimens, this point is positioned in the zone of the greatest strain localization. The extraction points are shown in Figure 4.2.

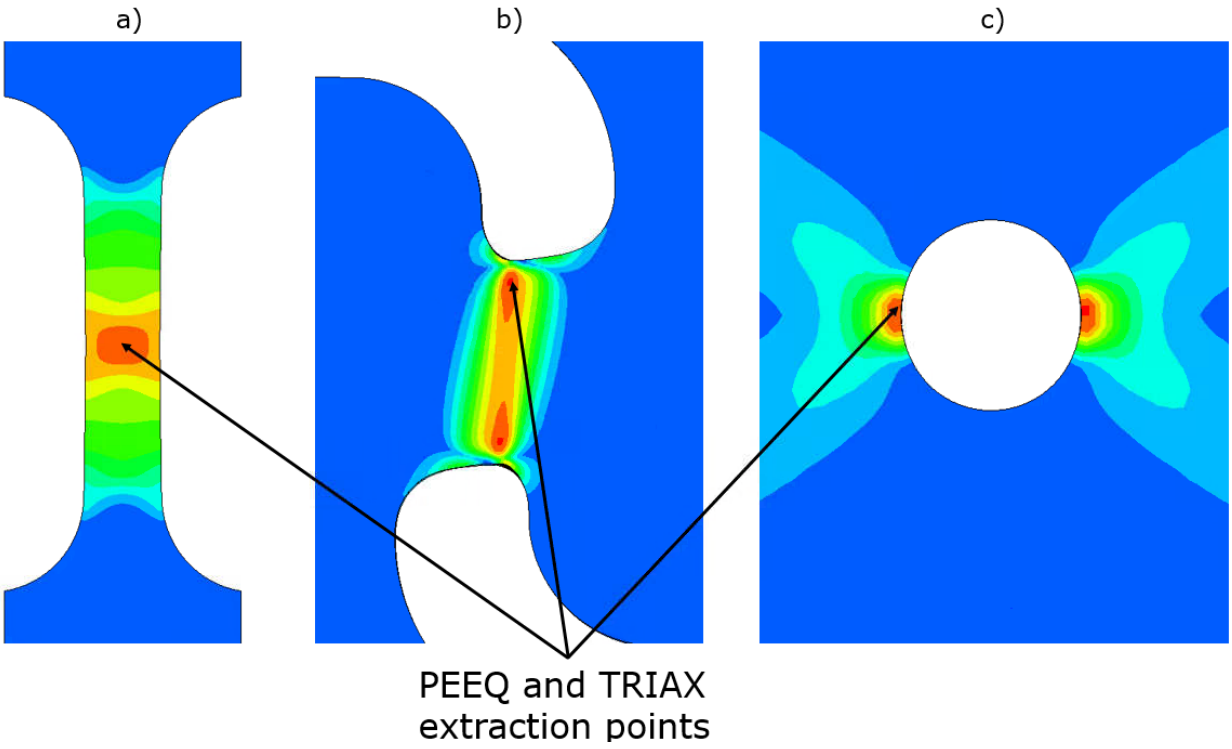

Figure 4.2: Plastic strain and triaxiality extraction points for: a) UT specimen, b) SH-MD specimen, c) CH specimen

Experimental plastic strain at the onset of damage is correlated to equivalent plastic strain in numerical simulation. Since the experimental and numerical strain fields coincide (section 3.5.2), the numerical plastic strain at the onset of fracture is equal to the experimental. Therefore, the stress triaxiality from the step in which the equivalent plastic strain is equal to the experimental fracture strain is defined as the stress triaxiality at the onset of damage. The obtained experimental fracture strain and corresponding numerical triaxiality of 2 and 3 mm specimens are displayed in Table 4.1.

However, due to the small number of frames taken for shear specimens, the plastic strain at the onset of damage for SH-MD specimen could not be obtained from

experimental results. Hence, the fracture strain for shear specimens is determined by linear extrapolation from tensile triaxiality to zero triaxiality according to literature [34]. The extrapolated shear fracture strain is further slightly increased to match the experimental force-displacement response. Moreover, due to similar strains and triaxialities of 2 and 3 mm specimens (Table 4.1), the 2 mm shear fracture strain is also used for 3 mm specimens (3 mm specimens were cut with notch in extrusion direction).

Table 4.1: The equivalent plastic strain and stress triaxiality at the onset of damage

	2 mm		3 mm	
	Plastic strain	Triaxiality	Plastic Strain	Triaxiality
SH-MD	0.17	-0.005	0.17	-0.005
UT	0.122302	0.352291	0.1231515	0.357277
NT20	0.114481	0.45371	0.1183637	0.466185
NT6	0.10368	0.535987	0.1122224	0.550935

The fracture points from Table 4.1 form the ductile fracture limit curves, which are displayed in Figure 4.3. These curves define the heart of the damage model, the denominator from the equations (2.9) and (2.10). It is obvious from Figure 4.3 that the relationship between the points is linear. Furthermore, the fracture strains of 3 mm specimens are slightly higher than of 2 mm specimens. Due to greater thickness, the triaxiality of 3 mm specimens also has greater values, as the out-of-plane stress component is bigger.

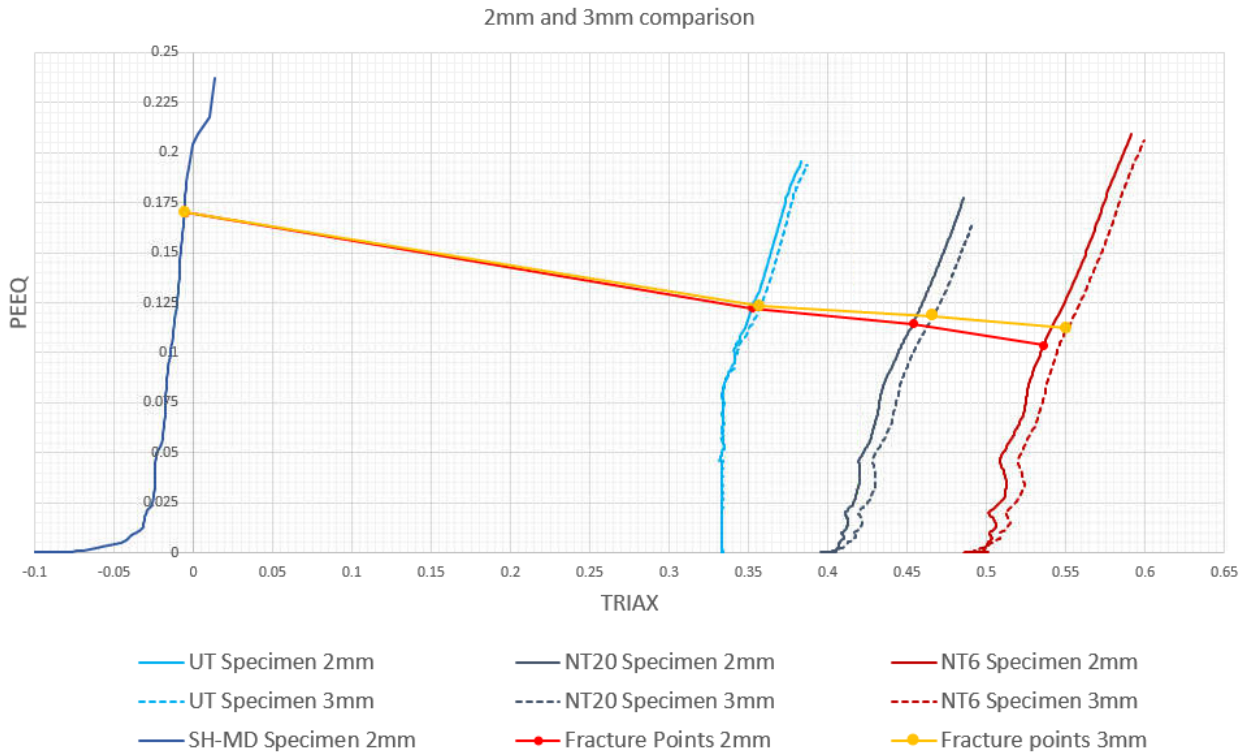

Figure 4.3: Strain paths of 2 and 3 mm specimens

The stress triaxiality fluctuations are also obvious from strain paths in Figure 4.3. The UT specimen triaxiality is constantly 0.33 until the necking initiation. Due to the notch influence, the stress triaxiality of NT20 and NT6 specimen increases as the plastic deformation initiates.

As it can be seen in Table 4.1 and Figure 4.3, the CH specimen is not used for the definition of the ductile fracture limit curves. Since the fracture of this specimen is usually initiated in the mid-plane edge of the hole, there are great uncertainties in the definition of fracture strain using a DIC method. However, this specimen is used for calibration of damage evolution displacement parameter, as it undergoes the highest plastic deformation from damage initiation to complete fracture. As shown in the equation (2.19), damage evolution is mesh sensitive and this sensitivity is described by the characteristic element length L. The characteristic element length in used numerical models is about 0.55 mm for both thicknesses. In addition, the 2 mm CH specimen exhibits plastic deformation of 15% from onset of fracture to complete failure, while the 3 mm CH specimen exhibits plastic deformation of approximately 36%. Finally, the damage evolution displacement parameters for both thicknesses are shown in Table 4.2.

Table 4.2: Damage evolution displacement of 2 and 3 mm specimens

	2 mm	3 mm
Damage evolution displacement [mm]	0.08	0.2

The ductile initiation criterion distribution of every specimen (UT shown in Figure 4.4 a)) matches the distribution of equivalent plastic strain (UT shown in Figure 4.4 b)). It is obvious that the damage concentration occurs at an angle of 45° to the loading direction, which leads to the conclusion that the fracture occurs due to the tangential stresses. Moreover, the increase of stress triaxiality is shown in Figure 4.4 c). The maximum stress triaxiality is reached at the place of the highest concentration of plastic deformation.

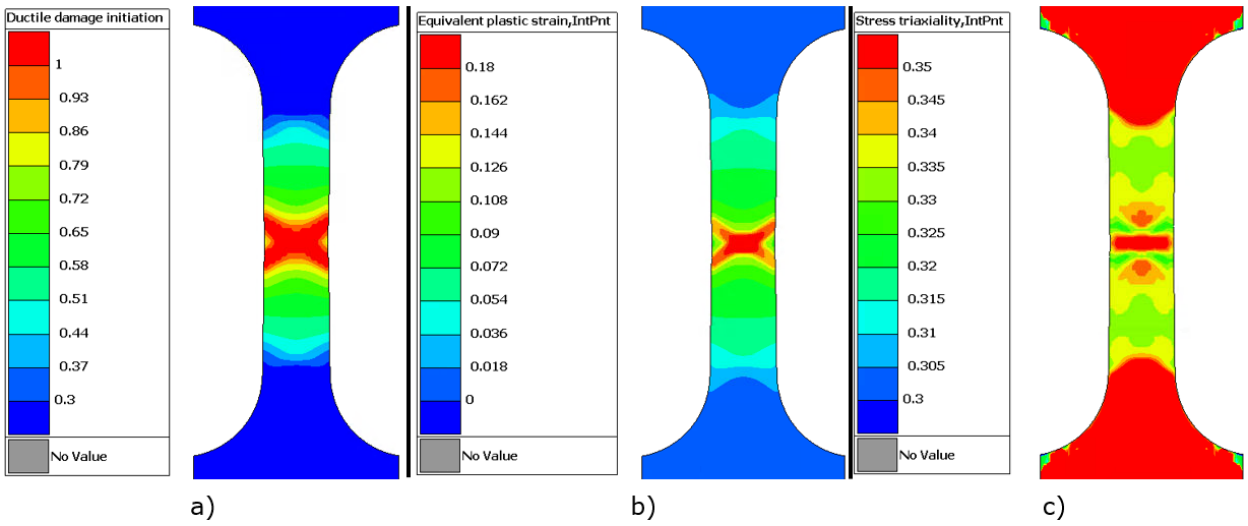

Figure 4.4: Ductile damage parameters of UT specimen: a) Ductile initiation criterion, b) Equivalent plastic strain, c) Stress triaxiality

4.1 Damaged force-displacement response

The force-displacement responses of the specimens with implemented damage model are shown in the following figures. An accurate Swift-Voce hardening model is key to good damage prediction, since the damage parameters depend on the development of plastic deformation. Simulated damage results are shown up to point of the first element deletion. The force-displacement results of UT specimen are displayed in Figures 4.5 and 4.6.

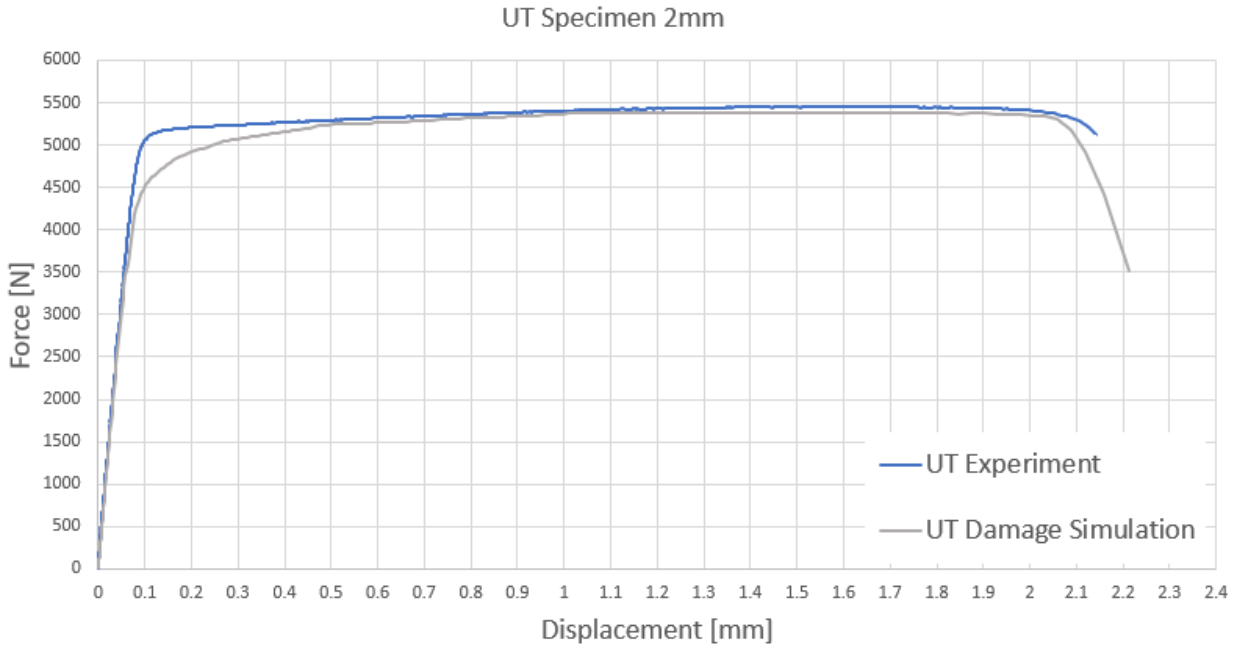

Figure 4.5: Damaged force-displacement response of 2 mm UT specimen

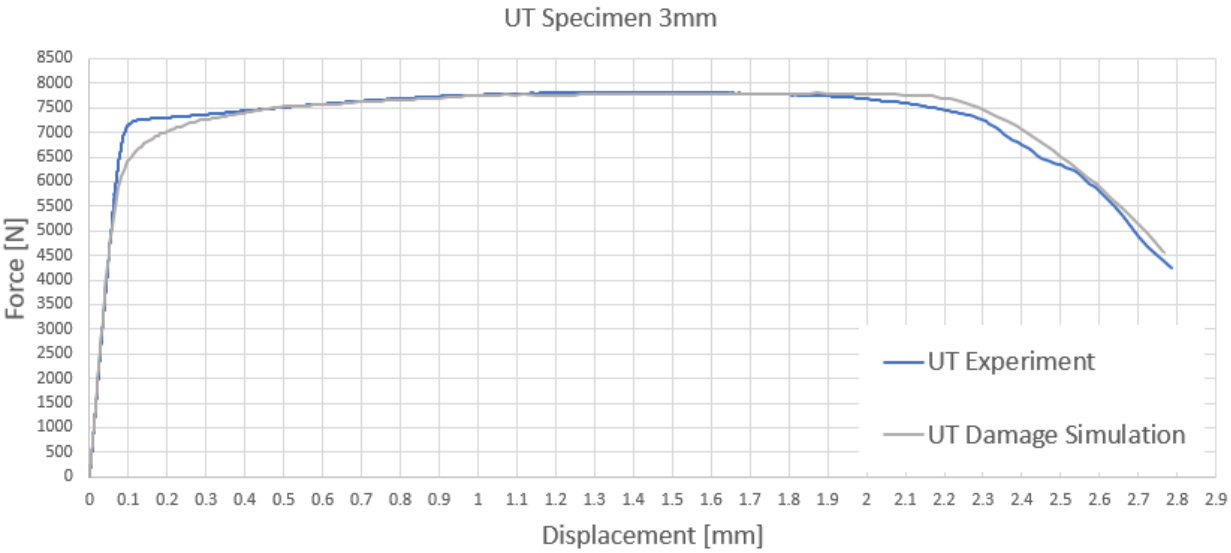

Figure 4.6: Damaged force-displacement response of 3 mm UT specimen

Due to the excellent hardening matching, the damage initiation and evolution for UT specimen is perfectly predicted. Measured damage initiation displacement, in which the experimental force suddenly drops, is completely matched by simulated model. Moreover, 3 mm damage evolution is excellently described by the proposed model.

Furthermore, the CH specimen experimental and simulated comparison are shown in Figures 4.7 and 4.8.

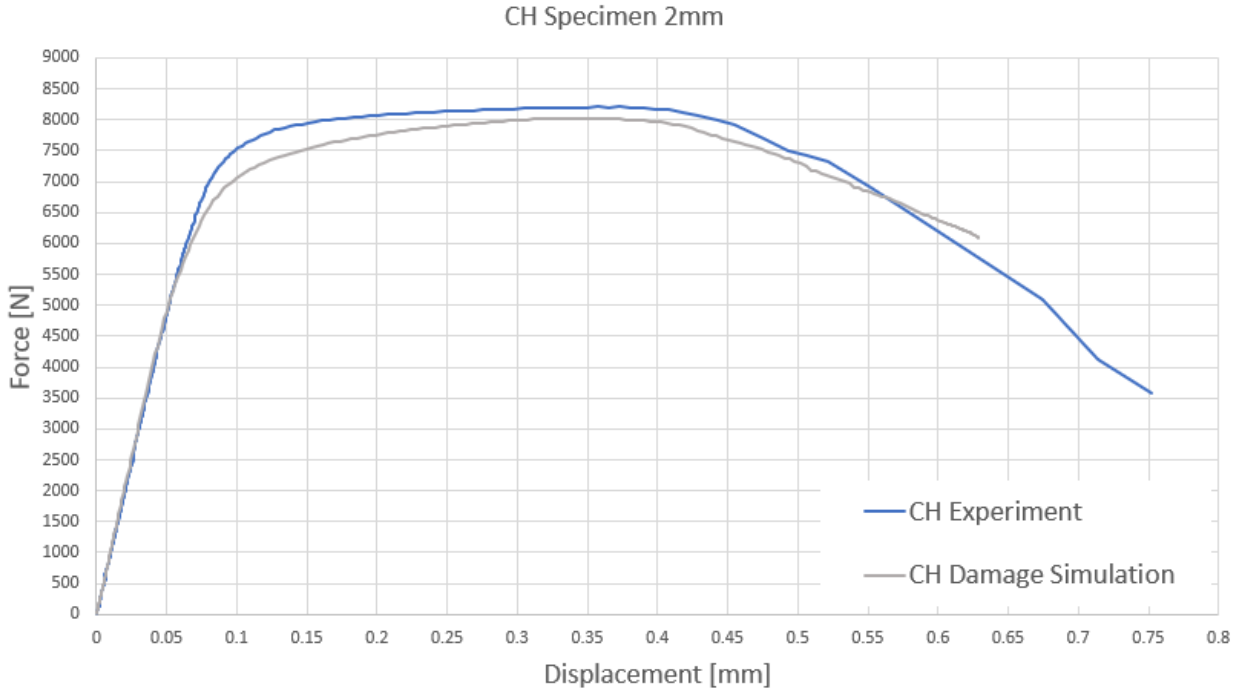

Figure 4.7: Damaged force-displacement response of 2 mm CH specimen

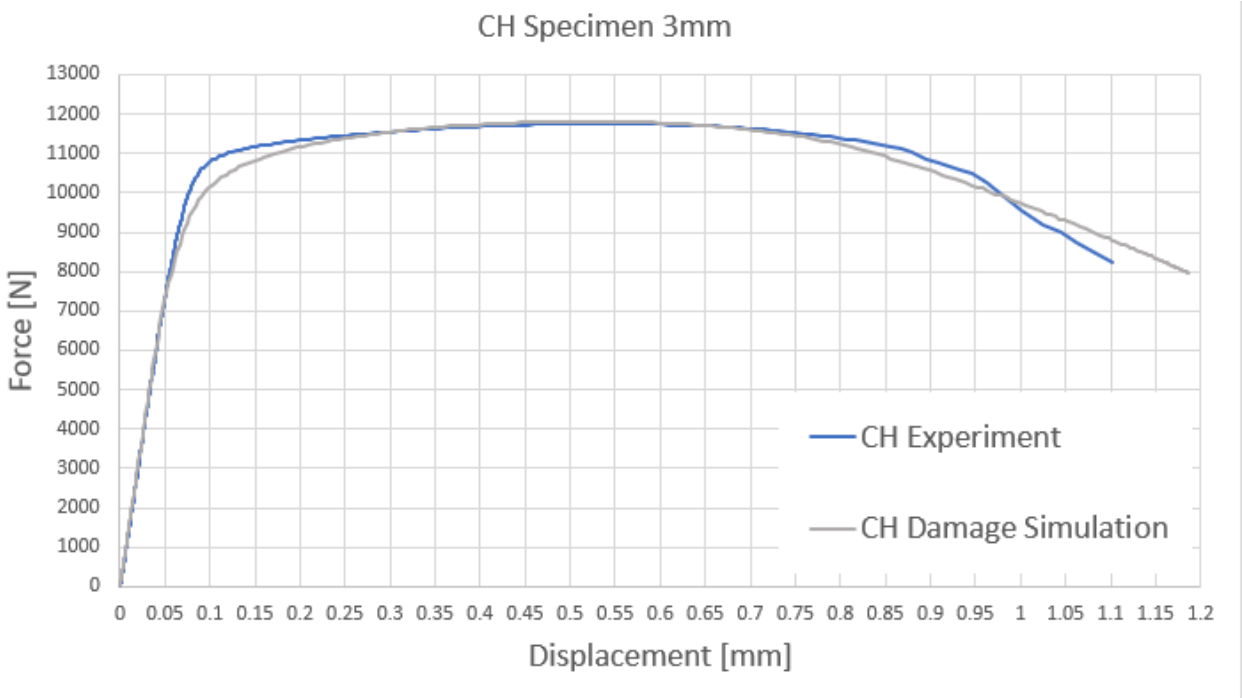

Figure 4.8: Damaged force-displacement response of 3 mm CH specimen

The above displayed results show perfect matching of measured and predicted material response. Damage initiation is well described because of an accurate hardening prediction. Additionally, this specimen is used for damage evolution displacement definition. Hence, the simulated ductile damage propagation is quite consistent with the measured one.

Following figures (4.9 and 4.10) present the damaged force-displacement response of NT20 specimen.

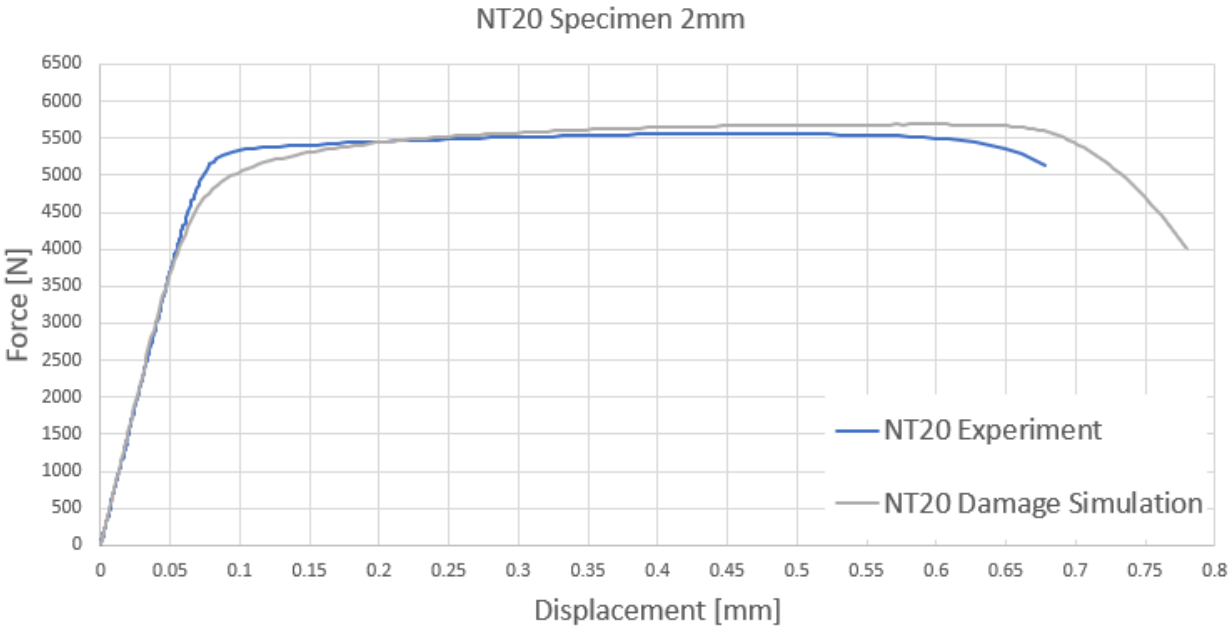

Figure 4.9: Damaged force-displacement response of 2 mm NT20 specimen

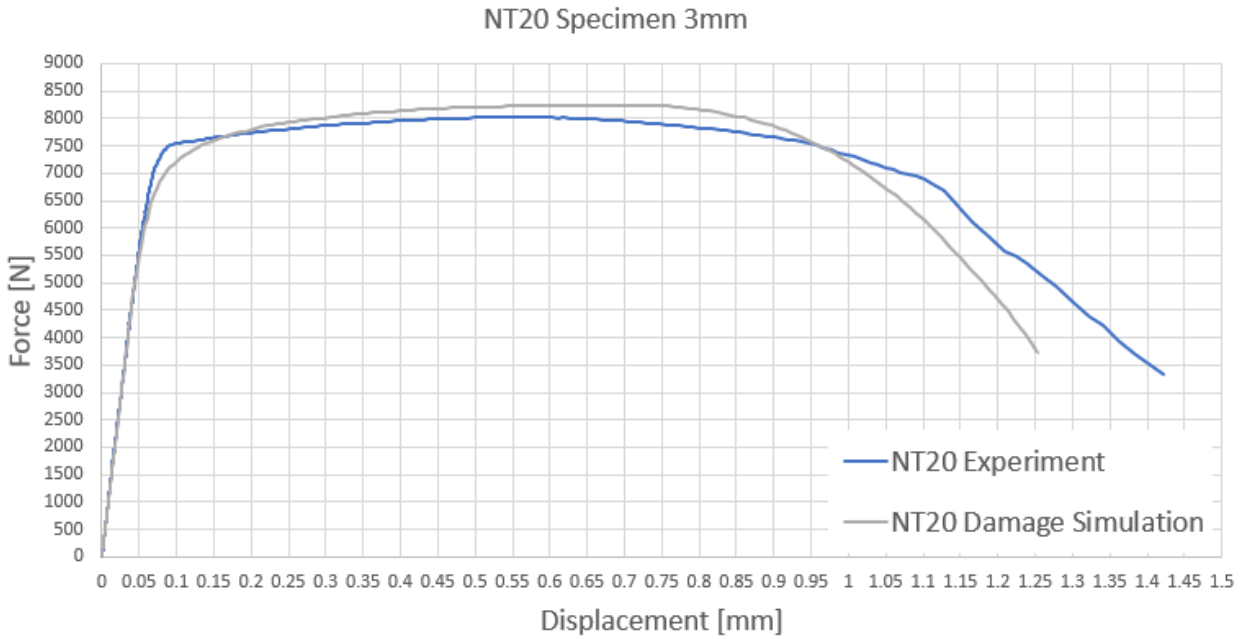

Figure 4.10: Damaged force-displacement response of 3 mm NT20 specimen

As shown in Figure 4.9, the simulated damage initiation displacement of 2 mm NT20 specimen is slightly over predicted. Hence, the damage propagation is overestimated for about 0.1 mm. However, damage initiation displacement is correctly predicted for 3 mm specimen (Figure 4.10). Due to the higher triaxialities (Figure 4.3), hardening model slightly overestimates the force level and therefore the damage initiation and evolution are a little bit mismatched.

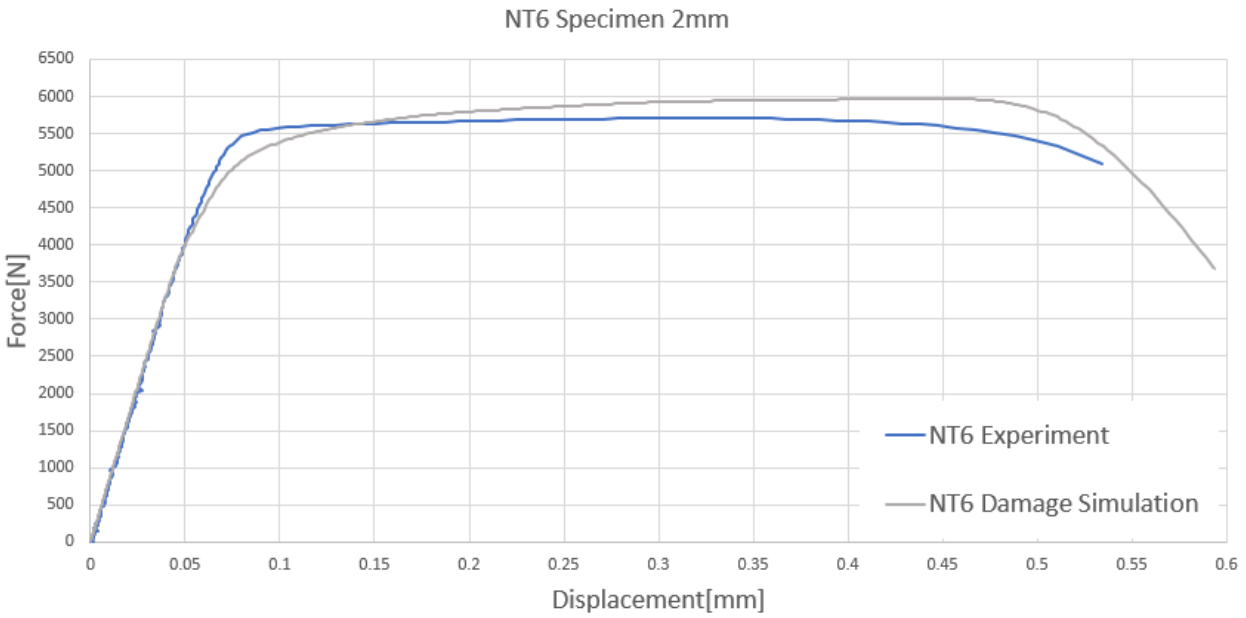

Figure 4.11: Damaged force-displacement response of 2 mm NT6 specimen

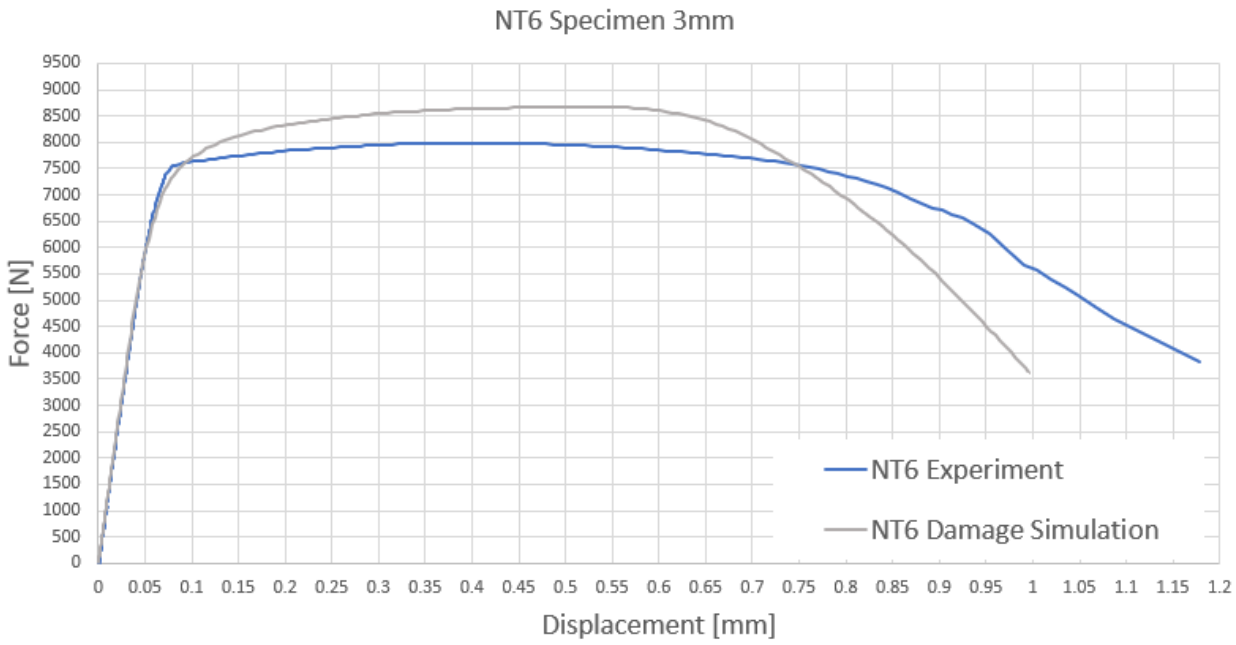

Figure 4.12: Damaged force-displacement response of 3 mm NT6 specimen

The damage initiation displacement of 2 mm NT6 specimen (Figure 4.11) is over predicted, as well as the damage evolution. Furthermore, damage initiation and evolution prediction of 3 mm NT6 specimen (Figure 4.12) exhibits even greater deviation from the experimental results. Since the hardening behavior of the NT6 specimen is not satisfactorily described, the damage initiation and evolution can not be completely accurate defined.

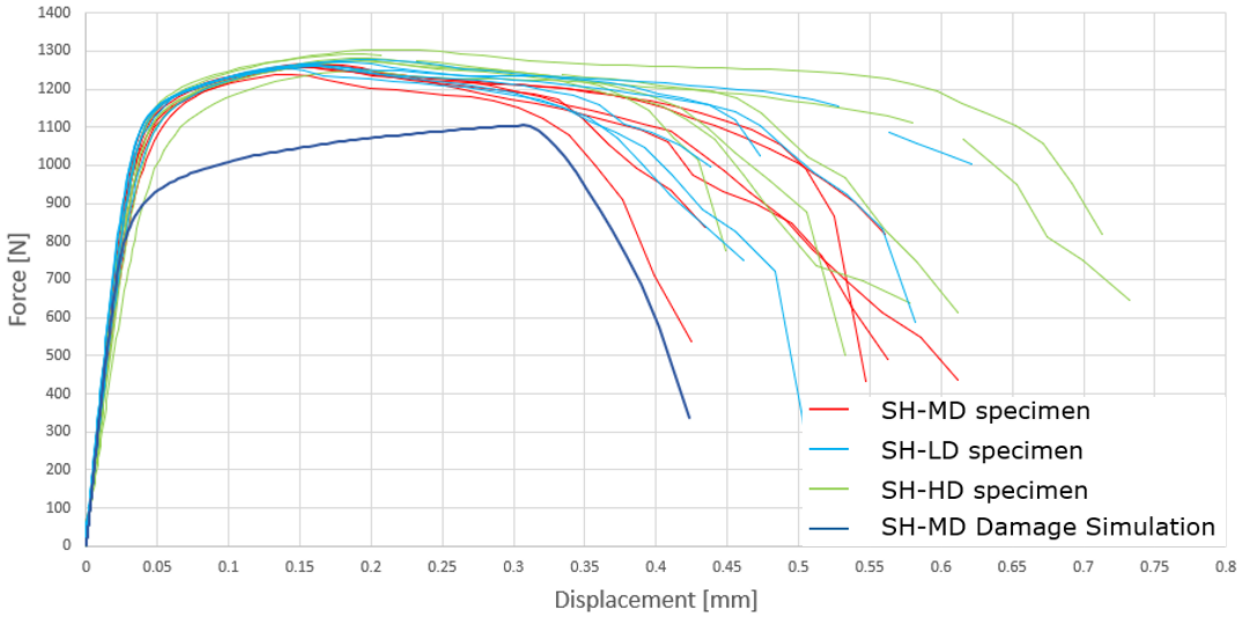

Figure 4.13: Damaged force-displacement response of 2 mm SH-MD specimen

Since it is not possible to accurately describe the hardening behavior with proposed hardening model, damage initiation results of the 2 mm shear specimen do not match the

measured values, as shown in Figure 4.13. Moreover, the assumption of linear relationship in ductile fracture limit curve (Figure 4.3) leads to conservative result.

5 Conclusions

In this paper, numerical modelling of aluminum wrought alloy 6005-T6 behavior from the beginning of loading to fracture is presented. The accuracy of numerical models is validated to experimental results. Experimental measurements are conducted on numerous samples of 7 specimen types. Moreover, two specimen thicknesses, 2 and 3 mm, are evaluated.

Firstly, a general description of 6005-T6 aluminum wrought alloy is presented. Furthermore, theoretical description of the used Swift-Voce flow law is given, as well as the hardening parameters definition procedure. Secondly, the theoretical background of ductile damage is described. In addition, the ductile damage model implemented in *Abaqus* is studied. Digital image correlation method, which is integrated in *Aramis* software, is used to obtain the displacement and strain fields during the loading. The selected specimen types geometries are designed in order to cover the triaxiality area form shear to bi-axial stress state. Due to inaccurate cutting of 3 mm shear specimens, these specimens are not used for validation in this paper. Moreover, 3 shear specimen types exhibit similar force-displacement response and therefore only one type is used for numerical comparison. Numerical simulations are conducted in *Abaqus/Explicit* software, which is a powerful tool for dynamic and quasi-static damage modelling. In order to ensure the numerical quasi-static response, mesh density and loading rate evaluation is performed.

Swift-Voce parameters are obtained from a least-square fit of stress-strain points using the *Matlab* software. Since two thicknesses are used, two separate stress-strain fits are conducted. The final Swift-Voce parameters set is obtained through inverse analyses using the simulations in *Abaqus/Explicit*. From the force-displacement response as well as from the strain fields comparison it can be concluded that the proposed model very accurately describes the 6005-T6 hardening. The greatest accuracy is achieved for uniaxial stress state. However, the NT6 and SH-MD predictions exhibit non negligible deviation from experimental results. Due to the anisotropy of extruded material, these specimens have

weaker mechanical properties in non-extrusion direction. Moreover, due to specific geometry, the stress values are high in non-extrusion direction for these specimen types. Since the proposed Swift-Voce model uses von Mises yield surface in combination with isotropic hardening, it can not adequately describe hardening for lower and higher triaxialities.

Ductile damage parameters calibration is conducted thorough combined experimental-numerical procedure. Experimental plastic strain at onset of damage is correlated with numerical triaxiality in order to define the ductile fracture limit curves for both thicknesses. These curves are described by the linear relation between fracture strain and triaxiality. Furthermore, the CH specimen is successfully used for the definition of damage evolution parameter. Due to the accurate hardening calibration, the proposed model correctly describes ductile damage of UT, CH and NT20 specimens. However, due to slightly deviation of predicted NT6 and SH-MD hardening behavior, the ductile damage is also slightly mismatched. Moreover, the assumption of the linear relationship between fracture strain and triaxiality leads to conservative damage prediction of shear specimens.

According to findings of this thesis, it is possible to improve hardening and damage prediction of this material. Therefore, the following recommendations for any potential continuation of this research are presented:

- Since extruded sheet metals exhibit significant anisotropy, which can not be totally eliminated through tempering process, the experimental measurements in non-extrusion directions should be performed. Measurements in 45° and 90° should adequately describe the anisotropy.

- The proposed Swift-Voce flow law for further studies should be based on Hill's or Barlat Yld 2000-3D yield functions, as these can successfully describe material anisotropy.

- The future studies could find one ductile fracture limit curve for both thicknesses, as the difference between obtained 2 and 3 mm curves is not significant.

- Due to conservative results of shear specimens, fracture strain for shear stress state should be increased. New measurements with larger number of states would lead to more precise fracture strain determination. Moreover, the exponential relationship between shear and tensile triaxiality could be used.

Bibliography

[1] E-Mobility Outlook 2014, *The view from North America*, Center for Automotive Research at Stanford-CARS

[2] Gaffney, B., *Vehicle Battery Pack Design and Consideration of Repurposing*, Toronto, 2015.

[3] Pan, L., Zhang, C., *A High Power Density Integrated Charger for Electrical Vehicles with Active Ripple Compensation*, University of Bristol, 2015.

[4] http://www.bancoaluminium.com/

[5] Davis, J. R., *Alloying: Understanding the Basics*, ASM International, 2001.

[6] Wessel, J. K., *The Handbook of Advanced Materials: Enabling New Designs*, Wiley-Interscience, 2004.

[7] Larour, P., *Strain rate sensitivity of automotive sheet steels: influence of plastic strain, strain rate, temperature, microstructure, bake hardening and pre-strain*, Fakultat fur Georessourcen und Materialtechnik der Rheinisch-Westfalischen Technischen Hochschule, Aachen, 2010.

[8] Papasidero, J., Doquet, V., Mohr, D., *Ductile fracture of aluminum 2024-T351 under proportional and non-proportional multi-axial loading: Bao-Wierzbicki results revisited*, International Journal of Solids and Structures, 2015.

[9] Reddy, A. C. S., Bhaskar Reddy, C., Paleswar, D. V., *Review on Different Hardening Models for Computation of Deep Drawing Process Simulation*, Indian Academy of Sciences, 2020.

[10] https://en.wikipedia.org/wiki/File:Yield_surfaces.svg

[11] Kelly, P., *Solid Mechanics Part II*, The University of Auckland, 2013.

[12] Mohr, D., Marcadet, S. J., *Micromechanically-motivated phenomenological Hosford-Coulomb model for predicting ductile fracture initiation at low stress triaxialities* International Journal of Solids and Structures, 2015

[13] Roth, C. C.,Mohr, D., *Determining the Strain to Fracture for Simple Shear for a Wide Range of Sheet Metals*, International Journal of Mechanical Sciences 2018.

[14] Ross C., Case J., Chilver A., *Strength of Materials and Structures 4th Edition*, Butterworth-Heinemann, Oxford, 1999.

[15] Pardoen, T., Hutchinson, J. W., *An extended model for void growth and coalescence*, Journal of the Mechanics and Physics of Solids, 2000.

[16] Tvergaard, J., *Influence of voids on shear bands instabilities under plane strain conditions*, International Journal of Fracture, 1981.

[17] http://mms2.ensmp.fr/msi_paris/transparents/Matthieu_Maziere/2013-MM-Damage.pdf

[18] Sancho, A., Cox, M. J., Cartwright, T., Aldrich-Smith, G. D., Hooper, P. A., Davies, C. M., Dear, J. P., *Experimental techniques for ductile damage characterisation*, Imperial College London, London, 2016.

[19] Rice, J.R., Tracey, D.M., *On the Ductile Enlargement of Void sin Triaxial Stress Fields*, Journal of the Mechanics and Physics of Solids, 1969.

[20] Gurson, A.L., *Continuum Theory of Ductile Rupture by Void Nucleation and Growth: PartI-Yield Criteria and Flow Rules for Porous Ductile Media*, Journal of Engineering Materials and Technology, 1977.

[21] Tvergaard, V., Needleman, A., *Analysis of the cup-cone fracture in a round tensile bar*, Acta Materialia-Journal, 1984.

[22] Kachanov, L. M., *Introduction to Continuum Damage Mechanics*, Springer Science and Business Media, Springer Netherlands, 1986.

[23] Lemaitre, J., Desmorat, R., *Engineering Damage Mechanics*, Springer, 2005.

[24] Bonora, N., *A Nonlinear CDM Model for Ductile Failure*, Engineering Fracture Mechanics 58, 1997.

[25] Johnson, G. R., Cook, W. H., *Fracture Characteristics of Three Metals Subjected to Various Strains, Strain-Rates, Temperatures and Pressures*, Engineering Fracture Mechanics-Journal, 1985.

[26] Xue, L., Wierzbicki, T., *Ductile Fracture Initiation and Propagation Modelling Using Damage Plasticity Theory*, Engineering Fracture Mechanics, Massachusetts Institute of Technology, Massachusetts, 2008.

[27] Abaqus Analysis User's Guide, Dassault Systemes, 2016.

[28] Bai, Y., Teng, X., Wierzbicki, T., *On the Application of Stress Triaxiality Formula for Plane Strain Fracture Testing*, Journal of Engineering Materials and Technology, 2009.

[29] Park, S., Lee, K., Cerik, B., Choung, J., *Comparative Study on Various Ductile Fracture Models for Marine Structural Steel EH36*, Journal of Ocean Engineering and Technology, 2019.

[30] Mohr, D., Roth, C. C., *Ductile fracture experiments with locally proportional loading histories*, International Journal of Plasticity, 2015.

[31] Vrgoč, A., *Numerical analysis of spot welds in sheet metal structures exposed to mechanical shock and vibration loading*, University of Zagreb, 2019.

[32] Colby, R. B., *Equivalent Plastic Strain for the Hill's Yield Criterion under General Three-Dimensional Loading*, Massachusetts Institute of Technology, 2013.

[33] Barlat, F. *et al*, *Plane stress yield function for aluminum alloy sheets-part 1: theory*, International Journal of Plasticity, 2002.

[34] Hooputra, H., Gese, H., Dell, H., Werner, H., *A comprehensive failure model for crashworthiness simulation of aluminium extrusions*, International Journal of Crashworthiness, 2012.